Summer 8-10-2018

Mechanistic Studies of Reducible Metal Oxides as Hydrodeoxygenation Catalysts

Akbar Mahdavi Shakib
University of Maine, akbar.mahdavi@maine.edu

MECHANISITIC STUDIES OF REDUCIBLE METAL OXIDES AS HYDRODEOXYGENATION CATALYSTS

By

Akbar Mahdavi Shakib

B.S. Teacher Training University of Tehran, 2007

M.S. Sharif University of Technology, 2010

A DISSERTATION

Submitted in Partial Fulfillment of the

Requirements for the Degree of

Doctor of Philosophy

(in Chemistry)

The Graduate School

The University of Maine

August 2018

Advisory Committee:

Dr. Brian G. Frederick, Associate Professor of Chemistry, Co-advisor

Dr. Thomas J. Schwartz, Assistant Professor of Chemical Engineering, Co-advisor

Dr. Rachel N. Austin, Professor of Chemistry, Barnard College

Dr. Carl. P. Tripp, Professor of Chemistry

Dr. Barbara J. W. Cole, Professor of Chemistry

Dr. François G. Amar, Professor of Chemistry and Dean of the Honors College

MECHANISITIC STUDIES OF REDUCIBLE METAL OXIDES AS HYDRODEOXYGENATION CATALYSTS

By Akbar Mahdavi-Shakib

Dissertation Advisors: Dr. Brian G. Frederick, Dr. Thomas J. Schwartz

An Abstract of the Dissertation Presented
in Partial Fulfillment of the Requirements for the
Degree of Doctor of Philosophy
(in Chemistry)
August 2018

Hydrodeoxygenation of phenol to benzene using ruthenium supported titania catalysts strongly varies depending on the support crystal structure and preparation conditions. Here, we performed spectroscopic characterization of titania supports to identify the surface impurities common to commercial and synthesized titania samples using a variety of spectroscopic methods. Sulfate impurities were detected for the commercial anatase samples and a procedure for their elimination was proposed so that inactive catalysts gained reactivity. Surface hydroxyls of different TiO_2 samples (anatase, rutile, and pyrogenic) were identified using diffuse reflectance infrared Fourier transform spectroscopy (DRIFTS) experiments performed on vigorously cleaned surfaces and a facet-specific assignment was proposed using DFT calculations performed by our collaborators. In addition, the electronic structure of TiO_2 samples were studied using the reaction of vigorously cleaned TiO_2 samples with H_2/D_2. Our results revealed that sulfate impurities of the commercial anatase samples change their electronic structure consistent with creation of deep electronic trap states within the band gap. Our results are used to derive structure-activity relationships for the Ru/titania catalyzed hydrodeoxygenation reactions of phenol.

DEDICATION

To my parents, Ahad Mahdavi Shakib and Kobra Monazami.

To Barbara Frederick

ACKNOWLEDGEMENTS

I would like to thank my parents for their endless love and support during all my years of studies, and especially for the past few years we had to spend apart.

I would like to thank my supervisor Dr. Brian G. Frederick for his mentorship, for going above and beyond to support my training and graduate career, and for being a role model in his scientific thinking. I feel grateful to call Brian a friend.

I would like to thank my co-advisor Dr. Thomas Schwartz for his mentorship and support. Tom's expertise in heterogeneous catalysis and chemical engineering enriched my vision as a chemist.

I would like to thank Dr. Rachel Austin, the P.I. on this project, for her mentorship and for being a role model in scientific communication and leadership. Rachel created many opportunities for us to collaborate with great minds, and I am grateful for it.

I would like to thank people whose works are presented here, especially Lars Grabow and Juan Arce-Ramose Manual for the DFT calculations, Samra Husremovic for the catalytic data, and George Bernhardt for his assistance in measuring XPS and XRD data.

I also would like to thank Dr. Carl P. Tripp, Dr. Barbara Cole, Dr. François Amar, Amir Rahmani, Christian Geci, Sabrina Sultana, and Sudheera Yaparatne, for helpful discussions.

This research was supported by the U.S. National Science Foundation under award number NSF 1565843. I would like to thank NSF, LASST, and the Chemistry Department at the University of Maine for their financial support during my doctoral research. We also would like to acknowledge the DOE Award #DE-FG02-07ER46373.

Lastly, I would like to thank each and every one who was part of this journey. My friends, my colleagues, and the many people who, along the way, made this possible.

TABLE OF CONTENTS

LIST OF TABLES

LIST OF FIGURES

CHAPTER 1

INTRODUCTION

1.1. Motivation

Fossil fuels have been the primary source of energy and carbon-based materials since the industrial revolution. They fueled industries and made the improved life style of modern societies possible. Projections indicate that the demand for fossil fuels will continue to increase since the middle-class population is expanding in developing countries.[1] Although fossil fuel resources are not sustainable in nature, recent discovery of new sources of natural gas throughout the world suggests[1] that the peak in fossil fuel production is not happening as soon as previously suggested.[2] Therefore, fossil fuel resources are able to meet the growing demand for energy and materials for many years to come.[1] However, there are many current environmental concerns associated with the continued use of fossil fuels, such as water and air pollution during extraction,[3] methane release during extraction,[4] oil spills during extraction and transportation, and most importantly CO_2 emission when fossil fuels are burned. Currently, climate change caused by high levels of atmospheric CO_2 is one of the biggest environmental concerns[5] and it is critical to mitigate the CO_2 emission levels as soon as possible. This will not happen until we find alternative sources of energy that can respond to the growing energy demand that are economically competitive. As Chu and Majumdar commented, "The Stone Age did not end because we ran out of stones; we transitioned to better solutions".[1]

To mitigate CO_2 emission, we need to switch from carbon-based energy feedstock sources to sustainable energy systems such as solar energy, wind power and biofuels.[1] Solar energy and wind power are green sources of energy. However, we do not have consistent access to wind and sun light and need to store the electricity made from these renewable sources in batteries or in chemical bonds. The low energy density (on an energy/mass basis) of current batteries limits their applications in heavy machinery and long distance travel.[6] Liquid fuels in this regard are very attractive because they have high energy densities. As a result, biofuels appear as one of the future energy sources in most projections.[1]

Biofuels are any energy rich molecules that are obtained from biomass or other living organisms. Biomass is considered to be sustainable energy because the carbon released after burning biomass would eventually be released into the atmosphere during the plant respiration and when biomass decays.[7-8] On the other hand, when fossil fuels is burned, "dormant" carbon that has been captured by photosynthesis millions of years ago is released into the atmosphere.

Production of biofuels has been an evolutionary process. First generation biofuels were mostly based on fermentation of food crops such as corn.[7] However, there are environmental and ethical concerns associated with biofuels production from food resources.[9-10] These concerns became more serious when grain prices increased by 40% in 2008, which was attributed to the increased production of biofuels from food crops.[9] Newer generations of biofuels are based on non-edible carbon masses such as lignocellulose and algae.[8] Lignocellulose in this regard is very interesting because it is usually available as the waste product of agricultural and forestry activities. For example, the Margaret Chase Smith Policy Center of the University of Maine estimated in 2008 that the forest industries in Maine could produce up to 2.6 million dry tons of forest residues per year as a side product of forestry activities.[11] This amount of lignocellulosic biomass can replace 32% of Maine's current gasoline consumption by fermentation to ethanol, or 76% percent of Maine's petro-diesel consumption using Fischer-Tropsch synthesis.[11]

There are two general chemical approaches to convert lignocellulosic biomass to biofuels. In the first approach, the whole lignocellulosic biomass is converted into biofuels using gasification or pyrolysis methods.[12-14] Gasification of biomass produces CO and H_2, known as syngas, and can be converted to hydrocarbons via the Fisher-Tropsch process.[15] This method is costly because of the high pressure required for the Fisher-Tropsch process.[16-17] The pyrolysis method involves heating the biomass in the absence of oxygen to liquefy it.[18] This method produces a complex mixture containing hundreds of molecules, which is corrosive, undergoes fast aging,[19] and requires upgrading before being used as a fuel.[13-14, 20] In addition, the pyrolysis method has low selectivity toward any individual molecules and can only be used for fuel production.

In the second approach, lignocellulosic biomass is broken down into its individual components (cellulose, hemicellulose, and lignin) and each component can be converted to fuels and/or value-added products. The second approach can potentially diversify the products of biorefineries and makes them financially more viable.[21] Paper companies have mastered the separation of lignocellulosic biomass into its individual components using the Kraft-Pulping process.[22] Cellulose and hemicellulose are polymers made of sugar monomers while lignin is a polymer made of phenolic monomers.[23] Cellulose has a crystalline structure while hemicellulose and lignin are amorphous.[24] Hemicellulose can be easily separated from lignocellulosic biomass by heating the biomass with water.[25] Further treatment of lignocellulosic biomass with an aqueous solution of acid/ base,[24] or organic solvents[25] yields a white solid called wood pulp and a solution known as black liquor. Wood pulp is cellulose and black liquor contains lignin.[25]

While there are many applications for the wood pulp, black liquor is largely underused.[23] Wood pulp is used for production of paper and other valuable products such as cellulose nanofibers.[22] Cellulose can also be depolymerized into glucose and glucose can be fermented to make ethanol, or it can be converted to important platform chemicals using biological or chemical catalysts.[26] On the other hand, lignin in the black liquor is currently only used to generate energy by burning.[23] Lignin makes up approximately 30% of lignocellulosic biomass[23] and can be used as a sustainable source of liquid fuels and/or as a replacement for the petroleum-derived aromatics.

Lignin depolymerization is achieved by chemical,[27] mechanochemical,[28] electrochemical,[29] or pyrolytic[30] processes which produce a mixture of aromatics that contain methoxy, alkyl, and phenolic OH functional groups. Formate-assisted pyrolysis of lignin removes methoxy groups from the pyrolysis liquid and produces higher alkylated phenols.[30] Lignin depolymerization products are not suitable yet to be used as a transportation fuel and removal of oxygen via hydrodeoxygenation (HDO) reactions is necessary to improve fuel properties.[31] Since phenolics are one of the major components of the lignin

depolymerization reactions, phenol is a suitable model compound to evaluate the performance of HDO catalysts for upgrading of lignin-derived molecules to liquid transportation fuels.

1.1.1 Hydrogenation versus direct deoxygenation

There are two pathways for the HDO of phenol, Figure 1.1. In the first pathway, phenol is converted to benzene without hydrogenation of the benzene ring. This pathway is called direct deoxygenation (DDO). In the second pathway, the ring is hydrogenated first to form cyclohexenol, followed by hydrogenation to cyclohexanol, then dehydration to cyclohexene and finally hydrogenation to cyclohexane. This pathway is called hydrogenation dehydration (HYD). The DDO pathway may have technoeconomic advantages because it reduces the consumption and cost of hydrogen.

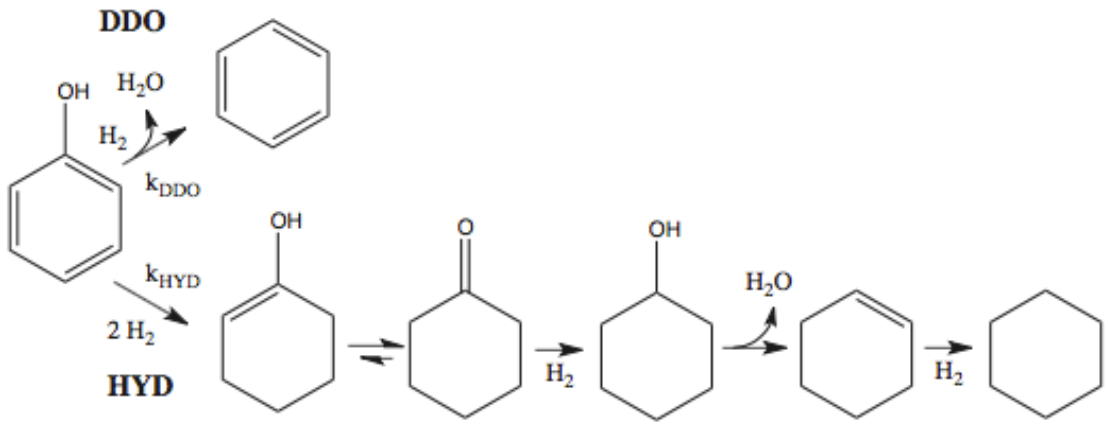

Figure 1.1. HYD versus DDO pathways. Reproduced with permission from Newman, et al.[32]

1.1.2. Unique selectivity and activity of Ru/TiO_2

Newman *et al.* showed that Ru/TiO_2 (P25) shows excellent selectivity and activity for DDO of phenol to benzene compared to catalysts prepared on other supports, as shown by the data in Table 1.1[32] However, the excellent selectivity and activity of the catalyst depends on the treatment procedure

performed following Ru deposition. When Ru/TiO_2 catalysts are calcined after Ru deposition (Ru/TiO_2-Cal (P25) in Table 1.1), catalysts have low DDO selectivity. When catalysts are reduced after Ru deposition, they are more selective toward the DDO reaction. Reductive treatment of the catalyst makes small Ru particles while oxidative treatment of the catalyst makes large Ru particles.[32] As a result, hydrogenation of the ring is the preferred pathway when Ru particles are large (~10 nm) while DDO of phenol is the preferred pathway when Ru particles are small (~1 nm), as illustrated in Figure 1.2. These observations suggest that the DDO reaction happens at the metal support interface. Newman *et al.* speculated that the possible reasons for the excellent performance of TiO_2 P25 as the catalyst support could be associated with the reducible nature of TiO_2 or strong metal-support interactions.[32]

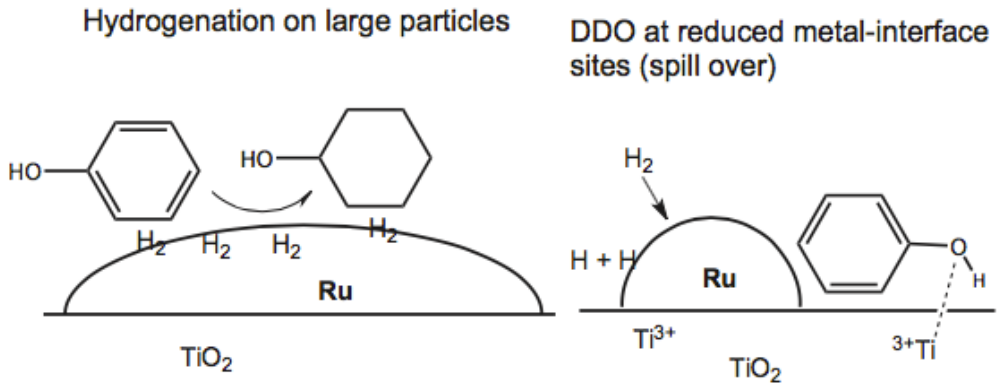

Figure 1.2. Reaction pathway on the large Ru nanoparticles vs small Ru nanoparticles. Reproduced with permission from Newman, et al.[32]

Table 1.1. DDO selectivity and turn over number (TON) of the reaction of phenol at 300 °C and 650 psi H_2 for 1 h. Data from Newman, et al.[32] All of the catalysts were reduced under H_2 at 300°C after Ru deposition, unless otherwise stated.

Catalyst	DDO selectivity	TON[b]
Ru/MCM41	16	430
Ru/C	45	260
Rn/Al_2O_3	22	240 (57)[c]
Ru/TiO_2 (P25)	85	1640 (298)
Ru/TiO_2-Cal (P25)[a]	20	160 (22)

[a]Catalyst was calcined after Ru deposition, [b]moles of products per mole of ruthenium, [c]values in the parenthesis are standard errors.

1.1.3. Mechanism of DDO of Phenol

Nelson *et. al*. investigated the mechanism of DDO of phenol over Ru/TiO_2 experimentally and theoretically to elucidate the role of support, which led to a mechanism shown schematically in Figure 1.3.[33] In this mechanism, heterolytic dissociation of H_2 between the metal nanoparticle and a surface hydroxyl with basic character forms a hydride on the metal surface and a $–OH_2^+$ group on the support surface. After heterolytic dissociation of H_2, in a concerted fashion, the hydride acts as a nucleophile to attack the C1 carbon of phenol (the carbon atom attached to the OH group) and the surface $–OH_2^+$ group acts as a Brønsted acid to protonate the –OH group of the phenol to form water. In this mechanism, the reducibility of the support does not play a role. An ideal support would be a material with amphoteric hydroxyls.

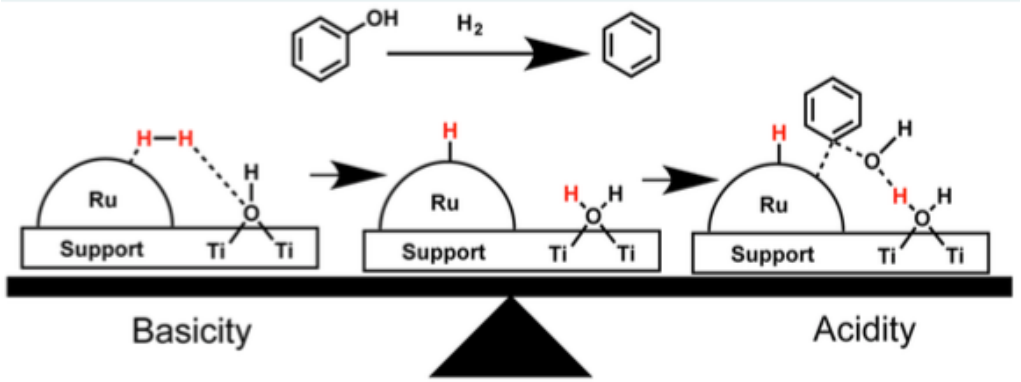

Figure 1.3. Proposed mechanism for the DDO of phenol on the metal-support interface. Adapted with permission from Nelson, et al. [33]

1.2. Role of TiO_2 crystal structure

Husremovic *et al.*[34] studied the influence of TiO_2 crystal structure on the performance of the Ru/TiO_2 catalyst for DDO of phenol. Experimental studies of Neman *et al.*, .[32] and Nelson *et al.* [33] were performed on TiO_2 P25, which is ~85% anatase and ~15% rutile. However, the theoretical investigation of the mechanism was performed on the rutile (110) TiO_2 surface. Husremovic *et al.*[34] studied catalysts made from P25, P90 (a higher surface area analog of P25 containing 95% anatase and 5% rutile phases), pure rutile-phase, and pure anatase-phase TiO_2 from several different sources to determine whether crystal structure plays a role in the DDO mechanism.

1.2.1. Materials

Titanium dioxide P-25 (Evonik, 50 m^2 g^{-1} surface area), Titanium dioxide P-90 (Evonik, 100 m^2 g^{-1} surface area, pore size 20-60 nm), TiO_2 rutile (US Research Nanomaterials, 30 nm particle size, 35-60 m^2 g^{-1} surface area, pore size 20-60 nm), and four TiO_2 anatase samples from Sigma Aldrich, denoted "SA", US Research Nanomaterials, denoted "USR", Alfa Aesar, denoted "AA", and Nanografi, denoted NG, were all purchased from their respective manufacturers. Anatase BC was synthesized at Barnard College following a published procedure.[35] Briefly, to 50 ml 100% ethanol in a 100 ml three-

neck round-bottom flask in ice, we added 2.89 ml of $TiCl_4$ dropwise with a pressure equalized addition funnel. Once addition of $TiCl_4$ was completed, the reaction was stirred at ambient condition for 2 hours. The reaction mixture was placed in an oven at 87 °C and heated for three days. The powder was rinsed by addition of milli-Q water and centrifuged at 20,000 rpm for 30 minutes, several times every day for 30 days until the pH of the supernatant was around 7. The resulting material, denoted "BC", has a surface area of 159 m^2/g and a bimodal distribution of pores with maxima around 4 and 12 nm. $RuCl_3 \cdot 3H_2O$, liquefied phenol, and diethyl ether were purchased from Sigma-Aldrich. 200 mesh Cu TEM grids were purchased from Ted Pella Inc. (Redding, CA).

1.2.2. X-ray diffraction characterization of the support

The x-ray diffraction studies were also carried out at the Shared Materials Characterization Laboratory (SMCL) of the CNI at Columbia University using the PANalytical Xpert3 theta-theta Powder X-ray diffraction (XRD) instrument equipped with Cu Kα radiation. The operating voltage was 45 kV and the current 40 mA. The experiments were conducted in the Bragg-Brentano geometry using a zero-background holder in order to minimize the background signal and eliminate the diffraction peaks from the holder. The two-theta angular range for the scans was 20-100°. The scan step size was 0.1° and the dwell time 100 s per step. For the incident beam, a 15 mm mask and 0.5° divergence and 1° antiscatter slits were employed. For the diffracted beam, the 0.5° antiscatter slit was used. The powder samples were mixed with isopropyl alcohol to allow for ease of placement in the sample holder.

Figure 1.4 shows the x-ray diffraction patterns of anatase, rutile, P25, P90, and a physical mixture of anatase and rutile (90:10). The X-ray diffractograms of the SA, USR, and AA anatase show pure anatase phase, with selected planes indexed. The X-ray diffraction experiments show the presence of both anatase and rutile in P25 and P90. P90 shows 95% anatase and 5% rutile content, and P25 shows 87% anatase

and 13% rutile. Nanographi anatase (data not shown) shows all of the anatase lines and an additional line at $2\theta = 50.4°$ which was not identified.

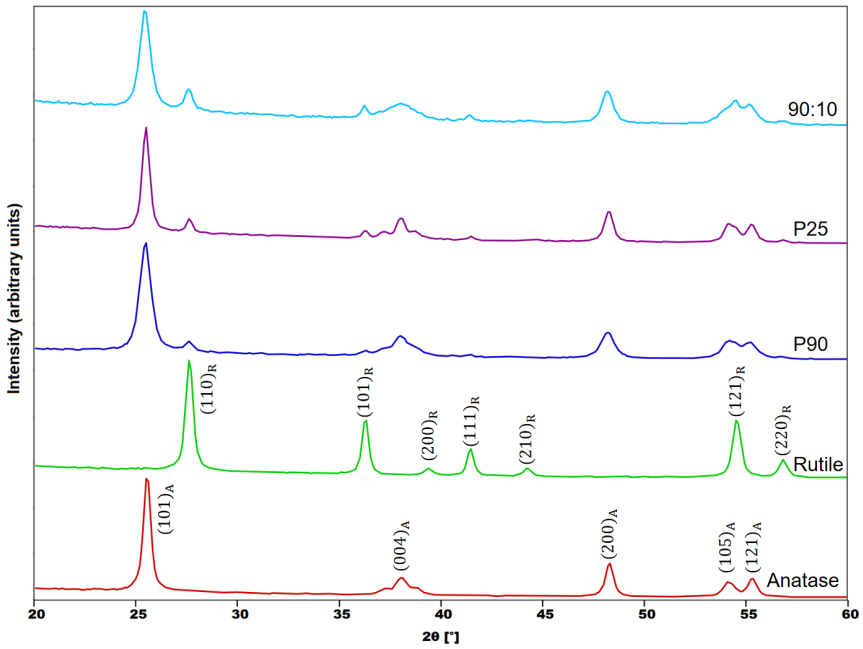

Figure 1.4. XRD patterns for anatase, rutile, pyrogenic (P90 and P25) and a physical mixture of anatase and rutile (90:10) titania, showing that the pyrogenic titania patterns contain peaks assignable to both anatase and rutile. The patterns have been displaced for clarity.

1.2.3. Catalyst preparation

Catalysts were prepared on a 5 gram scale with a metal loading of 1% (~50 mg of Ru per 5 g of TiO_2). The metal precursor ($RuCl_3$) was dissolved in Milli Q water and added to the support until a paste-like consistency was obtained. The mixture was dried overnight at 90 °C and crushed to uniform consistency.

Catalysts were reduced immediately prior to each reaction with H_2 in a 25 mL 4590 Parr stirred micro reactor sealed with a flat graphite gasket. After sealing the catalyst in the reactor, the system was purged three times with Ar gas and gradually heated to 573 K under flowing H_2 gas. When the system reached 573 K, the reactor was kept under flowing H_2 for another 0.5 h. Then, an additional 550 psig of

H_2 was added and the system was maintained at that pressure and temperature for 1 h. Post-reaction the reactor was cooled to room temperature prior to venting the system.

The wt. percent metal loading of catalysts was determined using a Thermo Scientific iCAP 600 ICP-OES spectrometer with microwave-assisted digestion. Approximately 25 to 30 mg of catalyst was weighed and placed in a CEM EasyPrep microwave digestion vessel with 8 ml of a 3 to 1 mixture of HCl and HNO_3 (trace metal grade). The vessels were sealed and placed in a CEM MARS 6 microwave. The temperature was raised to 220 °C over two hours and then held for 30 min. The samples were then cooled to room temperature before being diluted to a total volume of 50 ml in MilliQ water. The digested samples were run through the ICP and the ruthenium concentration was determined by comparing the emission to a calibration curve made using ruthenium standards with concentrations of 0 ppm, 4 ppm, and 12 ppm. The results were confirmed by analysis of selected samples by Galbraith Laboratories.

1.2.4. Transmission Electron Microscopy (TEM)

Conventional and high-resolution TEM was performed at Columbia University Nanoinitiative (CNI) electron microscopy facilities using the FEI Talos F200X Transmission/Scanning Transmission microscope or at the MIT Center for Materials Science and Engineering (CMSE) using the JEOL 2010 Advanced High Performance TEM. The analyzed catalysts were mixed with a minimal amount of 2-propanal and the mixture was suspended on a lacey carbon Cu grid or a silicon nitride window. The operating voltage of the FEI Talos was 200 kV. The HRTEM imaging was done using the 60 μm objective aperture in order to include the first diffracting planes of both rutile and anatase ($(110)_R$ and $(110)_A$) and to achieve higher imaging contrast. Identification of specific particles in the HRTEM image was done by filtering the respective atomic plane periodicity of each phase in fast Fourier transforms (FFT) of the images. Selected area electron diffraction patterns were used to determine the phases present in larger populations of particles compared with the HRTEM images. Prolonged exposure to the electron

beam resulted in amorphization of the particles and thus care was taken to minimize the imaging time. Additionally, we found that the carbon layer in the grids was not fully amorphous, and thus it became necessary to prepare samples using silicon nitride windows. However, once optimal imaging conditions were identified, all the remaining TEM work was done using the holey carbon grids with no complications of imaging and interpretation resulting from their use.

Ru/TiO_2 catalysts have been shown to form small evenly spaced nanoparticles of ruthenium upon reduction with hydrogen. In prior work, we demonstrated that these nanoparticles are an essential component of selective HDO catalysts.[32] In that work, catalysts that had been calcined prior to reduction had much larger and irregular particles and preferentially catalyzed hydrogenation reactions. In this work, HRTEM images of reduced Ru/rutile, Ru/anatase, Ru/P25 and Ru/P90 were compared. All materials show an even distribution of approximately 2 nm Ru nanoparticles (Figures 1.5 and 1.6).

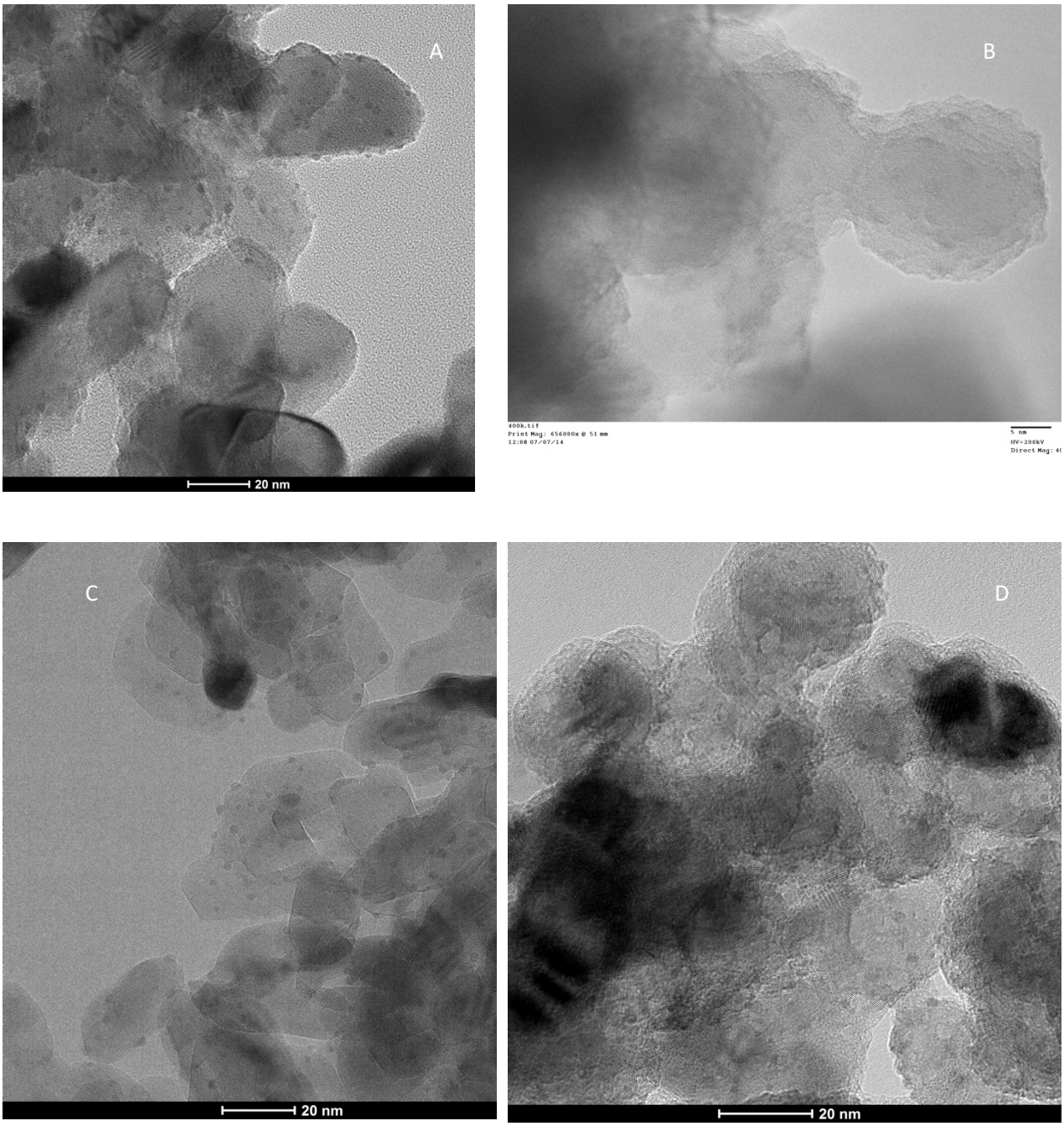

Figure 1.5. HRTEM images for (A) Pretreated Ru on rutile, (B) Pretreated Ru on P25, (C) Pretreated Ru on Nanographi anatase, and (D) Pretreated Ru on P90.

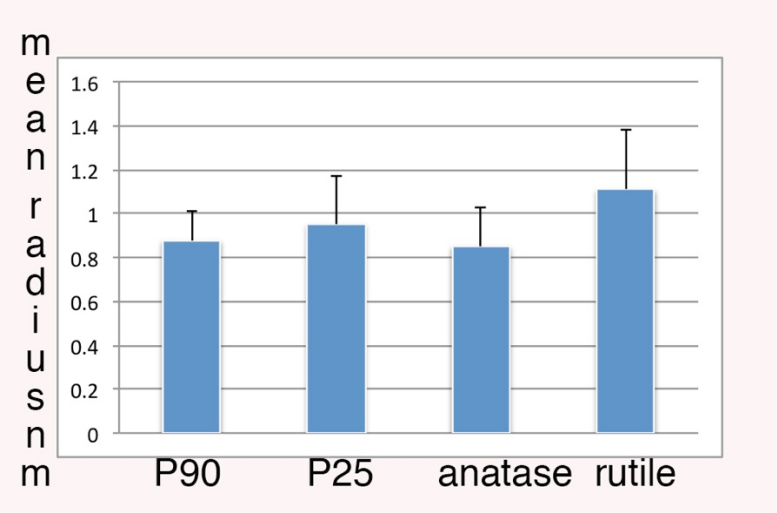

Figure 1.6. Mean radius of ruthenium particles (nm) on TiO_2 supports as obtained from an analysis of HRTEM images.

Detailed characterization of the titania support without ruthenium was undertaken to address questions raised by the catalytic data (see below) that showed that pyrogenic titania (P25 and P90) create catalysts more similar to rutile-based catalysts than anatase-based catalysts, despite the fact that P90 and P25 are predominantly anatase. HRTEM showed that P90 contains rutile particles (Figure 1.7), but in comparison to the anatase spots, the rutile spots are rare.

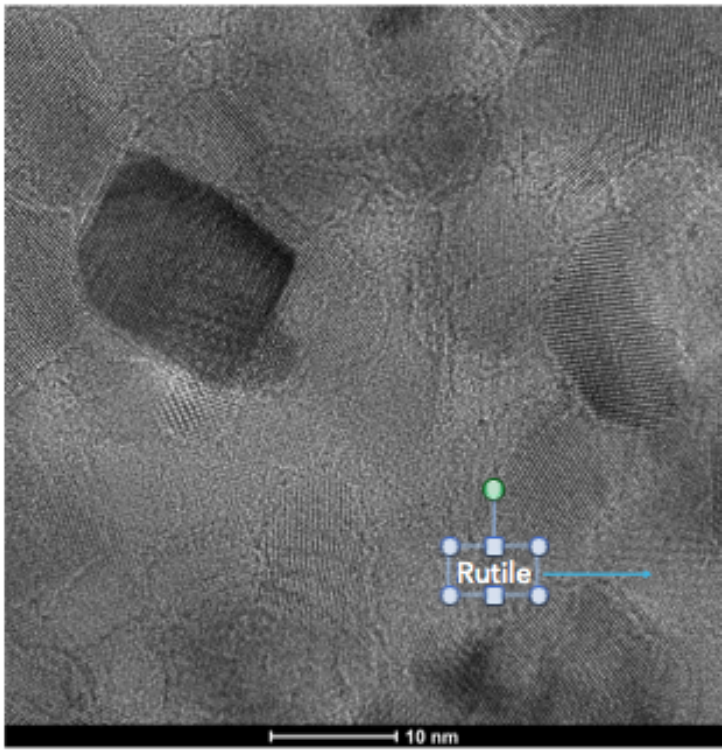

Figure 1.7. HRTEM showing a rutile particle in P90

Figures 1.8a and 1.8b are SAED patterns of P90. These patterns also confirm the presence of rutile and anatase in P90, as indicated in the XRD data. However, whereas anatase exhibits full diffraction rings (Fig. 1.8a), rutile only exhibits isolated diffraction spots (Fig. 1.8b). It should be noted that the diffraction spots of rutile are distinct from those for anatase since the two phases have different crystal structures and thus d-spacings. The presence of isolated diffraction spots, in addition to identification of individual rutile particles in HRTEM images, indicates that rutile is present as a second phase in P90 with particles that are comparable in size to those of anatase (Figure 1.7).

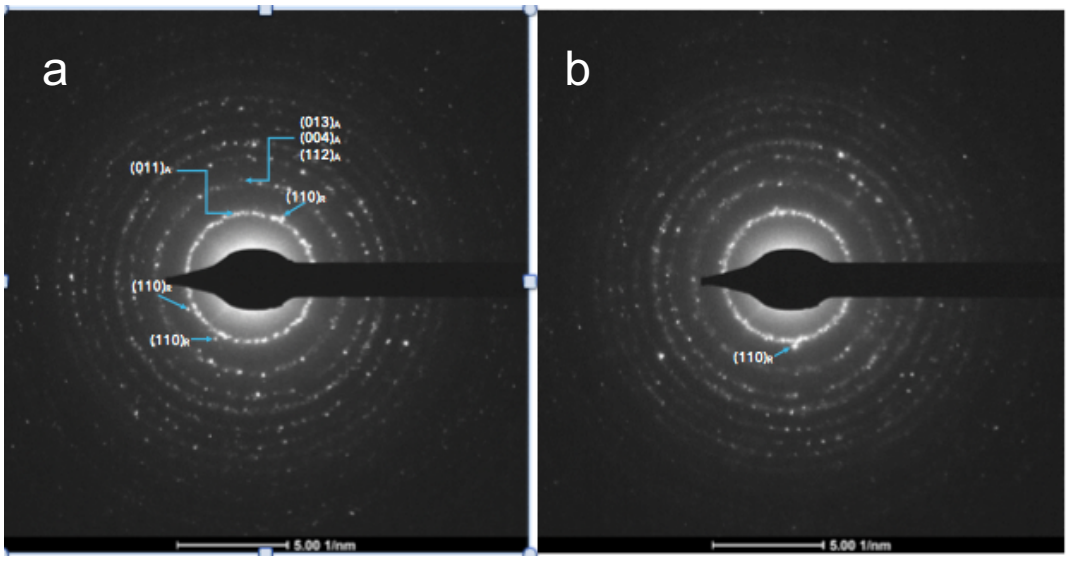

Figure 1.8. TEM diffraction data showing diffraction from (a) anatase and (b) rutile grains in P90

1.2.5. Catalytic reaction

In a standard reaction 4 ml of phenol (10 wt % water, Sigma Aldrich) was introduced into the reactor with 120 mg of catalyst reduced immediately prior to the reaction. The system was purged three times with Ar and pressurized to 5 psi under an argon atmosphere. The temperature was then gradually increased to 573K with stirring at 650 RPM. After the set temperature was reached, the system was pressurized by addition of 650 psi of H_2. The reaction time was 15 minutes and in this time span the system was repressurized if a 50 psi drop in pressure was observed. After the reaction, the system cooled in air until the temperature dropped to 200 °C. Then, the reactor was rapidly cooled using an ice bath to prevent extended reaction times. Samples were immediately analyzed using GC/MS. Two μL of the reaction mixture were diluted in 1.5 mL of diethyl ether. The samples were injected with a standard solvent delay. Samples were analyzed using an Agilent 7820GC System with a 76930 series autoinjector and 5977E network mass selective detector with a HP-5MS cross-linked 5% PH ME siloxane capillary column (dimensions of 30 m × 0.25 mm × 0.25 μm) using UHP He. The method contained a 5 min hold

at 318 K, followed by a ramp at 10 K/min to 498 K. Product yields were obtained from calibrated GC/MS spectra. Results of the catalytic reactions are summarized in Table 1.2.

Reactivity data presented in Table 1.2 showed that there was inconsistency between the DDO reaction results and crystal phase composition of the catalyst support. Catalysts prepared on rutile are as selective to benzene as those prepared on P90 and P25. However, catalysts synthesized with anatase supports were considerably less selective for DDO of phenol to benzene, while producing more cyclohexane and other hydrogenation products. The difference in DDO selectivity (i.e. benzene yield) between pyrogenic titania and pure anatase supported catalysts is surprising considering that P90 is ~95% anatase. Here we performed extensive physicochemical characterization of TiO_2 supports in order to build structure-activity relationship for DDO of phenol over Ru/TiO_2.

We explored a number of different possible explanations for the observed differences between the reactivity of the catalysts prepared from different supports. Since different impurities might exist in the TiO_2 samples, depending on the preparation methods,[36] the role of chemical impurities in the reactivity of the catalysts was explored. Similarity in the reactivity of the P90 and rutile may suggest that surface chemistry of P90 is similar to rutile. We explored the possibility of the core-shell model of pyrogenic TiO_2 (core of anatase and shell of rutile) which is argued extensively in the literature.[37-40] There is also a long interest in the pseudomorphic crystal matching between the RuO_2 and TiO_2 rutile (110) surfaces that could stabilize preferential growth of RuO_2 particles on rutile (110) surfaces, but not anatase surfaces,[41] therefore re-opening the question as to whether Ru^0 or RuO_2 is actually the active phase for the phenol DDO reaction. Because the proposed mechanism involves amphoteric hydroxyls, based on the calculations on the rutile (110) surface,[33] even though the TEM shows uniformly 2 nm nanoparticles on anatase, pyrogenic, and rutile catalysts, if the Brønsted acid/base character of hydroxyls are different for different facets, that might account for the difference in the selectivity observed. In addition, the effect of water as a co-catalyst, observed experimentally and supported theoretically,[33] raises the question of

whether the difference between hydrophilicity/hydrophobicity of the pyrogenic TiO_2 versus low temperature anatase plays a role in the selectivity.

Table 1.2. Distribution of all phenol-derived products. All results are the average of at least three separate experiments. Standard errors are given in parentheses. TiO_2 alone showed approximately 0.4% phenol conversion. "CRC" stands for materials in which the TiO_2 was calcined, reduced, and calcined at 400 °C before catalyst synthesis.

	conversion				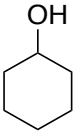	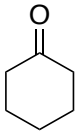	**deoxygenated**
Ru/P25	29.3 (2.1)	93.2 (0.8)	3.3 (0.6)	0.6 (0.1)	1.0 (0.2)	1.9 (0.8)	98.0 (0.5)
Ru/P90	36.7 (4.7)	91.8 (1.8)	6.1 (1.8)	0.4 (0.1)	0.7 (0.3)	0.9 (0.2)	98.4 (0.6)
Ru/rutile	17.2 (2.1)	92.2 (1.7)	3.5 (1.6)	0.6 (0.1)	1.7 (0.2)	2.0 (0.4)	96.6 (1.1)
Ru/ Anatase – US research_CRC	22 (4.7)	44.5 (6.8)	28.3 (5.5)	0.3 (0.06)	5.1 (1.6)	1.9 (0.3)	73 (1.8)
Ru/anatase – Nanografi	17.5 (3.8)	34.9 (12.9)	44.5 (11.3)	1.1 (0.2)	14.6 (2.8)	5.1 (2.1)	80.7 (4.4)
Ru/anatase (BC)	7.8 (1.2)	65.5 (2.9)	21.6 (2.2)	3.3 (1.0)	3.2 (1.0)	6.4 (1.6)	87.3 (1.7)

1.3. Organization of the thesis

In chapter 2, I will discuss DRIFTS studies in which we measured the isolated surface hydroxyls of pyrogenic TiO_2 after carefully removing surface adsorbed contaminants under rigorously dry conditions. We assigned them to specific facets of anatase and rutile using DFT calculations performed by our collaborators in Lars Grabow's group at the University of Houston, taking into account four criteria: the likelihood of a facet existing, the route to formation of the type of surface hydroxyl, the thermal stability of the hydroxyls, and the scaling of the DFT frequencies. Therefore, we propose revised frequency assignments and extend the work of Aurrovel, et al.[42] to include additional structures that can form on defective anatase surfaces.

In Chapter 3, I will discuss the XPS, XRD, ICP-OES, BET, and DRIFTS characterization of TiO_2 supports. We showed that commercial anatase samples contain sulfate impurities that deactivate the

catalyst. We reduced the sulfate content of the commercial anatase samples by vigorous pretreatment of the support prior to catalyst synthesis. Catalysts made from the pretreated commercial anatase samples showed reactivity, but they were still not as selective as P90 for the DDO reaction. In addition, catalysts made from synthesized sulfate-free anatase samples showed low selectivity for DDO as well. DRIFTS spectra showed that pure anatase samples are highly hydroxylated at the reaction temperature (300 °C) because these materials are prepared with low temperature wet condition methods. On the other hand, pyrogenic TiO_2, which is prepared with gas phase high temperature methods, is mostly dehydroxylated at the reaction temperature. This may have implications in the hydrophilicity/hydrophobicity of the surface, thought to be important in the reactions involved.

In Chapter 4, I will present DRIFTS spectra recorded during the reaction of clean surfaces with H_2 and show that broad background absorption features can be used to characterize the electronic structure of TiO_2. Our results showed that sulfate species create deep trap states within the band gap of TiO_2 and act as electron scavengers when H_2 is dissociated.

CHAPTER 2

USE OF SURFACE HYDROXYL FREQUENCIES TO IDENTIFY THE EXPOSED FACETS OF PYROGENIC TiO_2 NANOPARTICLES

The surface reactivity of TiO_2 is governed in many applications by the hydroxyl groups on its surface. FTIR spectroscopy is the most common method used to study surface hydroxyls. However, interpretation of the observed bands of powder samples is not straightforward. In this work, we propose a facet-specific assignment of the surface hydroxyls of pyrogenic TiO_2 (commonly known as P25 and P90) by comparison between experimentally observed FTIR bands under dry conditions with DFT-calculated vibrational frequencies. The vibrational frequency of surface hydroxyls on different TiO_2 surfaces are sufficiently distinct to allow them to be used for facet identification. This approach could be used for characterizing the morphologies of catalyst particles under working conditions and for *in situ* or *operando* studies of facet-specific catalytic activities.

2.1. Introduction

Titania is one of the most widely studied metal oxides,[43] with specific attention often given to the hydroxyl groups and their involvement in a variety of processes, including photocatalysis,[44-47] catalysis,[33, 42, 48] self-cleaning surfaces,[49-50] and bio-implants.[51] A powerful method for characterizing such surface species and surface reactions is vibrational spectroscopy.[52-54] However, reliable assignment of observed vibrational bands is critical for a meaningful spectral interpretation. The complexity of powder samples can make it difficult to assign the vibrational bands of surface oscillators[36] because each crystallite is composed of multiple surface facets, the relative abundance of which changes with sample preparation[48] and the local environment.[40, 42] Consequently, fundamental surface science studies often use well-characterized single crystals to elucidate information about a particular facet. However, vibrational spectroscopy studies of such surfaces are difficult to perform due to their low surface area. Most published experimental studies focus on the rutile (110) surface,[55-57] which has the lowest free energy, and

little information is available for anatase surfaces and higher-energy rutile surfaces. Density functional theory (DFT) calculations can provide information not easily accessible by experiments. In this work, we have studied the surface hydroxyls of TiO_2 powder samples under dry conditions using Diffuse Reflectance Infrared Fourier Transform Spectroscopy (DRIFTS) and DFT calculations to augment and revise previous[42] facet-specific assignments of the isolated surface hydroxyls of pyrogenic TiO_2.

TiO_2 exists in three crystal structures of rutile, anatase, and brookite.[43] Rutile is the thermodynamically stable form of TiO_2 in the bulk, while brookite and anatase are meta-stable phases.[58] However, anatase is more stable than rutile at the nanoscale.[58-59] Pyrogenic TiO_2 is synthesized by flame hydrolysis of $TiCl_4$ and contains individual anatase and rutile nanoparticles.[37-38, 40] For instance, Evonik (formerly Degussa) P25 contains 85% anatase and 15% rutile,[40] and this material is used in a variety of catalytic and photocatalytic applications.[36, 60] Because of the unique preparation method, each particle is highly crystalline[37, 40] and has few chemical impurities compared to TiO_2 samples prepared in the liquid phase,[36] which has implications for both photocatalysis and thermal catalysis.

Pyrogenic titania is unique as a support in bifunctional catalysts. For example, Ru supported on various metal oxides is selective for the conversion of phenol to benzene, with P25 showing the highest activity and selectivity.[32] In the proposed mechanism, surface hydroxyls with basic character are involved in heterolytic dissociation of H_2 at the metal-support interface.[33] Since the type of hydroxyls[42] and surface acidity/basicity[61] of different TiO_2 facets differ from each other, a more complete assignment of the surface hydroxyls on each facet of both phases is important in the mechanistic understanding of the TiO_2 catalyzed reactions.

Surface hydroxyls also have implications in photocatalysis. Photocatalytic activity of TiO_2 increases with surface hydroxyl coverage.[62-63] Surface hydroxyls are proposed to be the adsorption sites[46] and involved in the path through which electrons and holes migrate to the surface for photocatalytic reactions.[44, 47] Light induced changes in the IR hydroxyl bands were studied by several groups. Hoffmann et al.[44] reported that a band at 3715 cm^{-1} is formed after illumination with UV light, which was attributed

to the photo-induced reduction of Ti^{4+}-OH species to Ti^{3+}-OH species, although thermal effects may have been important, as the temperature increased to 160 °C under illumination.[45] Yates et al. reported that there was no change observed in the hydroxyl bands after illumination when heating was prevented.[64-65] In addition, while Hoffmann et al. reported that the 3715 cm^{-1} band was not sensitive to O_2,[45] Gates et al.[66] reported that this band was eliminated after exposure to O_2; however, their reported spectra show that water was co-introduced with O_2. In addition, surface hydroxyls create trap states in the band gap of TiO_2.[67] In work to be presented in Chapter 4, we have studied the electronic structure of TiO_2 powders using in-situ DRIFTS during reactions with H_2 to form surface hydroxyls performed in vigorously dry conditions. We[68] and others[69-70] interpret the broad electronic absorbance features in infrared spectra produced by adsorption of H_2 (D_2) on P90, anatase, and rutile as being due to formation of surface hydroxyl protons and electrons that accumulate in the trap states. Our results showed that the total defect density as well as the energy and localization of specific defects is directly dependent on the amount of bulk impurities and type of surface defects, such as surface hydroxyls. However, the experimental disagreements in the behavior and ambiguities in the assignments of the surface hydroxyl frequencies hinders the use of FTIR as a probe of surface hydroxyls in photocatalytic, as well as catalytic, reaction studies.

The first assignment of the surface hydroxyl bands of titania was made by Primet *et al.*[71] and Tsyganenko *et al.*[72] in the early 1970s. Primet *et al*. reported two bands at 3715 and 3665 cm^{-1} for anatase and two bands at 3685 and 3655 cm^{-1} for rutile. They assigned the higher frequency bands (3715 cm^{-1} band of anatase and 3685 cm^{-1} band of rutile) as terminal hydroxyls and the lower frequency bands (3665 cm^{-1} band of anatase and 3655 cm^{-1} band of rutile) as bridging hydroxyls, see Figure 2.1. Tsyganenko *et al*.[72]. reported three bands for anatase at 3725, 3670, and 3650 cm^{-1} and assigned the 3725 cm^{-1} band as terminal hydroxyls and the 3670 and 3650 cm^{-1} bands as two different kinds of bridging hydroxyls. These assignments were qualitative and based on classical mechanics; however, recent DFT studies suggest that the frequencies of terminal hydroxyls are not necessarily higher than those of bridging hydroxyls.[73-74]

Hence, fundamental surface science studies are necessary for the proper assignment of the surface hydroxyls of TiO_2.

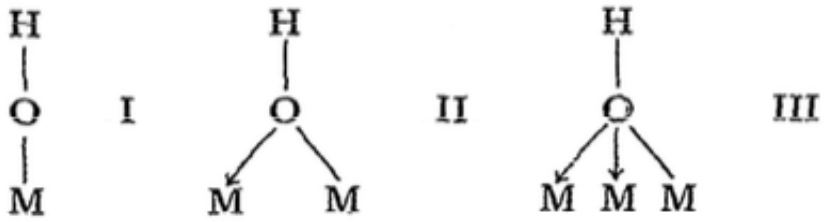

Figure 2.1. Terminal versus bridging structure of surface hydroxyls. (I) terminal, (II) and (III) bridging. Reproduced with permission from Tsyganenko et al.[72]

Arrouvel *et al.* reported the first computational assignment of the surface hydroxyls of anatase TiO_2 nanopowders.[42, 48] They studied the type, frequency, and thermal stability of the surface hydroxyls that are formed by water dissociation on the anatase surfaces and calculated the vibrational frequency of these terminal hydroxyls.[42, 75] The anatase (001) and (110) surfaces dissociate water upon adsorption regardless of surface coverage, while water dissociation on the anatase (100) surface occurs only at low coverages. Surface hydroxyls were not considered for the anatase (101) facet because this surface does not dissociate water in the defect-free state.[76] However, both theoretical[77-78] and experimental[79] work show that bridging hydroxyls could also form by dissociative adsorption of water on the surface defects (*e.g.*, oxygen vacancies) of less reactive surfaces such as anatase (101). Very recently, Nadeem et al.[79] observed bridging hydroxyls on the anatase (101) single crystal surface using scanning tunneling microscopy (STM), see Figure 2.2.

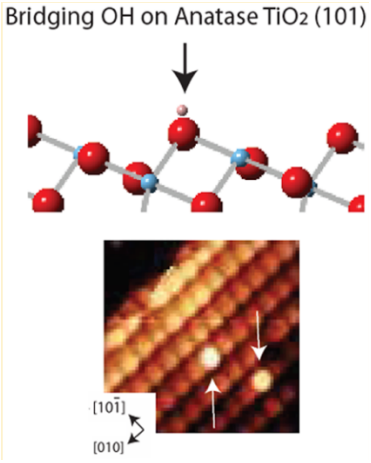

Figure 2.2. STM image showing the presence of bridging hydroxyls on the anatase (101) surface. Reproduced with permission from Nadeem et al.[79]

In this work, we have extended Arrouvel's approach to consider the hydroxyls that are formed by water dissociation on surface oxygen vacancies of less reactive surfaces such as anatase (101) and rutile (110). Using DRIFTS experiments coupled with information gleaned from the literature, we verified the spectral behavior of the surface hydroxyl bands of pyrogenic TiO_2 (P90), anatase, and rutile particles. Spectral interpretation of the surface hydroxyls in the presence of water is complicated by hydrogen bonding between the surface hydroxyls and water molecules. In addition, water molecules coordinated to Lewis acidic sites vibrate in the same frequency range as the surface hydroxyls, 3600-3800 cm^{-1}.[42] Step-wise temperature-programmed calcination with dry O_2 revealed which absorbances are due to surface impurities and the temperature at which they are eliminated. Based on these experiments, we selected 300 °C for studying the most thermally stable, isolated surface hydroxyls of TiO_2 samples. At this temperature, TiO_2 surfaces are cleaned from water and other impurities, as evidenced by the absence of the corresponding IR bands. For the DFT-based assignment of the observed bands, we calculated the vibrational frequency and energetics of hydroxyls on the anatase (001), anatase (101), and rutile (110) surfaces. Surface structure and vibrational frequency of rutile (110) surface hydroxyls are known from fundamental surface science studies, as illustrated in Figure 2.3. We present assignments of the hydroxyl

frequencies based on scaling the DFT calculated values to agree with experimental evidence from rutile (110) single crystals,[55, 57, 80-81] consistency with the observed thermal stability of the surface hydroxyls, and likelihood of the particular facet's existence. Our results suggest that the pyrogenic TiO_2 bands at ~3670 cm^{-1} are assigned to the bridging hydroxyls on the anatase (101) surface, the 3690 cm^{-1} band is assigned to the bridging hydroxyls on the rutile (110) surface, and the 3715 cm^{-1} band is assigned to the terminal hydroxyls on the anatase (001) surface.

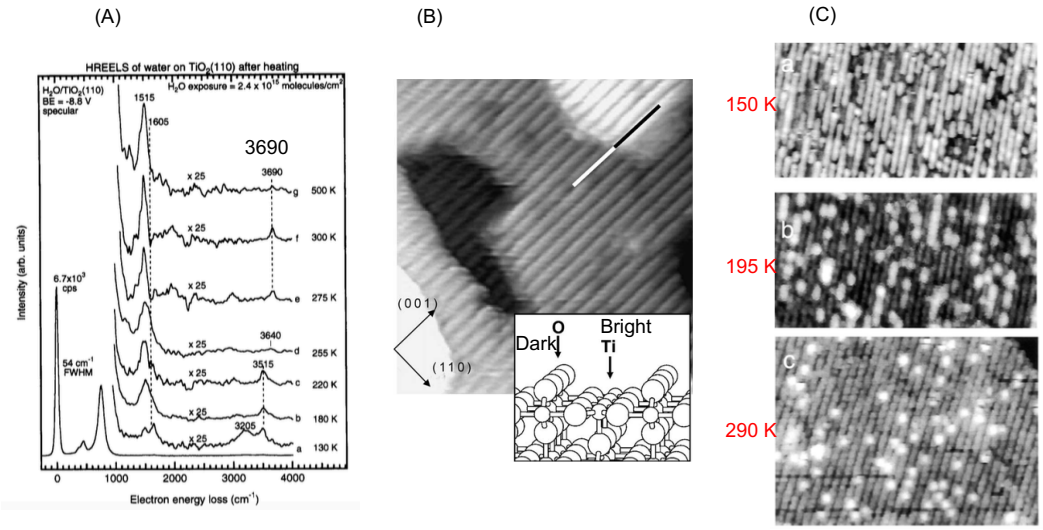

Figure 2.3. Fundamental surface science studies on the TiO_2 rutile (110) surface. (A) vibrational frequency of the rutile (110) surface revealed by high resolution electron energy loss spectroscopy (HREELS), adapted with permission from Henderson et al.[80] (B) STM image of rutile (110) surface showing Ti and O rows, reproduced with permission from Diebold et al.[43] (C) STM images of rutile (110) surface recorded at different temperatures showing the presence of water and surface hydroxyls on the surfaces as bright spots. The STM image recorded at 290 K contains only surface hydroxyls which reveals that surface hydroxyls on rutile (110) surface have bridging character, adapted with permission from Brookes et al.[82]

2.2. Experimental and theoretical methods

Three TiO_2 samples were studied in this work, which have been characterized for specific surface area and crystal phase as reported previously.[68] Pyrogenic TiO_2 (P90) was purchased from Evonik and used as-received. Rutile was purchased from US Research Nanomaterials and used as-received. Commercially available anatase samples contain sulfate impurities, which complicates the interpretation

of spectral results, so we synthesized sulfate-free anatase using a modified sol-gel method described elsewhere.[83] Briefly, to 50 ml of 100% ethanol in a 100 ml three-neck round-bottom flask in ice, we added 2.89 ml of $TiCl_4$ dropwise with a pressure equalized addition funnel. Once addition of $TiCl_4$ was completed, the reaction was stirred at ambient condition for 2 hours. The reaction mixture was placed in an oven at 87 °C and heated for three days. The powder was rinsed by addition of milli-Q water and centrifuged at 20,000 rpm for 30 minutes, several times every day for 30 days until the pH of the supernatant was around 7.

The bulk crystal phase of the rutile, sulfate-free anatase, and P90 (95% anatase, 5% rutile) materials was confirmed with x-ray diffraction and the specific surface areas (P90 100 m^2/g; rutile 30 m^2/g; sulfate-free anatase 159 m^2/g) will be reported in Chapter 4.[68]

DRIFT spectra were recorded using a Nicolet 6700 Fourier Transform Infrared (FTIR) spectrometer equipped with a Praying Mantis™ (Harrick Scientific Production, IBC) accessory for DRIFTS applications. KBr powder was placed in the sample cup inside a Harrick Scientific high temperature reaction chamber (HVC). The HVC sample cup is located on a temperature-controlled sample stage equipped with a cartridge heater and a chromel-alumel (K-type) thermocouple. The temperature of the sample cup is controlled by a Harrick Scientific Automatic Temperature controller (ATC-024-1). Based on work by Couble et al.[84] analysis performed by DRIFTS gives better agreement with volumetric and transmission IR measurements for adsorption using pseudo-absorbance units than with Kubelka-Munk units; see also a review paper by Meunier.[85] Therefore, spectra were presented in absorbance units.

The TiO_2 samples were spread on the top of KBr powder in the sample cup for DRIFTS studies. After KBr or each material spread on KBr was loaded in the chamber, the environmental chamber was heated to 70 °C overnight under flowing O_2 (Grade 2, Matheson), and dried to achieve water vapor pressures estimated to be in the 10^{-10} torr range (Appendix A). Water and carbon dioxide impurities in the O_2 were removed using a molecular sieve trap (13X, 4 to 8 mesh, Acros Organic, degassed at 200 °C for

at least one day) immersed in a dry ice-acetone bath. All DRIFTS spectra were recorded under dry O_2 flow by accumulation of 512 scans at 8 cm^{-1} resolution using a DTGS detector.

Density functional theory (DFT) calculations were carried out using the Vienna Ab-initio Simulation Package (VASP) in combination with the Atomic Simulation Environment (ASE)[86-89] by collaborators at the University of Houston*. The projector augmented wave (PAW)[90] method and the generalized gradient approximation (GGA) with the revised Perdew−Burke−Ernzerhoff (RPBE) functional were employed to solve the Kohn−Sham equations.[91-92] All DFT calculations were performed with a cutoff energy of 400 eV and a Gaussian smearing of kBT = 0.1 eV with subsequent extrapolation of the total energies to kBT = 0 eV.[93] To correct for on-site Coulombic interaction of the localized Ti 3d state, we used the DFT+U approach by Dudarev et al. with Ueff = 2.0 eV.[94] This value is in good agreement with the value obtained by Hu and Metiu.[95]

The optimized lattice constants for rutile TiO_2 are *a = 4.712 Å*, *c/a = 0.640*, and *u = 0.306*, in good agreement with experimental data.[96-97] The rutile TiO_2(110) surface was represented in a 5 x 4 periodic unit cell with four TiO_2 layers, of which the top two layers were fully relaxed, while the bottom two layers were fixed at their bulk positions. Subsequent slabs were separated by 16 Å of vacuum space in the z direction, a dipole correction was applied to compensate for the effect of adsorbing molecules only on one side of the surface,[98] and spin polarization was included. The Brillouin zone was integrated using a (2 x 2 x 1) Monkhorst−Pack mesh,[99] and geometries were optimized using a force convergence criterion of 0.05 eV/Å. Convergence with respect to the k-point set and the force criterion were confirmed.

The binding energies of stable intermediate states (E_{BE}) were calculated with respect to the clean surface and gas phase reference molecules according to $E_{BE} = E_{slab+adsorbate} - (E_{slab} + E_{gas})$, where $E_{slab+adsorbate}$ is the total energy of the slab with adsorbates; E_{slab} is the energy of the clean surface; and E_{gas}

* Calculations were performed by Juan Manuel Arce-Ramos and Lars Grabow.

is a gas phase reference state based on phenol, water, and hydrogen. All reported DFT energies are electronic energies at T = 0 K unless otherwise noted.

2.3. Results

We have performed DRIFTS studies of the titania samples as well as DFT calculations of the surface structure, vibrational frequencies, and thermal stability of the surface hydroxyls.

2.3.1. DRIFTS

DRIFTS experiments were performed during the pretreatment and after the surface was cleaned from surface impurities to observe hydroxyls bands without interference of the impurities. We have also studied the surface hydroxyls that are formed upon hydrogen dissociation on the TiO_2 surface.

2.3.1.1. Pretreatment

Hadjiivanov *et al.* [36] in their review paper on the surface chemistry of anatase TiO_2 determined that there are at least 12 distinct surface hydroxyls reported for anatase TiO_2 and a precise interpretation of the observed patterns is still missing. A recent assessment of the surface hydroxyls of anatase and rutile TiO_2 shows that not much has improved and contradictory results have been reported by different authors.[100] Some of the reported surface hydroxyl bands for anatase are from surface impurities or are due to interactions with impurities such as water, carbonate, bicarbonate, and sulfate species that are commonly found on TiO_2 surfaces.[36] Hence, we developed procedures to clean and dehydrate the TiO_2 surface so that only hydroxyls characteristic of the exposed facets remain. To find the optimum pretreatment temperature, we performed step-wise temperature-programmed calcination of the samples from 30 °C to 400 °C for each sample in the environmental chamber while DRIFTS spectra were recorded. Samples were maintained at elevated temperatures for at least 8 hours under flowing dry oxygen.

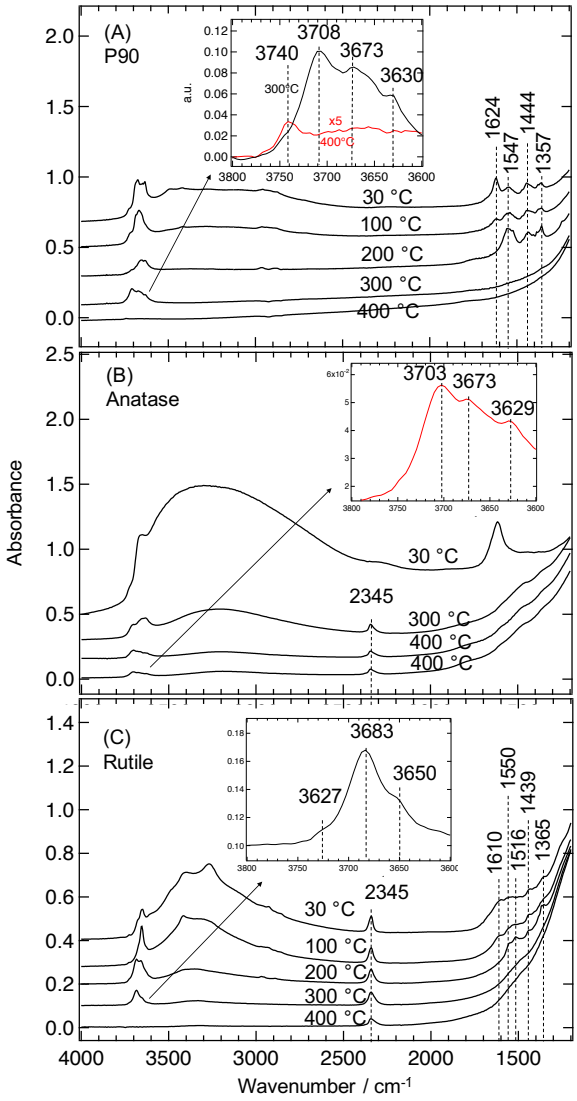

Figure 2.4. DRIFTS spectra of the TiO_2 samples, (A) P90, (B) anatase, and (C) rutile recorded during stepwise temperature programmed calcination from 30 to 400°C, as indicated.

The DRIFTS spectrum of P90 recorded at room temperature (Figure 2.4-A) contained several absorbances caused by surface impurities. The bands at 1357, 1444, and 1547 cm^{-1} are assigned to carbonate and bicarbonate species.[61] The 1624 cm^{-1} band is assigned to the bending mode of molecularly adsorbed water. [48, 80] The broad absorption in the 2500-3600 cm^{-1} region is characteristic of hydrogen bonded surface hydroxyls and hydrogen bonded water molecules. The complex feature in the 3600-3800 cm^{-1} region is characteristic of surface hydroxyl groups and water molecules coordinated to Lewis acid sites, as will be discussed below.[42, 48]

DRIFTS spectra showed that the surface is dehydrated at 200 °C, as evidenced by the elimination of the water bending band and the broad absorption feature in the 2500-3600 cm^{-1} region (Figure 2.4-A), which is consistent with previous reports.[42, 46] The carbonate bands were eliminated from the spectrum at 300 °C. In addition, the 3708 cm^{-1} band grows in intensity as the surface impurities are removed. At this temperature only three significant bands were resolved in the isolated hydroxyl region at 3630, 3673, and 3708 cm^{-1}. After overnight calcination at 400 °C, these bands were largely eliminated from the spectra, and only a small band at ~ 3740 cm^{-1} was observed (inset of Figure 2.4-A). The vibrational frequency and high thermal stability of the latter band are consistent with previous assignments of this band to silica impurities.[101-102] This assignment is also supported by XPS analysis of P90, which shows the presence of silica impurities.[34] Thus, the P90 surface remained contaminated at temperatures below 300 °C, and the surface dehydroxylated at temperatures above 300 °C, although the dehydroxylation temperature should depend on the partial pressure of water and is different for each crystallographic facet (*vide infra*). Under the conditions used in this study, 300 °C was considered optimal.

Because pyrogenic TiO_2 consists of individual anatase and rutile particles, samples of pure anatase and rutile were evaluated as well. Similar step-wise temperature-programmed calcination experiments as that of P90 were performed for the anatase (Figure 2.4-B) and rutile (Figure 2.4-C) samples. At room temperature, the DRIFTS spectrum of anatase shows strong absorbance in the 2500-3600 cm^{-1} region, indicating that the surface is highly hydroxylated making it hydrophilic and therefore

retaining molecular water, as confirmed by the strong bending mode (1620 cm^{-1}) (Figure 2.4-B). Calcination at higher temperatures led to a reduction in the broad absorption feature in the 2600-3600 cm^{-1} region. However, this feature was not eliminated even after several days of calcination at 400 °C, in contrast to P90. Isolated hydroxyl bands at 3629, 3675, and 3703 cm^{-1} also persisted in the spectra during the calcination at 400 °C. These bands must be due to surface hydroxyls because the water bending band was eliminated at 200 °C. The differences in hydroxylation between anatase and P90 may be due to the synthesis methods for each. It is known that the surface of TiO_2 samples prepared at low temperature in the presence of water, as during the hydrolysis of $TiCl_4$, are extensively hydroxylated; while such surfaces undergo irreversible dehydroxylation during drying, some hydroxyls persist on the surface and remain even after evacuation at 700 °C.[36] Conversely, the surface of TiO_2 samples prepared at high temperature in the absence of water (*e.g.*, P90) are largely dehydroxylated as-synthesized.[36]

DRIFTS spectra recorded during the step-wise temperature-programmed calcination of rutile are shown in Figure 2.4-C. Water and carbonate bands were eliminated from rutile after overnight calcination at 300 °C, and a broad absorption feature for the H-bonded surface hydroxyls was observed in the 2500-3600 cm^{-1} region, as were three bands for isolated hydroxyls at 3727, 3683, and 3652 cm^{-1} (See inset of Figure 2.4-C). Similar bands were previously reported for rutile powder samples.[71, 103-104] The isolated hydroxyl bands were eliminated after overnight calcination at 400°C.

There was a band at 2345 cm^{-1} which appeared in the DRIFTS spectra of anatase and rutile but not the spectra of P90, and it persisted after overnight calcination at 400 °C. While this band could be due to the asymmetric stretching mode of linear CO_2 molecules coordinated to Lewis acid sites on the TiO_2 surface,[61] CO_2 molecules coordinated to Ti^{4+} sites persist on the surface at room temperature only under CO_2 atmosphere.[61] Hence, this band must have originated from the CO_2 molecules trapped in the structure, as previously reported for silica.[105]

2.3.1.2. Hydroxyl bands

Figure 2.5 shows the DRIFTS spectra of the TiO_2 samples recorded at 300 °C and after the temperature was returned to room temperature under dry O_2 flow. For P90, the decrease in temperature led to: an increase in the intensity of the $\upsilon\ (O-H)$ bands; blue shifts of the bands at 3708 and 3629 cm^{-1} by 10 and 12 cm^{-1}, respectively; no change in the frequency of the band at 3673 cm^{-1}; an absorbance at 3687 cm^{-1} was resolved from other absorbances. The anatase TiO_2 sample behaved similarly to the P90 sample, except that the 3687 cm^{-1} band was absent (Figure 2.5-B). The intensity of the $\upsilon\ (O-H)$ bands increased for the rutile TiO_2 sample and the absorbances at 3683 and 3650 cm^{-1} blue shifted by ~12 and 10 cm^{-1}, respectively (Figure 2.5-C).

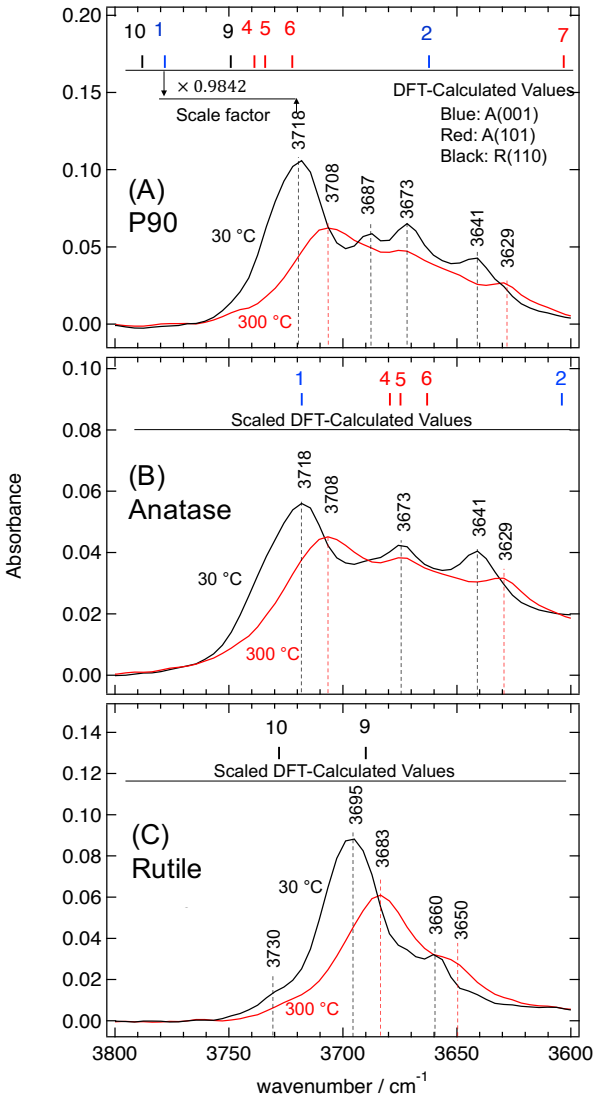

Figure 2.5. DRIFTS spectra of A) P90 , B) anatase, and C) rutile in the hydroxyl region recorded at 300 °C (red spectra) and 30 °C (black spectra). Symbols on the top of (A) show the DFT-calculated vibrational frequency of hydroxyls on the anatase (001) surface (blue), anatase (101) surface (red), and rutile (110) surface (black), as summarized in Table 2.2. Symbols (and numbers) on the top of (B) and (C) show the predicted vibrational frequencies of anatase and rutile hydroxyls after scaling the DFT-calculated values (see Discussion).

Now, we compare the spectral behavior of the surface hydroxyls of pyrogenic TiO_2 collected in this work with information available in the literature. A summary of the $\upsilon\ (O-H)$ values from the literature for P25 pyrogenic TiO_2 samples observed on reasonably dry surfaces is presented in the first five columns of Table 2.1, illustrating the lab-to-lab reproducibility of the measured frequencies. To observe the

surface hydroxyl bands of TiO_2, prior pretreatment at higher temperatures is required.[47, 106] We observed that surface hydroxyl bands undergo significant transformations at 300 °C, when carbonate species are eliminated. Two of the $\upsilon\ (O-H)$ frequencies observed in this study for P90 at 300 °C (3629 and 3708 cm^{-1}) are slightly lower than those reported for P25 in Table 2.1. However, it must be noted that the reported P25 values summarized in Table 2.1 were recorded at room temperature, after initial pretreatment at higher temperatures. Spectra recorded at 300 °C were at a sufficiently high temperature to prevent adsorption of water on the surface, but under our conditions negligible uptake of water could have occurred during cooling to 30 °C. The values of $\upsilon\ (O-H)$ measured for P90 at 30 °C were consistent with the P25 reported values within ±2 cm^{-1}.

Table 2.1. Comparison of $\upsilon\ (O-H)$ values of the pyrogenic TiO_2 P25 with P90.

P25					P90		[a]Assignments
Panayotov[65]	Lobo-Lapidus [66]	Nanayakkara [46]	Deiana [47]	Lin[106]	This Work (300 °C)	This Work (30 °C)	
-	-	3733	3736	3734	3740	3740	SiO_2
3716	3717	3717	3717	3715	3708	3717	OH_{tr} A(001)
3688	3689	3691	3688	3688	-	3688	OH_{br} R(110)
3674	3672	3672	3672	3671	3673	3673	OH_{br} A(101)
3660	-	-	3659	3658	-	-	[b]NA
3648	3642	3642	3642	3640	3629	3641	NA

[a] See the Discussion section for the assignments, [b]Not assigned

2.3.1.3. Hydroxyls formed by reaction with H_2 (D_2)

To demonstrate the formation of surface hydroxyls from dissociation of H_2 independent of the adsorption of background water, we performed our experiments under rigorously dry conditions and at 300 °C. Before exposure to H_2, we cleaned the TiO_2 samples by calcination at 400 °C under dry O_2 for at least 8 h. The state of the surface after such pretreatment can be inferred from the spectra depicted in Figure 2.4. We achieved highly dehydroxylated surfaces for P90 and rutile with no detectable impurities, except traces of SiO_2, but the anatase sample remained slightly hydroxylated. Spectra depicted in Figure

2.6 were recorded during the reaction of such surfaces with H_2 at 300 °C. Previous reports show that H_2 dissociates on pyrogenic titania (P25) above 250 °C to yield electrons and protons.[107] The protons bond to surface oxygens (to form hydroxyls) and the electrons accumulate in the CB and mid-gap states.[69-70, 108] We observed a broad electronic absorbance feature and hydroxyl stretching bands for all these samples after reaction with H_2 at 300 °C.[68] By comparison with Figure 2.5, H_2 dissociated to form only certain hydroxyls. Reaction of the P90 surface with H_2 at 300 °C generated two bands at 3675 and 3645 cm^{-1} Figure 2.6-A. The anatase BC sample contained three bands at 3630, 3673, and 3708 cm^{-1} before exposure to H_2 but, as the difference spectrum in Figure 2.6-B shows, the two overlapping bands that appear at 3673 and 3645 cm^{-1} are the same bands as found for P90, which is consistent with the 95% anatase content of P90. Reaction of the dehydroxylated rutile surface with H_2 produced two bands at 3683 and 3665 cm^{-1}, which were both present during dehydroxylation at 300 °C.

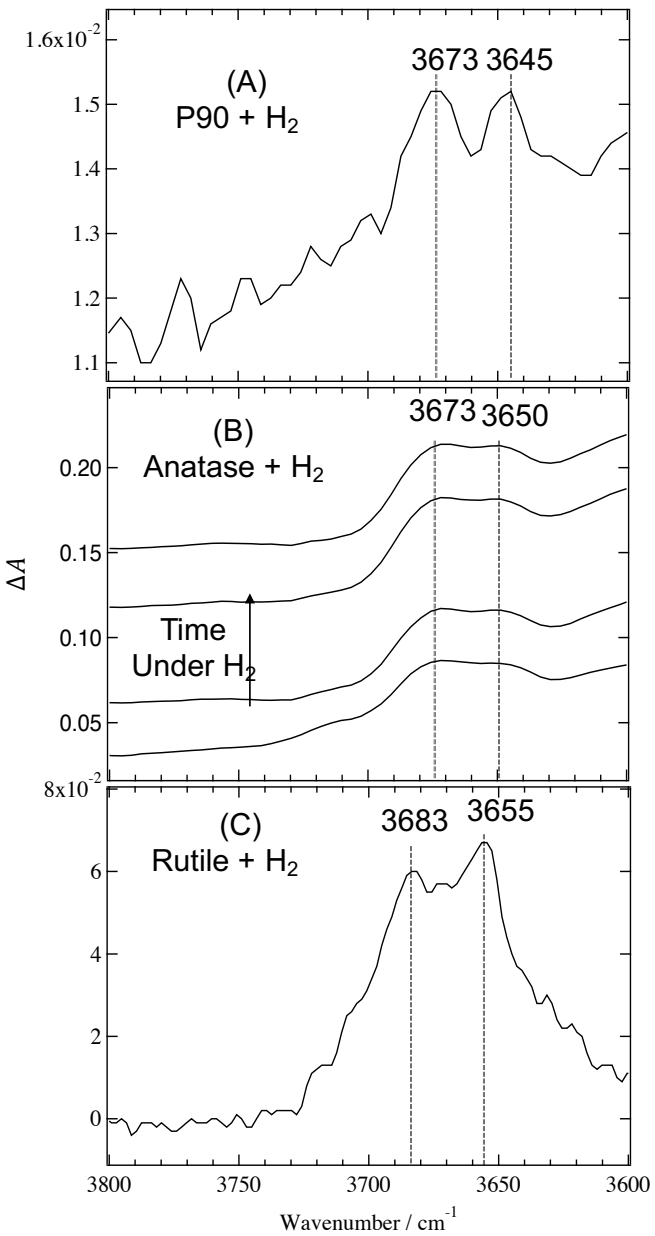

Figure 2.6. Difference DRIFTS spectra of A) P90, B) anatase, and C) rutile in the hydroxyl region recorded during the reaction of the 400 °C dehydroxylated TiO_2 samples with H_2 at 300 °C. All the spectra are relative to the DRIFTS spectrum of the sample recorded under Ar right before exposure to H_2. Surface hydroxyls formed by H_2 dissociation only on selected facets of the P90, anatase and rutile surfaces.

Reaction of the hydroxylated anatase surface with D_2 gave us further insight on how surface hydroxyls are preferentially formed upon hydrogenation. Figure 2.7-A shows that, in addition to the broad electronic absorption, H/D exchange resulted in negative-going bands in the OH region and positive-

going bands in the OD region. Comparison of the expanded spectra in Figure 2.7-B and -C shows that initially, the relative intensities of the negative-going OH bands are similar to the corresponding positive-going OD bands. The relative intensity of the OH bands remained unchanged during the reaction, although they shifted upwards due to the increasing electronic absorbance background. However, at longer times, the relative intensity of the 2704 cm^{-1} OD band increased, indicating that D_2/H_2 dissociation occurred preferentially on one facet (corresponding to the 3670 cm^{-1} hydroxyl). The continuous growth of the broad electronic absorption feature shows continuous addition of electrons to the shallow trap states of anatase TiO_2 (Chapter 4) as OD groups are formed and dehydroxylation to produce oxygen vacancies occurs, maintaining a steady state OD coverage.

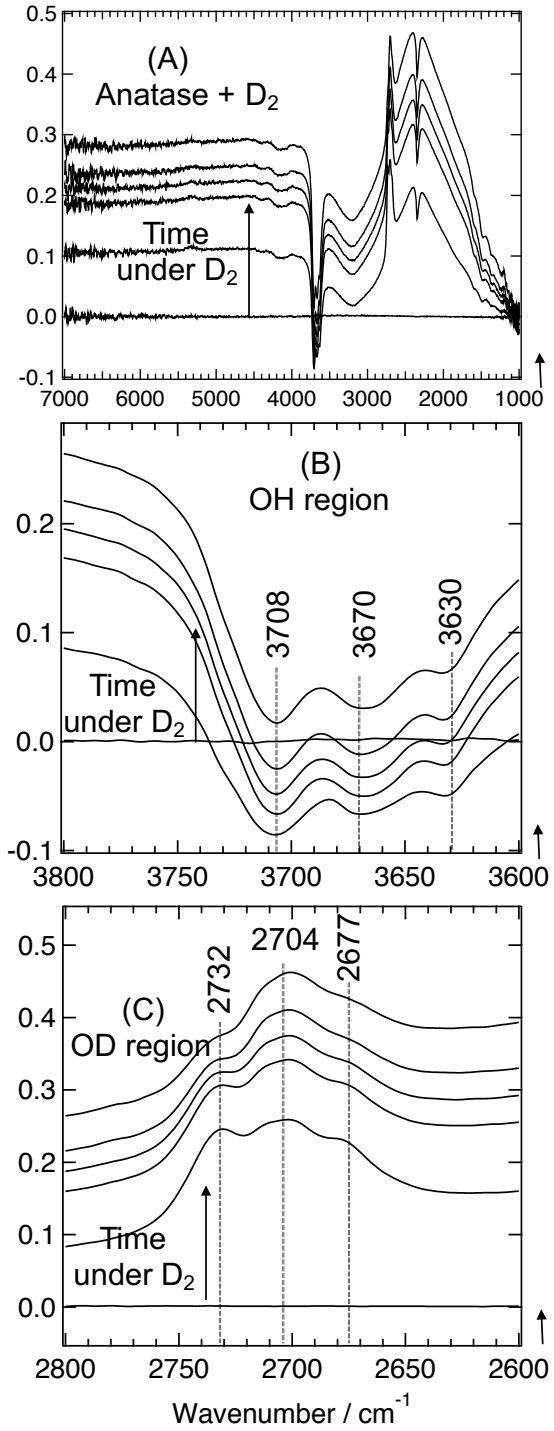

Figure 2.7. Difference DRIFTS spectra recorded during the reaction of anatase with D_2 at 300 °C. (A) overall spectra showing both vibrational and broad electronic absorbance features upon H/D exchange; (B) OH region showing negative-going bands and (C) OD region showing that in addition to the initial H/D exchange, the band at 2704 cm^{-1} continues to grow, which corresponds to the hydroxyl at 3670 cm^{-1}.

2.3.2. DFT calculations

Previous work by Arrouvel et al.[42] provides extensive information regarding the coverage dependent structures of water or hydroxyls formed upon adsorption of water on the stoichiometric anatase (001), (100), (110), and (101) surfaces, and surface free energy calculations used to predict phase diagrams, i.e. the equilibrium coverage of hydroxyls as a function of temperature and water vapor pressure. Because it is known experimentally[79, 109] and theoretically[77-78] that water can dissociate on oxygen vacancies on the (101) and (001) surfaces or H_2 could adsorb dissociatively at defects[110] on the stoichiometric surface to form hydroxyls, and to make direct comparison with the calculations of Arrouvel et al.,[42] we focused our DFT calculations on the (101) and (001) facets of anatase and the (110) facet of rutile. The anatase (101) and (001) facets are the stable facets from the Wulff construction for both the stoichiometric and hydrated or hydroxylated anatase surfaces.

2.3.2.1. Surface structures

Figure 2.8-A and -B show the optimized surface structure of the two anatase faces with stoichiometric terminations. On the anatase (001) face (Figure 2.8-A), all surface Ti atoms are five-coordinate (Ti_V); while on the anatase (101) facet (Figure 2.8-B), the topmost layer exposes five- and six-coordinate Ti atoms (Ti_V, and Ti_{VI}). Both facets contain both three- and two-coordinated surface oxygens (O_{3c}, and O_{2c}). The O_{2c} sites on both surfaces are more exposed compared to the O_{3c} sites. Selected Ti–O bond lengths of the optimized surfaces are also shown in Figure 2.8.

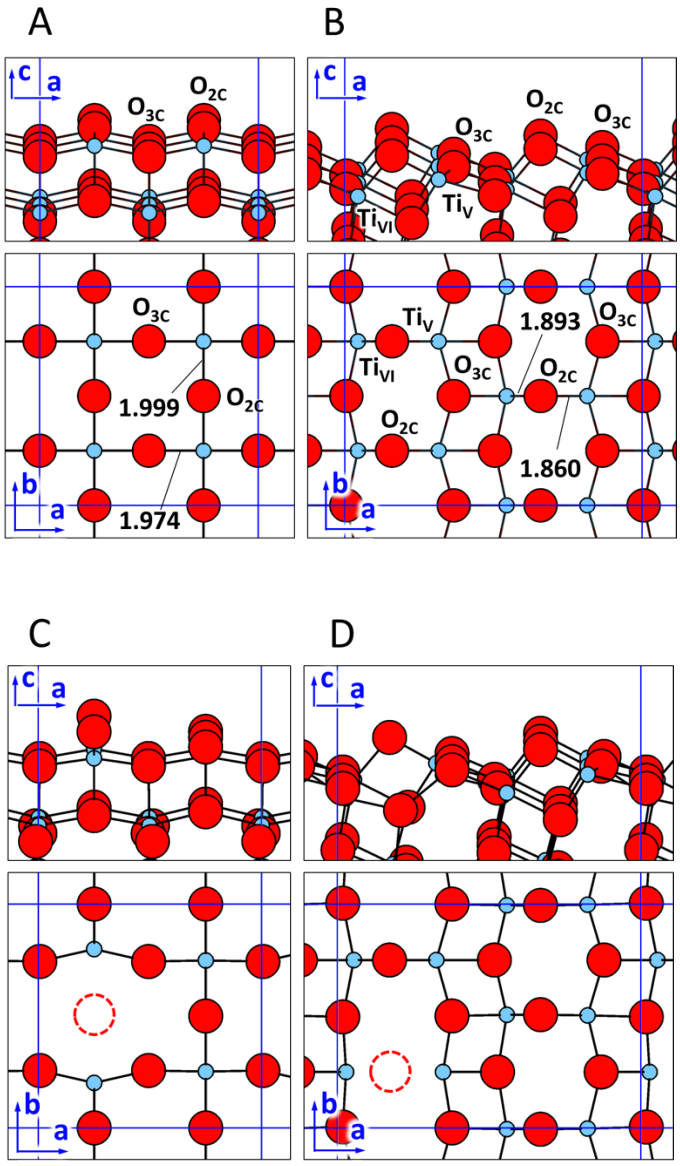

Figure 2.8. Side and top views of the optimized configurations of the stoichiometric anatase A) (001) and B) (101) surfaces, and surfaces with oxygen vacancy created by removing an O_{2C} from the C) (001) and D) (101) faces, at locations indicated by the red dashed circle. Ti and O atoms are shown in blue and red, respectively. Only surface atoms are shown in the top view for clarity. Bond lengths are expressed in Ångstroms. Limits of the periodic cell are shown in black dashed lines.

Figure 2.8-C and -D shows optimized structures for the defected (001) and (101) faces (i.e. a surface containing oxygen vacancies). In the case of the (001) face, the formation of the oxygen vacancy at the O_{2C} site leads to a relaxation of the exposed Ti atoms towards the closest O_{2C} to partially heal the

under-coordination caused by the removed oxygen. Similarly, the removal of an O_{2C} oxygen from the (101) surface causes the neighboring Ti atoms to move towards the O_{3C} atoms in the direction opposite to the vacancy. The direct removal of a bridging surface oxygen from the (001) facet to produce gas phase ½(O_2) requires 3.59 eV, which can be compared to a previous calculation by Guo, et al.[111] of 4.09 eV for the unreconstructed (001) surface. While a (1x4) reconstruction is known for the anatase (001) surface[112-113], there is clear evidence that the unreconstructed structure exists at low temperatures on nanocrystals,[114] but reconstructs between 400 and 600 °C.[115] The same process on the (101) requires 4.15 eV, which is identical to previous results on the anatase (101) surface, [116] but the estimated defect creation energy is 5.08 eV at the sX-LDA level.[117] For both anatase 1x4 (001) and (101), subsurface oxygen vacancies are more stable[116-117] and oxygen vacancy diffusion is facile. [116] These values are generally larger than the surface vacancy creation energy of 3.68 eV on the rutile (110) surface.[116]

Dissociative adsorption of water at the vacancy sites and migration of a proton can lead to formation of two hydroxyl groups. Figures 2.9-b, 2.10-a, and 2.10-c display the structures of selected surfaces with two hydroxyls, while the calculated vibrational frequencies of the O–H stretching modes is presented in Table 2.2. The influence of the local environment around the OH groups was also studied by considering structures containing a single hydrogen adatom per cell (Figure 2.9-c and 2.10-b) to simulate a partially dehydroxylated surface. For direct comparison with the energy and frequencies reported by Arrouvel et al.,[42] Figure 2.10-a shows the structure produced by dissociative adsorption of H_2O via a hydrolysis process on the stoichiometric (001) face. The configurations and hydroxylation coverage ($\theta = H/O_{2c}$ratio) included in Figures 2.9 and 2.10 are as follows: (2.9-a) H_2O dissociation via hydrolysis on the stoichiometric (001) surface ($\theta = 0.25$); (2.9-b) H_2O dissociation at an oxygen vacancy on the (001) surface ($\theta = 0.25$); (2.6-c) H adsorption over the stoichiometric (001) surface ($\theta = 0.125$); (2.10-a) H_2O dissociation over an oxygen vacancy (O_{2c}) of the (101) surface ($\theta = 0.167$); (2.10-b) H adsorption over the stoichiometric (101) surface ($\theta = 0.0625$); (2.10-c) H_2O dissociation over an oxygen vacancy of the

(101) surface ($\theta = 0.167$). For comparison to experimental and theoretical literature values, we also calculated the structures and frequencies of bridging hydroxyls on the rutile (110) surface at coverages corresponding to $\theta = 0.33$ and $\theta = 0.66$ (structures not shown).

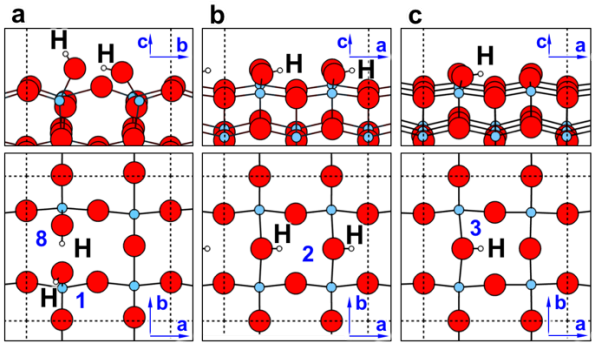

Figure 2.9. Hydroxylated surfaces of the (001) face of anatase. a) water dissociation via hydrolysis of the stoichiometric surface to form two terminal OH groups; b) water adsorption onto a surface oxygen vacancy to form two bridging hydroxyls; and C) a single bridging hydroxyl for evaluation of coverage dependent frequency shifts. Only surface atoms are shown in the top view for clarity. Atom color code is the same as in Figure 2.8 with hydrogen atoms being displayed in small white circles.

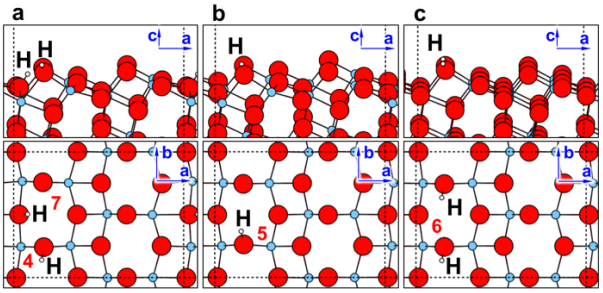

Figure 2.10. Hydroxylated surfaces of the (101) facet of anatase, which could be formed either by adsorption of H_2 on the stoichiometric surface or via water dissociative adsorption at an O_{2c} vacancy and migration of the proton to form A) a bridging hydroxyl at O_{2c} and a bridging hydroxyl at a neighboring O_{3c}; B) a single bridging hydroxyl at the O_{2c} site and C) two bridging hydroxyls at O_{2c} sites for comparison of the hydroxyl frequency at low coverage. Only surface atoms are shown in the top view for clarity. Atoms color code is the same as in Figure 2.8 with hydrogen atoms being displayed in small white circles.

The relative energies for dissociative adsorption of H_2 on the stoichiometric (001) and (101) surfaces to form two surface hydroxyls and the dehydroxylation to form H_2O and a surface oxygen vacancy are shown in Figure 2.11. These energies are referenced with respect to the energy of the most

stable hydroxylated state (with two H per cell shown in Fig. 2.9-b and 2.10-c), to illustrate the energy required or produced during adsorption of H_2 and required for dehydroxylation. The hydroxylated state is the lowest in energy for the (001) facet, and is thermodynamically favorable to relatively high temperatures (see Section 2.3.2.3 below). By contrast, desorption of H_2 from the hydroxylated (101) surface to yield the stoichiometric termination is favored energetically. As shown by Aschauer and Selloni's DFT calculations,[118] the associative desorption of H_2 from the (101) surface of anatase (Figure 2.10-c) is kinetically limited by activation barriers in the range of 1.8 to 2.0 eV, decreasing at higher hydroxyl coverage.[118]. The energy required for dihydroxylation is in good agreement with the 1.2 eV value Aschauer and Selloni reported[118] for oxygen vacancy defect creation with no additional activation energy barrier. Therefore, although desorption of hydrogen that leads to a stoichiometric (101) anatase surface is thermodynamically favored, loss of hydroxyls is thought to be kinetically limited with dehydroxylation being the lowest energy barrier, followed by diffusion into the bulk, and then desorption of H_2 least accessible. Thus, observation of the hydroxylated (101) surface at low temperatures is possible.

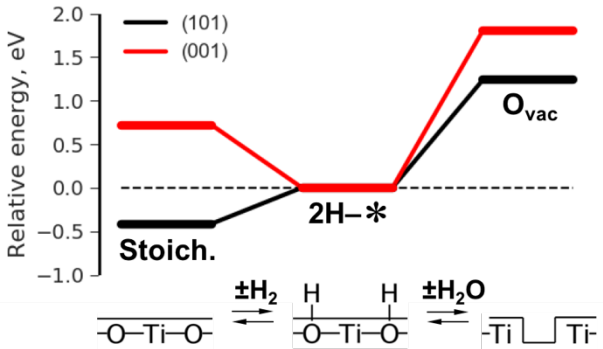

Figure 2.11. Relative energy of different structures of the (001) and (101) surfaces. From left to right: H_2(g) + stoichiometric surface; hydroxylated structures for (001) corresponding to two bridging hydroxyls as shown in Fig. 2.9-b and for (101) as shown in Fig. 2.10-c; H_2O(g) + surface with oxygen vacancy.

2.3.2.2. Vibrational frequencies

The calculated bond lengths and vibrational frequencies of the TiO_2 hydroxyls studied in this work are summarized in Table 2.2. These frequencies decrease linearly with the O–H bond length regardless of the coordination of the oxygen atom involved in the bond (Figure 2.12), which is consistent with previous reports.[75].

Table 2.2. Calculated $\upsilon(O-H)$ and $\upsilon(O-D)$ on the (001) and (101) facets of anatase. Coverage of hydroxyls groups and bond lengths for O–H are also included. Scaled frequencies shown in parentheses (See Discussion).

ID	Phase	Facet	Type	θ	Bond length $(O-H)$, Å	$\upsilon(O-H)$ cm^{-1}	$\upsilon(O-D)$ cm^{-1}
1	ana	(001)	O_{1c}–H	0.5	0.9710	3778.1(3718)	2749.6
8	ana	(001)	O_{1c}–H	0.5	1.0107	2896.0(2850)	2116.7
2	ana	(001)	O_{2c}–H	0.5	0.9777	3662.2(3604)	2666.2
3	ana	(001)	O_{2c}–H	0.25	0.9814	3597.7(3541)	
4	ana	(101)	O_{2c}–H	0.25	0.9733	3738.8(3680)	
5	ana	(101)	O_{2c}–H	0.25	0.9740	3734.1(3675)	
6	ana	(101)	O_{2c}–H	0.5	0.9743	3722.2(3663)	2707.8
7	ana	(101)	O_{2c}–H	0.25	0.9801	3603.1(3546)	
9	rut	(110)	O_{2c}–H	0.66	0.9717	3749.2(3690)	
10	rut	(110)	O_{2c}–H	0.33	0.9701	3788.0(3728)	

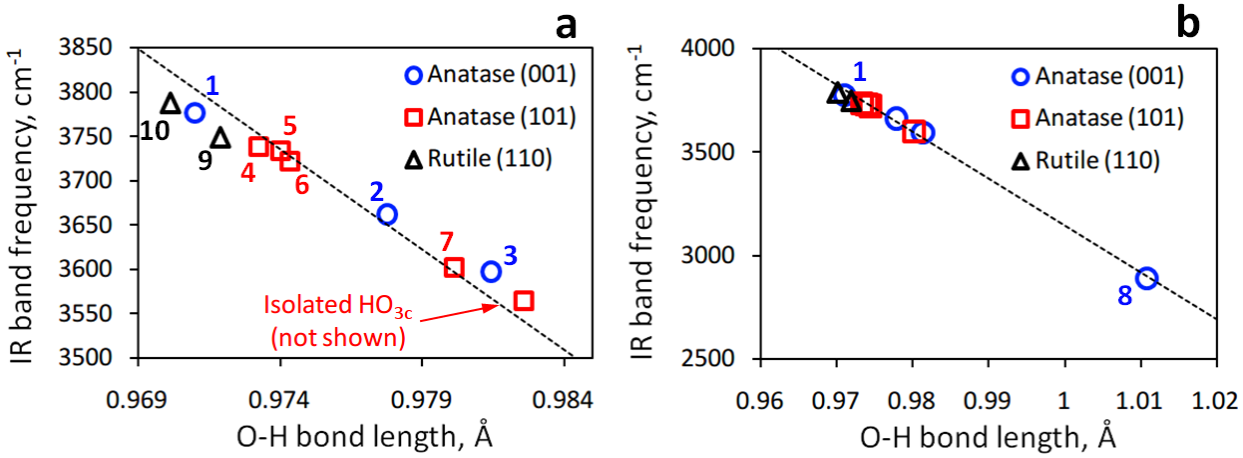

Figure 2.12. The O-H stretching frequency of surface hydroxyls as function of the O-H bond length (a). A wider view is also provided to include the hydroxyl group with the greatest bond length (b). All the anatase hydroxyls considered in the plots are shown in Figures 2.9 and 2.10. Vibrational frequencies of hydroxyls over the (110) facet of rutile at two coverage (1/3 and 2/3) are also shown for comparison.

On the (001) facet, hydroxyls 1 and 8 (Figure 2.9-a) are formed from water dissociation, as reported by Arrouvel, et al.[42] During this process, a hydroxyl from water sits over a Ti_V site while one lattice O_{2c}-Ti_V bond breaks and forms an additional terminal hydroxyl (O_{1c}-H) with the remaining proton from water. The new OH groups are hydrogen-bonded to each other. While hydroxyl 1 is a H-bond acceptor group, hydroxyl 8 is a H-bond donor. The donor and acceptor character of the OH groups change their bond lengths and, consequently, the corresponding vibrational frequencies. The calculated bond length of the hydroxyls 1 and 8 are 0.971 and 1.011 Å and the corresponding calculated vibrational frequencies are 3778 and 2896 cm^{-1} respectively. Our frequency of 3778 cm^{-1} is higher than that of Arrouvel, et al.[42] (3760 cm^{-1}) because they included anharmonic corrections.

A comparison of the calculated O–H stretching frequencies summarized in Table 2.2 illustrates the influence of the local environment on the vibrational frequency of bridging hydroxyls. On the (001) facet, when the coverage of hydroxyls increases from one hydroxyl in the unit cell (hydroxyl 3, Figure 2.9-c) to a pair of hydroxyls (hydroxyl 2, Figure 2.9-b), the O–H bond lengths decreased from 0.981 Å to 0.978 Å and $\upsilon(O-H)$ increased from 3597.7 cm^{-1} to 3662.2 cm^{-1} (64.5 cm^{-1} blue shift). On the anatase

(101) surface, the calculated $\upsilon(O-H)$ for the bridging hydroxyls (O_{2c}-H) were 3738.8 cm^{-1} (hydroxyl 4, Figure 2.10-a), 3734.1 cm^{-1} (hydroxyl 5, Figure 2.10-b) and 3722.2 cm^{-1} (hydroxyl 6, Figure 2.10-c). Surprisingly, the increase of the hydroxylation coverage has a different effect in the $\upsilon(O-H)$ of the O_{2c}-H groups of anatase (101) surface depending on the nature of the neighbor hydroxyl. For example, if we use hydroxyl 5 in Figure 2.10-b as a reference, a neighboring O_{3c}-H (Figure 2.10-a) causes a $\upsilon(O-H)$ blue shift while an adjacent O_{2c}-H (Figure 2.10-c) produces a $\upsilon(O-H)$ red shift. On the rutile (110) surface, the calculated frequency for a single hydroxyl in the (1x3) supercell (hydroxyl 10, Table 2.2) is 3788.0 cm^{-1} and the calculated frequency for a pair of hydroxyls in the supercell (hydroxyl 9, Table 2.2) is 3749.2 cm^{-1}. The presence of an adjacent O_{2c}-H group produces a $\upsilon(O-H)$ red shift in the equivalent hydroxyls.

2.3.2.3. Phase diagrams

We used *ab initio* atomistic thermodynamics to determine the stability of the hydroxylated facet structures under a range of reaction conditions, following the approach of Arrouvel, et al.[42] Only the most stable configurations (i.e., those where two hydroxyl groups are formed) were included in these calculations, and only two states that are connected by an adsorption/desorption process are compared at the same time. These results are shown in Figure 2.13. Several possibilities were tested for the (001) surface: the adsorption/desorption of water over the stoichiometric surface (Figure 2.13-a) or over the surface with an oxygen vacancy (Figure 2.13-c); and the adsorption/desorption of hydrogen over the stoichiometric surface (Figure 2.13-b). The phase diagram in Figure 2.13-a compares well with the coexistence curve between $\theta = 0.0$ and $\theta = 1.7\ H_2O/nm^2$ in the more extensive phase diagram of Arrouvel, et al.[42] (their Fig. 16b). For the (101) facet, only the states involved in the adsorption/desorption of water over the surface with an oxygen vacancy was considered (Figure 2.13-d).

As shown in Figure 2.13, both the desorption of water leading to the stoichiometric (Figure 2.13-a) or defected surface (Figure 2.13-c) are predicted to require temperatures higher than 300 °C for P_{H2O} higher than 10^{-5} bar, while the desorption of hydrogen (Figure 2.13-b) leading to the stoichiometric surface is thermodynamically possible at lower temperature and P_{H2}. Whether loss of hydroxyls via associative desorption of hydrogen is more favorable than dehydroxylation under our experimental conditions depends on activation energy barriers that are not currently known. Under the assumption that dehydroxylation of the (101) facet is the most kinetically accessible route to loss of hydroxyls, the phase diagram of Figure 2.13-d predicts that dehydroxylation would be equilibrated at lower temperatures than for the (001) facet at a water partial pressure of 10^{-5} bar. The process in which hydrogen is adsorbed/desorbed from the (101) stoichiometric surface was also examined, but it leads to the desorbed state at all tested conditions.

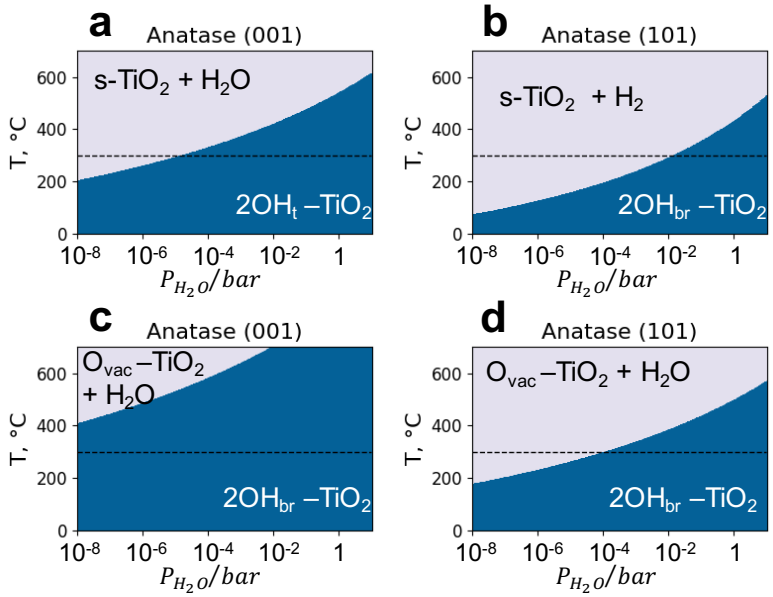

Figure 2.13. Thermodynamic phase diagrams comparing different states in the (001) (a-c) and (101) (d) facets of anatase. Over the (001) facet three states were compared connected through the following processes: (a) desorption of H_2O from the structure of Fig. 2.9-a leading to the stoichiometric surface; (b) desorption of H_2 from the structure of Fig. 2.9-b leading to the stoichiometric surface; and (c) H_2O desorption from the structure of Fig. 2.9b leaving an oxygen vacancy (as in Fig. 2.8-C). Over the (101) facet the corresponding states are connected through the desorption of H_2O from the structure of Fig. 2.10-c forming an oxygen vacancy (as in Fig. 2.8-D). Region in grey represent the conditions at which the dehydroxylated surface is favored, while the blue area represent the hydroxylated state.

2.3.2.4. Reaction with H_2

In an attempt to determine the mechanism of hydrogen dissociation and type of hydroxyls that are formed by reaction of anatase and rutile surfaces with H_2, we performed DFT calculations using the (110) and the (101) surfaces of rutile and anatase. The formation of a vacancy via hydrogen reduction was used as comparison reaction. Figure 2.14 shows the comparison between the vacancy formation process over TiO_2 in both crystalline phases. The results for anatase are completely new while the results for rutile were reported in a previous work.[33] The reaction proceeds first with the dissociative adsorption of hydrogen on two O_{br} sites, followed by the diffusion of a H^+ from one hydroxyl toward the remaining OH group and finally the formation of molecular water needs to occur prior it desorption leaving an oxygen vacancy behind.

From these DFT results, we can conclude that hydrogen adsorption is harder over anatase, and every intermediate involved in the oxygen vacancy formation is thermodynamically unfavorable. Over rutile, the process of vacancy formation is about 1 eV less endothermic than over anatase. In a review published in 2007,[119] the oxygen vacancy formation energy as well as the induced changes in electronic properties in the rutile and anatase phases of TiO_2, were summarized from different sources in literature. They compile mainly theoretical results, and from the available data they collected, it was mentioned that the defect formation energies for anatase systems are in general larger than those for rutile, which is consistent with the experimental observed lower tendency of forming oxygen vacancies on anatase surfaces.

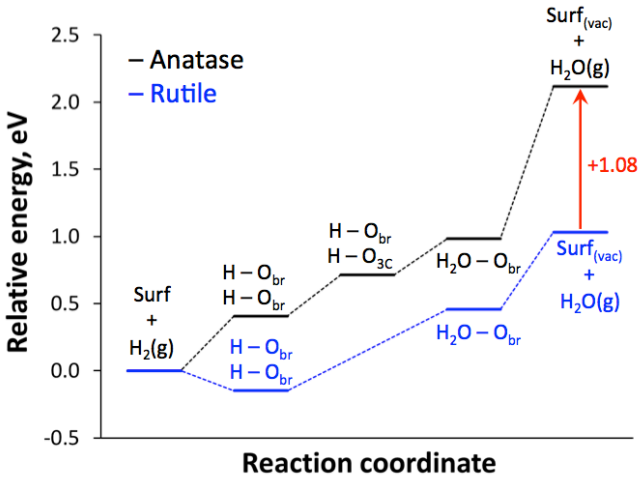

Figure 2.14. Potential energy diagram for the oxygen vacancy formation through the reduction with hydrogen on Anatase (101) and Rutile (110). In both cases, the energy of reference is the sum of the total energy of the stoichiometric slab and the energy of a hydrogen molecule in gas phase.

From these results one might speculate that the dissociation of H_2 at the metal/support interface is harder over Ru/anatase than over Ru/rutile, since hydroxyl groups display less stability over anatase. However, the effect of the supported metal particles has not been taken into account here.

We have also studied the energetics of H_2 adsorption over surfaces with O defects. After the formation of an oxygen vacancy, two electrons are left on the surface causing changes in the chemical properties of the surface. A further reduction of the surface might take place via hydrogen adsorption, but these aforementioned changes could affect the process. For this reason, we decided to study the adsorption of hydrogen over the surface of anatase and rutile containing an oxygen vacancy. First, we obtained the electron density difference (EDD) of both systems (anatase and rutile) while removing one oxygen. The EDD of a system is calculated as shown in the following equation:

$$EDD_{diff} = -\left(EDD_{stoich} - EDD_{surf-vac} - EDD_{Ogas}\right)$$

where EDD_{stoich}, $EDD_{surf\text{-}vac}$ and EDD_{Ogas} are the electron density of the stoichiometric surface, the surface with an oxygen vacancy and the isolated O in gas phase, respectively. Essentially, a difference in the electron density between the reference states is obtained and accumulation or depletion of electrons can

be spotted when a transition from one state (stoichiometric surface) to the other (oxygen vacancy formation) takes place.

In Figure 2.15 is presented the EDD of the oxygen vacancy formation on anatase (101) surface. From this figure, it is clear that by removing an oxygen from the surface, the extra electrons left in the system migrates immediately to the neighboring Ti atoms, reducing them at some extent. In a similar way, over rutile the electrons left by the oxygen atoms after its removal are localized on the adjacent Ti atoms as shown in Figure 2.16.

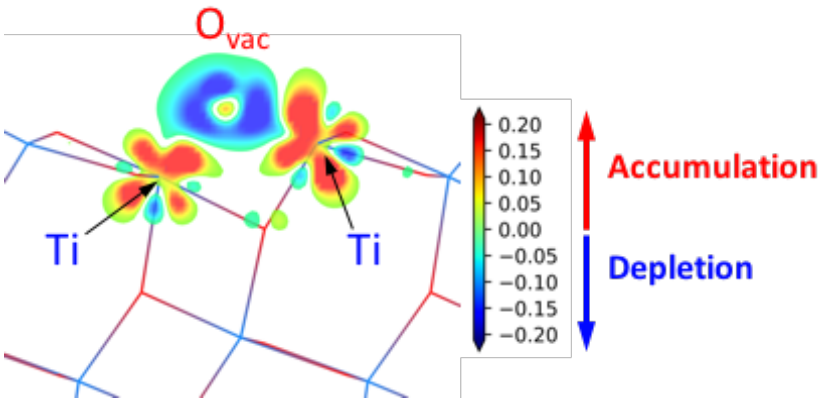

Figure 2.15. Electron density difference of the removal of an oxygen from the surface of anatase (101). Side view oriented in the [010] direction of the slab.

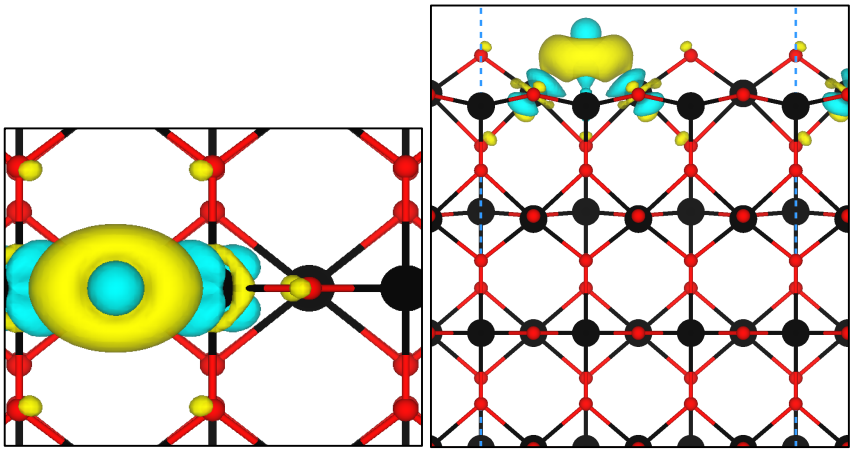

Figure 2.16. Electron density difference of the removal of an oxygen from the surface of rutile (110). The isosurface in yellow show electronic depletion, while blue show accumulation.

After one oxygen is removed from the surface of anatase and rutile, the interaction of hydrogen with these reduced surfaces is quite different. A summary of our finding regarding adsorption energies and modes over the reduced surfaces is presented in Table 2.3. In one hand, over the O-defected rutile surface, two adsorption modes have similar adsorption energies, the heterolytic dissociation forming H-Ti and H-O_{br} bonds (H-Ti_2, H-O_{br} configuration), or the homolytic dissociation forming two H-Obr bonds (H-O_{br}, H-O_{br} configuration). These two configurations have a difference of only 0.1 eV, as can be seen in Table 2.3, and therefore are expected to coexist under suitable conditions. However, note that both processes have different implications regarding the induced electronic effect on the surface. For instance, the heterolytic dissociation of H_2 does not add extra electrons to the surface, while the adsorption over oxygen sites does. Figure 2.17 displays the two most stable configurations for hydrogen adsorption over reduced rutile. The formation of two H-Ti bonds after H_2 dissociation was also explored but this process is less favorable than the mentioned above by at least 0.56 eV.

Table 2.3. Adsorption configurations and energies of hydrogen over surface models with an oxygen vacancy. Depending on the adsorption site, hydrogen might donate or retrieve electrons to or from the surface (transferred electrons).

Surface	**Adsorption configuration**	**ΔE_{ads}, eV**	**Transferred electrons**
Rutile-O_{vac}	H-Ti_2, H-O_{br}	0.094	0
Rutile-O_{vac}	H-O_{br}, H-O_{br}	0.205	+2
Rutile-O_{vac}	H-Ti_2, H-Ti	0.762	-2
Anatase-O_{vac}	H-Ti_2, H-Ti	0.120	-2
Anatase-O_{vac}	H-O_{3fold}, H-Ti_2	0.500	0
Anatase-O_{vac}	H-O_{br}, H-O_{br}	0.504	+2

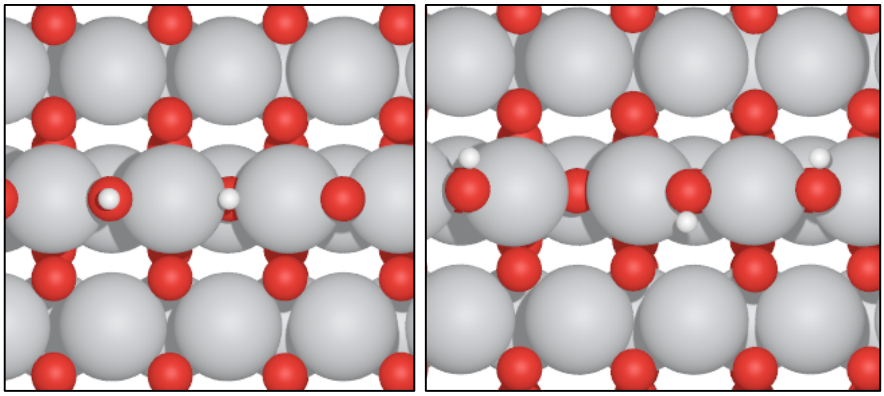

Figure 2.17. Two most preferred adsorption configurations of H_2 over the surface of rutile (110) with an oxygen defect. H-Ti_2, H-O_{br} configurations shown at the left, while H-O_{br}, H-O_{br} configuration is shown at the right. Only two hydrogen atoms were added but the image in the right show more due the periodicity of the slab.

The adsorption of hydrogen over the O-defected anatase surface is quite different. In this case, the most stable adsorption configuration of hydrogen involves the formation of H-Ti bonds (H-Ti_2, H-Ti configuration), forming hydride species. The adsorption energy in this case is 0.120 eV, similar to those most stable configurations obtained for the rutile surface. The second most preferred adsorption configuration (H-O_{3fold}, H-Ti_2) of hydrogen over reduced anatase has ΔE_{ads} = +0.50 eV, higher by 0.38 eV than the most stable hydride configuration. A mostly equally stable configuration involves the homolytic dissociation of H_2 forming two H-O_{br} bonds (H-O_{br}, H-O_{br} configuration). This last configuration has a ΔE_{ads} = 0.504 eV. Figure 2.18 displays the three most stable configurations for hydrogen adsorption over reduced anatase.

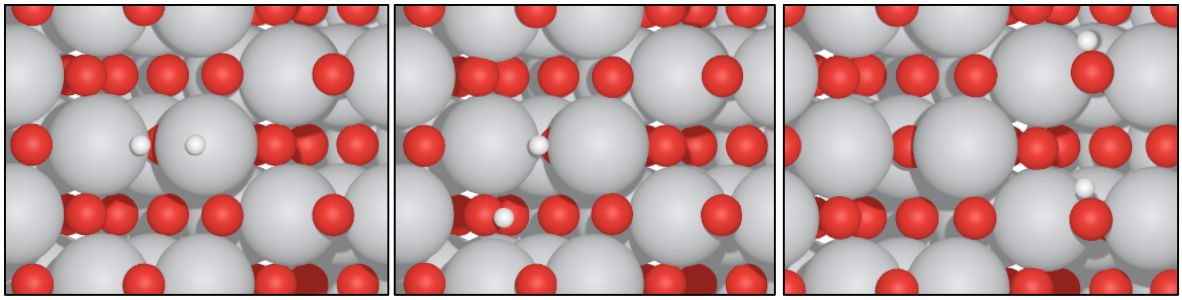

Figure 2.18. Three most preferred adsorption configurations of H_2 over the surface of anatase (101) with an oxygen defect. H-Ti_2, H-Ti configuration shown at the left, H-O_{3fold}, H-Ti_2 configuration is shown in the middle and H-O_{br}, H-O_{br} configuration is shown at the right.

To further investigate the formation of the hydride over reduced anatase, we determine the EDD of the system containing two adsorbed hydrogen atoms over Ti sites. The EDD was determined as the difference in the electron density of the H-Ti_2, H-Ti configuration and the sum of the electron densities of the O_{vac}-slab and isolated H atoms. A visualization of the EDD obtained is displayed in Figure 2.19. As can be seen in this figure, upon hydrogen adsorption over Ti sites, electrons were transferred from the Ti atoms, initially the oxygen vacancy neighbors, to the adsorbed H atoms. This suggests that the extra electrons, initially left by the oxygen atom while forming a vacancy, allocates on the hydrogen atoms while forming the H-Ti bonds, reversing reduction.

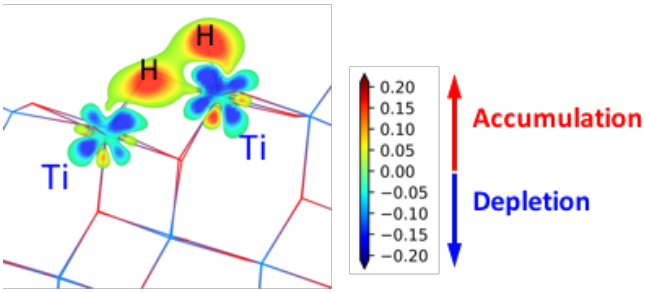

Figure 2.19. Electron density difference of the adsorption of hydrogen over Ti sites over the surface of O-defected anatase (101). Side view oriented in the [010] direction of the slab.

From these results, we may speculate that the reduction process of rutile-TiO_2 is considerably different from that on anatase. For instance, a facile accommodation of the extra electrons due to hydrogen adsorption might occur over rutile, even at the proximity of an existent oxygen vacancy.

However, over anatase the allocation of extra electrons might be a more difficult process once the surface has been reduced, leading to a more stable hydride state reversing reduction.

2.4. Discussion

A recent assessment by Hadjiivanov[100] on the interpretation of the surface hydroxyl bands of anatase and rutile titania indicates that assignments continue to be based on early coordination models of bridging vs. terminal hydroxyls. Dzwigaj, et al.[48] compared water and hydroxyl bands with the DFT calculations for well defined anatase faces, by Aurrovel et al.;[42] however, bands that are typical of anatase titania (see Table 2.1) were identified as molecular water. Recent theoretical studies[73-74] show that the original categorization of the high frequency bands to terminal hydroxyls and low frequency bands to the bridging hydroxyls does not necessarily hold. For example, Liu et al.[73] using DFT calculations reported that on the anatase (101) surface, bridging hydroxyls vibrate at 3727 cm^{-1} (similar to our hydroxyl #5 in Fig. 2.10.-b, 3734 cm^{-1}), while the frequency of a terminal hydroxyl on the coordinatively unsaturated Ti_V site was 3627 cm^{-1}. As a result, fundamental studies are required for the rational interpretation of the surface hydroxyl bands. Although there are many studies on the thermodynamics and structure of TiO_2 surfaces,[43, 59, 76, 119-120], reported vibrational frequencies are rare and a number of experimental and theoretical inconsistencies remain in the assignment of surface hydroxyls.

One significant advance toward rational interpretation of the surface hydroxyl bands of anatase nanopowders was done by Arrouvel *et al.*[42] who did extensive calculations of the surface energies, vibrational frequencies, and phase diagrams (the relative surface energy of the hydrated surfaces and the oxygen-terminated surface as a function of temperature and partial pressure of water). As illustrated in Figure 2.20, Arrouvel *et al.*[42] calculated the frequency of water molecules coordinated to surface Lewis acid sites (top row),which overlap with terminal surface hydroxyls (second row).[42] Dzwigaj, et al.[48] compared their theoretical predictions with FTIR data in the presence of water vapor. As Deiana, et al.[47] noted, the isolated hydroxyl frequency predictions of Arrouvel *et al.*[42] could not be confirmed because

adsorbed water was present under the Dzwigaj experimental conditions and most hydroxyl stretching bands were assigned to adsorbed water. Although Deiana, et al.[47] pretreated P25 up to 600 °C under vacuum conditions of 10^{-5} mbar, upon cooling to room temperature residual water readsorbed, clearly evident from the presence of the water bending mode, precluding measurement of the isolated surface hydroxyls. Their widely cited work has continued to base isolated hydroxyl frequencies on the original assumptions by Primet, et al. [71] and Tsyganenko.[72] To make sure that surface hydroxyl bands were not measured in the presence of adsorbed molecular water over the course of several hours at room temperature, it was necessary to achieve water partial pressures comparable to UHV or maintain the surface at temperatures of 300 °C. In this work, we measured spectra in vigorously dry conditions at 300 °C to observed hydroxyls in the absence of water.

We based our assignments of surface hydroxyl frequencies to specific facets on satisfying four criteria: 1) likelihood that the facet exists; 2) evidence that there is a route to formation of the type of hydroxyls considered; 3) theoretical evidence supporting the thermal stability of the hydroxyl; and 4) the need to scale DFT frequencies to improve accuracy.

First, surface facets should exist. The prevalence of a facet in nanoparticles is controlled by its surface energy. The Wulff construction is a way to predict the particle morphology. Since P90 is composed of both rutile and anatase, we must consider facets of both phases; however the correspondence between the hydroxyl spectra of pure rutile, pure anatase, and P90 allows us to assign the bands labelled A1, A2, and A3 in the bottom of Figure 2.20 to the majority anatase phase, while the bands labelled R1 and R2 are predominantly associated with rutile. For rutile, the Wulff construction predicts that (110) planes are most abundant, but (101), (011), (100), and (001) facets would be present at equilibrium.[121] The bridging hydroxyls on the (110) surface are well known, as it is the most extensively studied single crystal oxide surface. In the Wulff construction of anatase TiO_2, only the (101) and (001) facets appear; however, the presence of other surface facets cannot be excluded. Calculated surface energies of the anatase (100) and (110) facets by Arrouvel et al.[42] shows that these facets have comparable surface

energies with the (001) surface facet. For example, the energy of the anatase (110) surface is only 40 mJ/m^2 higher than anatase (001). In addition, while Wulff constructions are usually calculated based on the surface energies of the stoichiometric surfaces, hydroxylation of the surface generally lowers surface energies making other facets energetically more likely during hydrothermal synthesis. Arrouvel et al.[42] showed that some surfaces that are relatively high energy become comparable when hydroxylated. In addition to the (101) and (001) facets, Mino et al.[40] also identified the (100) and (112) facets in pure anatase and anatase particles of pyrogenic TiO_2 by using DFT calculations to assign the FTIR bands of adsorbed CO. Yuan et al. using scanning transmission electron microscopy showed the presence of less common anatase surfaces such as (103), (102), and (301) facets in anatase nanocrystals.[122] Therefore, the presence of other facet in practical conditions cannot be excluded and a complete assignment will require calculations of hydroxyl frequencies on additional facets.

After surface facets are identified, we need to know what type of hydroxyls each facet can have. In general, there are three ways by which surface hydroxyls can form: (1) dissociative adsorption of water on the stoichiometric surfaces; (2) dissociative adsorption of water on defects such as oxygen vacancies; and (3) hydrogenation of the stoichiometric surfaces. The energetics of water adsorption on the stoichiometric TiO_2 surfaces is widely studied.[76, 123] Arrouvel et al.[42] covered the hydroxyls that are formed by dissociative adsorption of water on the stoichiometric anatase surfaces. Although the defect-free anatase (101) surface does not dissociate water, theoretical calculations of Selloni et al.[77-78] shows that dissociative adsorption of water on the oxygen vacancies of (101) surface is favorable.[77-78] Very recently, Nadeem *et al.* experimentally confirmed water dissociation on the oxygen vacancies of the anatase (101) surface by observation of the bridging hydroxyls in the STM images of single crystals.[79] Bridging hydroxyls could also form by hydrogenation of the stoichiometric surfaces if there is a route for hydrogen activation. Therefore, the final state of water dissociation on a surface with oxygen vacancies and final state of the hydrogenation of a defect free surface are identical in reducible metal oxides.[124]

Assignment of the hydroxyls remaining after calcination at 300 °C imposes a thermal stability constraint. Arrouvel et al.,[42] calculated phase diagrams involving molecularly adsorbed water on anatase (100) and (101) which have low thermal stability. We show the frequency range of these bands as open boxes in Figure 2.20 to convey their low thermodynamic stability. Based on the calculated phase diagrams and the absence of water bending modes in our spectra, we can eliminate these molecular water adsorption structures. For dissociative adsorption of water to form terminal hydroxyls, the phase diagrams indicate that hydroxyls on the anatase (001) and (110) surfaces satisfy the stability constraint (solid boxes) while those on the (100) do not (open box). We extended Arrouvel's work by calculating the phase diagrams for the bridging hydroxyls formed on the anatase (101) and (001) surface. Our phase diagrams in Figure 2.17 suggest that the bridging hydroxyls on the anatase (101) surface and terminal hydroxyls on the anatase (001) surface can remain hydroxylated at 300 °C at water partial pressures as low as $P_{H_2O} = 10^{-4}\ atm$. These are shown as solid boxes in the third row of Figure 2.20.

Dzwigaj et al. [48] assigned a band at 3670 cm^{-1} to the molecular water mode on (101), which is the only potential assignment for the band we observe at 3670 cm^{-1} (designated A2). This is inconsistent because there is no water bending mode in our spectra, their phase diagram[42] would predict desorption of molecular water at lower temperatures, and generally DFT frequencies are overestimated. They also assign the band at 3735 cm^{-1} to the terminal hydroxyls on (001). However, this band is not commonly observed for pyrogenic TiO_2[100]. Busca et al. observed a band at 3735 cm^{-1} of some of the anatase samples and assigned it to Si-OH hydroxyls[102]. Consistent with the latter assignment, we observed a low intensity band at 3740 cm^{-1} when silica is detected by XPS. Therefore, we assigned the 3740 cm^{-1} band to Si-OH hydroxyls.

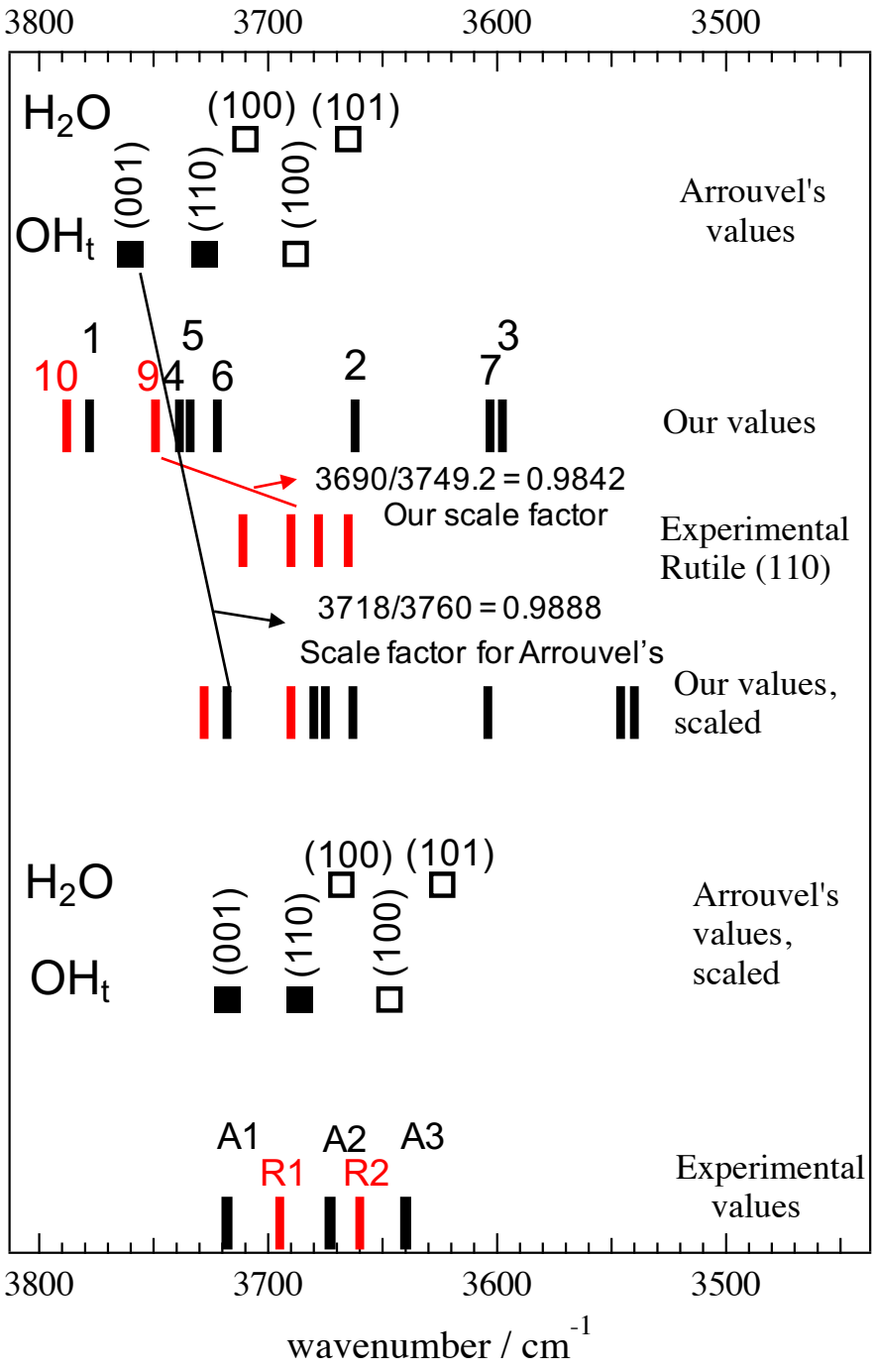

Figure 2.20. Assignment of the surface hydroxyls bands using the calculated vibrational frequencies calculated by Arrouvel et al. and us. Arrouvel's values are shown by squares and our values are shown by lines. Black symbols show anatase bands and red symbols shows rutile bands. The filled symbols show the species that can exist on the surface at 300 °C and empty symbols show the species that will desorb from the surface at temperatures below 300 °C, based on the calculated phase diagrams.

In calculations of molecular vibrational frequencies with DFT methods, scale factors ranging typically from 0.90 to 0.98 are used to obtain good spectroscopic accuracy. [125] Scale factors are well established for specific combinations of hybrid functionals and basis sets, [125-128] but no scale factor has been established for the plane wave basis sets and the RPBE or other non-hybrid functionals used in VASP, although there is a general expectation that frequencies are overestimated in plane wave DFT calculations.[129] An approximate value for the scale factor can be estimated from comparison of experimental and our calculated frequency for rutile (110). The vibrational frequency of bridging hydroxyls on the rutile (110) single crystal surface has been reported by several authors. Henderson used high resolution electron energy loss spectroscopy (HREELS) to measure a $\upsilon\ (O-H)$ value of 3665 cm^{-1} in one report[81] and 3690 cm^{-1} in another report[80] for the bridging hydroxyl formed by water dissociation on O-vacancy sites.[82] Yin *et al.*[57] used HREELS to obtain a $\upsilon\ (O-H)$ value of 0.456 eV (*i.e.*, 3678 cm^{-1}) for the bridging hydroxyl formed upon exposure of rutile (110) single crystals to atomic hydrogen.[124, 130] Petrik *et al.*[55] reported the value of 3711 cm^{-1} using infrared reflection-absorption spectroscopy (IRAS) for the hydroxyls formed by water dissociation on this surface. The average of the experimentally reported $\upsilon\ (O-H)$ values of the bridging hydroxyls of rutile (110) surface is 3686 ± 19.5 cm^{-1}. In comparison, the calculated value of OH_{br} on the rutile (110) surface is 3749.2 cm^{-1} (Table 2.2), indicating a correction factor of 0.983 ± 0.01, which is within the range expected.

Scaling our DFT frequencies by this factor brings the anatase (001) terminal hydroxyl frequency into alignment with peak A1 and the bridging hydroxyls on (101) into agreement with peak A2. This assignment satisfies the stability constraint and the facets are known to exist on P25. A more precise scale factor can be estimated from the best fit of our frequencies (1, 9, 4, 5,6,) to A1, R1, and A2. The frequencies of Arrouvel et al.[42] included anharmonic corrections, the scale factor to correct their frequencies should be closer to unity. By comparison of the terminal hydroxyls on (001) frequencies in both calculations, we estimate a scale factor of (0.988). This aligns their (001) terminal hydroxyl with our

A1 peak at 3717 cm^{-1}, as shown in row 7 of Figure 2.20, which is thermally consistent and resolves the suggestion that the 3735 cm^{-1} peak of Dzwigaj et al. [48] and our spectra be assigned instead to Si-OH impurities.

The scaled (110) terminal hydroxyl frequency of Arrouvel et al.[42] could be present in low coverage, but is certainly not resolved in our spectra. The only hydroxyl close in frequency to our anatase A3 peak is the terminal hydroxyl on the (100) face. These facets have been shown to exist,[40, 122] but the phase diagram[42] predicts desorption at lower temperatures. However, because the barrier to associative desorption could be sufficiently large to make it kinetically metastable (similar to the situation for the bridging hydroxyls on (101)), we cannot exclude it. Certainly, other facets, such as the (112) and (103), need to be explored as potential assignments. Nevertheless, bands R2 and A3 could not be assigned definitively from the facets considered in this work.

Further support for assignment of hydroxyls A1 to terminal OH on (001) and A2 to bridging hydroxyls on (101) can be gained from the H_2 dissociation experiments in Figures 2.6 and 2.7 where the intensity of A2 grows along with the broad electronic absorbance. Previous DFT studies of the energetics of H_2 dissociation on stoichiometric anatase and rutile surfaces [124] and this work on the energetics of H_2 dissociation on the O-vacancies of anatase (101) and rutile (110) surfaces shows that H_2 dissociation can be either homolytic or heterolytic. While homolytic dissociation of H_2 does not involve electron transfer to/from TiO_2, there are two electrons transferred to TiO_2 upon homolytic dissociation of H_2. Observation of a broad electronic absorbance in the difference DRIFTS spectra recorded during the reaction of H_2 with the anatase and rutile samples (sulfate paper) shows that electrons are transferred to the lowest unoccupied electronic states of TiO_2, which is in support of homolytic dissociation of H_2. This could be because although heterolytic dissociation is more favorable in some cases, there might be less barrier for homolytic dissociation. After homolytic dissociation of hydrogen, bridging hydroxyls are formed, see Figure 2.17 and 2.18 for rutile (110) and anatase (101) respectively. Formation of terminal hydroxyl on the TiO_2 surfaces studied upon reaction with H_2 would require breaking of a Ti-O bond which seems

unlikely. Hence, only bridging hydroxyls are formed after the reaction with H_2. In support of the later statement, we did not observe formation of band A1, which corresponds to terminal hydroxyls, after reaction of anatase and pyrogenic TiO_2 with H_2.

We now consider two aspects that limit the uniqueness of our assignments for the use of the isolated hydroxyl frequencies for identifying the exposed facets on titania nanoparticles. It should be noted that we have not considered all the possible surface facets in our assignment. For example, Mino *et al*[40]. using DFT calculations showed that anatase (103) has a comparable energy with anatase (001) surface, while the energy of anatase (112) is lower than anatase (001) surface. They also suggested that anatase (112) surface is present in the anatase particles of pyrogenic TiO_2 using FTIR of adsorbed CO. In order to assign the R1 and A3 bands, and also to be confident about the uniqueness of our assignments, the vibrational frequency of the hydroxyls on other anatase and rutile surface facets should be considered.

In addition, the frequency of the surface hydroxyls shifts depending on the coverage and temperature at which spectra were recorded. We observed that some of the surface hydroxyl bands shifted by 5-10 cm^{-1} as the temperature was reduced to 30 °C. Such thermal shifts of the isolated hydroxyl bands was previously reported for the surface hydroxyls of zeolites[100, 131-133]. Several reasons, such as thermal expansion of the lattice and anharmonic effects, are proposed for the thermal shift of the vibrational bands.[134-136] However, the present results, as well as data in the literature,[100, 131] show that the degree of thermal shift of surface hydroxyl bands varies among different hydroxyls on the same sample. Osuga *et al.* [131]associated the thermal shift of the surface hydroxyls of zeolites to thermal dissociation of Brønsted acidic hydroxyls and used the degree of the shifts to calculate the ΔH of O-H dissociation.[131] The range of thermal and coverage dependent shifts determined from experiment and theory should be considered in the assignments to provide qualitative understanding of the extent to which different facets can be distinguished from each other.

2.5. Conclusion

In this work, surface hydroxyls of pyrogenic, anatase, and rutile TiO_2 samples were characterized using DRIFTS and assigned using DFT calculations. Step-wise calcination performed under dry O_2 stream revealed the surface impurities common to the TiO_2 surfaces and temperature at which these impurities are eliminated. For the pyrogenic TiO_2, we observed four bands at 3641, 3673, 3687, and 3718 cm^{-1}. The observed bands were superimposition of the observed bands for the pure anatase and rutile, consistent with 95% anatase content of P90. We calculated the vibrational frequency of the surface hydroxyls formed on the anatase (001), anatase (101), and rutile (110) surfaces using DFT and based on the DFT-calculated values we propose that the 3718 cm^{-1} band is assigned to the terminal hydroxyls on the anatase (001) surface, the 3687 cm^{-1} band is assigned to the bridging hydroxyls of the rutile (110) surface, and the 3673 cm^{-1} band is assigned to the bridging hydroxyls of the anatase (101) facet.

CHAPTER 3

DOES THE CRYSTAL STRUCTURE OF TITANIA IMPACT THE EFFECTIVENESS OF RU/TIO$_2$ DIRECT DEOXYGENATION CATALYSTS?

We investigated whether the catalytic effectiveness of nanoparticulate ruthenium supported on titanium dioxide (Ru/TiO_2) depends on the structure of TiO_2. Ru supported on rutile TiO_2 is an excellent catalyst for the deoxygenation of phenol to benzene with high selectivity and good yields. In contrast, Ru supported on anatase TiO_2 is dramatically affected by surface sulfate poisoning. The widely used pyrogenic TiO_2 supports, P25 and P90, both show activity that is closer to the that of rutile than anatase, despite being 85 – 90 wt% anatase. This work presents a unique characterization of Ru/TiO_2 catalysts, points to the critical role that surface contaminants in commercially available anatase can play in catalyst poisoning, and affirms that the surface acid/base properties of titania, along with its interaction with water, are critical to the success of HDO catalysts. Heteroepitaxy between rutile RuO_2 and rutile TiO_2 is not essential for the creation of active Ru/TiO_2 DDO catalysts.

3.1. Introduction

We recently proposed a mechanism by which Ru on TiO_2 directly deoxygenates phenol with high efficiency and selectivity for benzene.[137] The proposed mechanism relies on the presence of a surface hydroxyl at the TiO_2-Ru nanoparticle interface, which acts as a Brønsted base and facilitates the heterolytic cleavage of Ru-associated H_2. In a subsequent step, the now protonated surface hydroxyl functions as a Brønsted acid and protonates and anchors the phenolic oxygen, which weakens the C-O bond. Additional water in the reaction suppresses vacancy formation on the TiO_2 surface and speeds up the loss of water from the substrate. The mechanistic role of the titania crystal structure was not considered in the initial report. These prior experimental results were obtained using Ru/TiO_2 P25 (a widely used form of pyrogenic titania that is a mix of anatase and rutile phases), while the titania surface was computationally modeled as being in the rutile phase. In this work, we have expanded our survey to

include other forms of TiO_2 to address the question of whether the crystal phase of titania affects reactivity. In addition to repeating our work with P25, experiments were done using P90 (a higher surface area analog of P25 containing both anatase and rutile phases and a small amount of an uncommon form of titania, TiO_2B[138]), and pure rutile- and anatase-phase titanias from several different sources. Our catalytic results show clear differences between different titania supports. Below we describe our use of HRTEM, PDF, and DRITFS spectroscopy to characterize the catalysts and to provide evidence that disproves the hypothesis that heteroepitaxy between RuO_2 and rutile TiO_2 is essential for the formation of highly selective Ru/TiO_2 catalysts.

3.2. Experimental section

A number of materials characterization techniques were utilized at UMaine for characterization of supports and catalysts. The methods are described below.

3.2.1. XPS

TiO_2 samples were placed on carbon tape for XPS analysis. Samples were outgassed at room temperature and pressures < 10^{-8} torr for 3h before the analyses. XPS analyses were performed using a SPECS PHOEBUS 100 MCD plus analyzer at a pass energy of 100 eV with an Al Kα X-ray source working at 240 W and 20 mA.

3.2.2. Inductively coupled plasma-optical emission spectroscopy (ICP-OES)

ICP-OES analyses were performed using an iCUP 6000 ICP-OES ThermoFisher instrument. 0.1 gram of the TiO_2 samples was digested in 2 mL HCl, 2 mL HNO_3, and 5 mL HF solution at room temperature in Teflon vials until dissolved. HF was neutralized with a saturated solution of boric acid before analysis. Intensities were converted to sulfur content from experimental calibration curves and reported as ppm on a mass basis (mg S/kg sample).

3.2.3. N_2 adsorption porosimetry

Nitrogen sorption isotherms were determined at 77 K using a Micromeritics ASAP-2020 instrument. Before the analyses, samples were degassed by evacuation at 350 °C. Surface area was determined using the BET method.[139]

3.2.4. DRIFTS

DRIFT spectra were recorded using a Nicolet 6700 Fourier Transform Infrared (FTIR) spectrometer equipped with a Praying Mantis™ (Harrick Scientific Production, IBC) accessory. KBr powder was placed in the sample cup inside a Harrick Scientific high temperature reaction chamber (HVC). The sample cup in HVC was placed on a temperature-controlled sample stage equipped with a cartridge heater and a thermocouple. The sample cup temperature was controlled by a Harrick Scientific Automatic Temperature controller (ATC-024-1).

The TiO_2 samples were spread on top of the KBr powder in the sample cup for DRIFTS studies. After the material was loaded in the chamber, the environmental chamber was heated externally overnight with the sample maintained at 70 °C under an O_2 flow (Grade 2, Matheson). The O_2 was dried with a molecular sieve (13X, 4 to 8 mesh, Acros Organic) trap immersed in a dry ice-acetone bath. Step-wise temperature-programmed calcination was performed in the environmental chamber while several DRIFTS spectra were recorded at each temperature. All the DRIFTS spectra were recorded under dry O_2 flow by accumulation of 512 scans at 8 cm^{-1} resolution using a DTGS detector.

3.3. Results

Here, we present detailed physico-chemical characterization of the TiO_2 supports in order to make structure-activity relationship for the DDO of phenol using Ru/TiO_2 catalysts.

3.3.1. XPS, ICP-OES, and BET

XPS and ICP-OES spectroscopy were used to determine the chemical impurities in the TiO_2 samples. Survey XPS scans of the TiO_2 samples (SI) revealed C1s, Ti2p, and O1s peaks for all the samples. The C1s peak was observed because samples were placed on a carbon tape for the XPS analysis. The S2p peak at 168.5 eV was the first clear evidence for the presence of a potential catalyst poison, and it was observed in the XPS spectra of Sigma Aldrich (SA), U.S. Research (USR), and Alfa Aesar (AA) anatase samples (Figure 3.1). Consistent with the XPS results, ICP-OES analyses of SA, USR, and AA anatase samples showed the presence of sulfur impurities, as summarized in Table 3.1. Pure anatase is commercially produced via the "sulfate method" while pyrogenic TiO_2 is produced from gas phase hydrolysis of $TiCl_4$.[140] Hence, the presence of sulfate impurities in most of the commercial anatase samples is easy to explain. There is also a Si 2s peak visible at 154 eV[141] in the XPS spectra of P90, rutile, AA, and USR anatase samples (Figure 3.1).

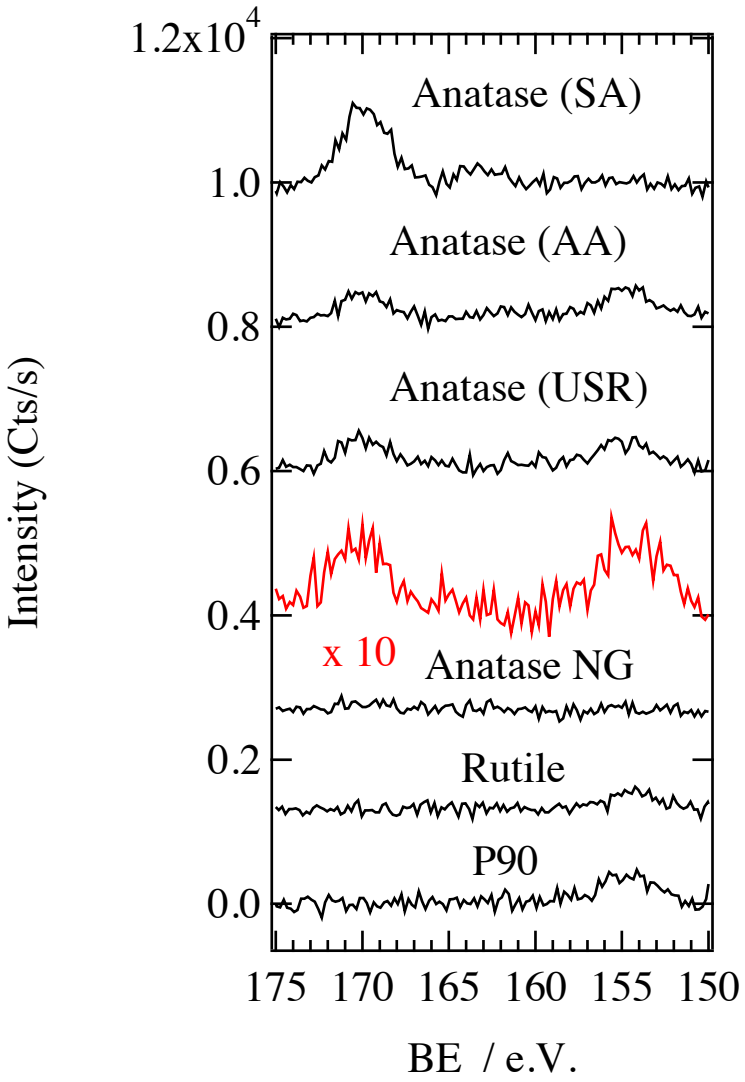

Figure 3.1. XPS spectra of the as-received TiO_2 samples, as indicated, in the sulfur 2p and Si 2s region. Spectra offset for clarity. Red curve shows a spectrum for Anatase NG in which the counting time was increased by a factor of 10 and expanded by 10x to confirm the presence of sulfur and silicon impurities.

Survey spectra showed that Ti, O, and C were present on all samples. The commercial anatase samples also showed sulfur. Rutile, P90, and Anatase (SA) also showed silicon. The thickness of a carbonaceous layer, d_c, was estimated from the C 1s/Ti 2p peak area ratios using a 2-layer model,

$$\frac{I_{C1s}}{I_{Ti2p}} = \frac{N_c \sigma_{C1s} \lambda^C_{C1s} [1 - exp(-d_C/\lambda^C_{C1s})] T(KE_{C1s})}{N_{Ti} \sigma_{T2p} \lambda^{TiO2}_{Ti2p} \, exp(-d_C/\lambda^C_{Ti2p}) T(KE_{Ti2p})}$$

where effective attenuation lengths (EAL), λ_m^M, for core level *m* in material *M,* were calculated using the NIST electron effective attenuation length database, Ver. 1.3, for TiO_2 anatase (density 3.893 g/cm^3, band gap 3.2 eV) and polymer $(CH_2)_x$ (density 0.99 g/cm^3, band gap 4.5 eV as model for carbonaceous carbon, following Seah and Spencer[142]) at the kinetic energies of the respective photoemission lines. We used beta asymmetry parameters from Reilman et al.[143] and Scofield's[144] photoionization cross sections. The analyzer transmission function, $T(KE)$, for an electron with kinetic energy, *KE*, was determined by SPECS by comparison of Au and Ag foil spectra to those measured for a known transmission function.[145] The total cross sections, σt_m,

$$\sigma t_m = \sigma_m \left(1 - \frac{\beta_m}{2} P_2(cos\theta)\right)$$

where, σ_m is the photoionization cross section, β_m is the beta asymmetry parameter of the corresponding core level, and P_2 is the Legendre Polynomial for an angle between the incident photon and emitted photoelectron, $\theta = 45°$. The Legendre polynomial, P_2, is given by:

$P_2(x) = \frac{3x^2-1}{2}$. The number density (atoms/cm^3), N, is

$$N = \frac{\rho N_A}{M_W}.$$

where M_W is the molar mass, ρ is the density of the material, and $N_{\square}$ is Avogadro's number. Peak areas were determined from numerical integration after subtraction of a Shirley baseline, excluding the x-ray satellite peaks. For anatase, the Ti number density in TiO_2 was calculated to be 2.935 x 10^{22} atoms/cm^3 based on the crystal structure[146] and for the carbonaceous "polymer" layer 1.14x10^{23} atoms/cm^3. The O:Ti stoichiometry, N_O/N_{Ti} was calculated from

$$\frac{I_{O1s}}{I_{Ti2p}} = \frac{N_O \sigma_{O1s} \lambda_{O1s}^{TiO2} \left[1 - exp\left(-d_C/\lambda_{O1s}^{C}\right)\right] T(KE_{O1s})}{N_{Ti} \sigma_{T2p} \lambda_{Ti2p}^{TiO2}\, exp\left(-d_C/\lambda_{Ti2p}^{C}\right) T(KE_{Ti2p})}$$

and was within 10% of the expected 2:1 ratio. The carbonaceous layer thickness ranged from 7-12 Ångstroms depending on the sample.

The sulfur 2p region of the XPS spectra of the samples are shown in Figure 3.1. Using the ratio of the S 2p and Ti 2p peak areas, we estimated the surface sulfate coverage on the TiO_2 surface, $\theta_S(\frac{atoms}{area})$, assuming sulfur was adsorbed only on the nanoparticle surface and that both core level peaks were attenuated by the carbonaceous layer.

$$\theta_S = \frac{I_{S2p}}{I_{Ti2p}} \frac{N_{Ti}\sigma t_{Ti2p}\lambda_{Ti2p}^{TiO2}\, exp\left(-d_C/\lambda_{Ti2p}^{C}\right)T(KE_{Ti2p})}{\sigma t_{S2p} exp\left(-d_C/\lambda_{S2p}^{C}\right)}$$

The sulfur coverage is shown in Table 3.1. For comparison with the ICP-OES bulk composition, the mass of sulfur on a spherical particle, whose diameter was chosen to give the BET surface area shown in Table 3.1, was calculated from the estimated coverage from XPS and the particle area. The bulk composition was then calculated from the ratio of the mass of sulfur to the mass of the spherical TiO_2 nanoparticle, expressed in ppm on a mass basis. The values agreed better with the ICP-OES measurements than with the higher sulfur content estimated from XPS assuming the sulfur was homogeneously distributed through the nanoparticle. For particle diameters of order 10 - 30 nm, the average sulfur content based on a homogenous particle model was only larger by a factor of 2; e.g. the Anatase (SA) would have sulfur content of 8200 ppm if the XPS intensities were analyzed based on homogeneous particle composition.

To reduce/remove the sulfur content of the commercial anatase samples, they were subjected to a calcination/reduction/calcination cycle, with each step conducted at 400°C, for 5 h. The sulfur levels were below detection limits in XPS (Figure 3.2). ICP-OES analyses of the pretreated samples did not show the presence of sulfate species.

Table 3.1. Chemical and physical characterization of TiO_2 samples

Material		ICP-OES S content / ppm	XPS S Content S atoms/ nm^2	BET surface area m^2/g	Estimated bulk S content/ppm[d]
Pyrogenic	P90	<500	ND[a]	100	NA
Anatase	SA	3660	1.5	50[c]	4000
	AA	1361	0.47	136	3300
	USR	782	0.52	93	2500
	NG	<500	0.15	280	870
	BC	NA[b]	ND	159	NA
Rutile	USR rutile	<500	ND	33	NA

[a] Not Detected, [b] Not Available, [c] as specified by the manufacturer, [d] milligrams of sulfur in a kilogram of titania

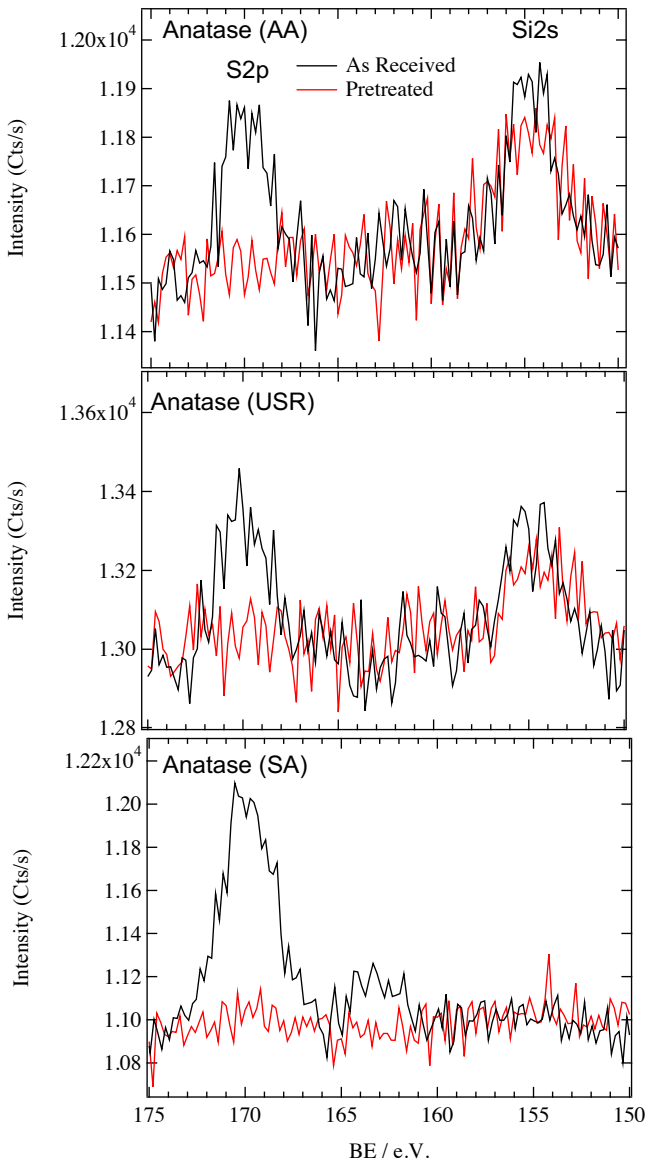

Figure 3.2. XPS analysis of commercial anatase samples before (black spectra) and after 400°C calcination-reduction-calcination pretreatment (red spectra)

3.3.2. X-ray diffraction

Crystal structures were identified from x-ray diffractograms measured using a PANalytical X-PertPro X-ray diffractometer utilizing Cu-Kα radiation in a parallel beam optical configuration. Powder samples were placed on a quartz zero-background plate for the XRD analysis. X-ray diffractograms (Fig.

3.3) of the BC, SA, USR, and AA anatase shows pure anatase phase, while P90 shows 95% anatase and 5% rutile content.

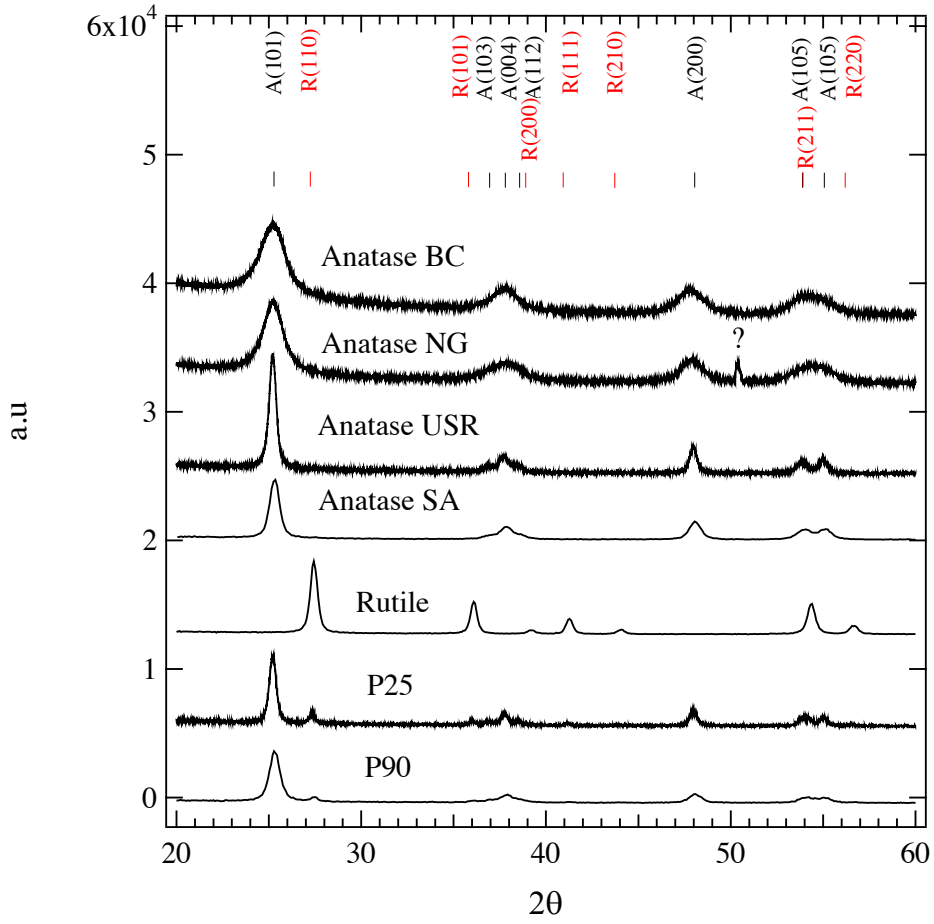

Figure 3.3. X-ray diffractograms of the TiO_2 samples.

3.3.3. DRIFTS

Surface hydroxyls feature prominently in our proposed reaction mechanism and serve as an important clue to catalytic activity in this work. DRIFTS spectroscopy provides a method for observing surface hydroxyls and detecting differences in these key surface moieties between different sources of titania. Of particular interest to this work was observing whether the surface sulfur, previously detected by other methods, interfered with these catalytically important surface moieties. The calcination of TiO_2

samples was monitored using DRIFTS to distinguish stretching frequencies of water from those of surface hydroxyls in an effort identify the differences between pyrogenic titania (i.e. P90 and P25) and pure anatase samples. DRIFT spectra of P90, and anatase TiO_2 samples, recorded during step-wise temperature-programmed calcination (TPC), are presented in Figure 3.4. Several bands are observed that are attributed to chemical species originating from the reaction of the surface with atmospheric gases, such as water and carbon dioxide, or from chemical impurities introduced during material synthesis, some of which can be removed by TPC. The 1357, 1444, and 1547 cm^{-1} bands are assigned to surface carbonates or bicarbonate.[147] The 1624 cm^{-1} band is assigned to the bending mode of water. The broad absorbance feature in the 2500-3600 cm^{-1} region contains the vibrational bands of water and H-bonded surface hydroxyls.[46, 47,] The bands in the 2800-3000 cm^{-1} region correspond to C-H stretching vibrations of hydrocarbon impurities. The complex absorbance features in the 3600-3800 cm^{-1} region are due to the vibrational modes of isolated hydroxyls.[42]

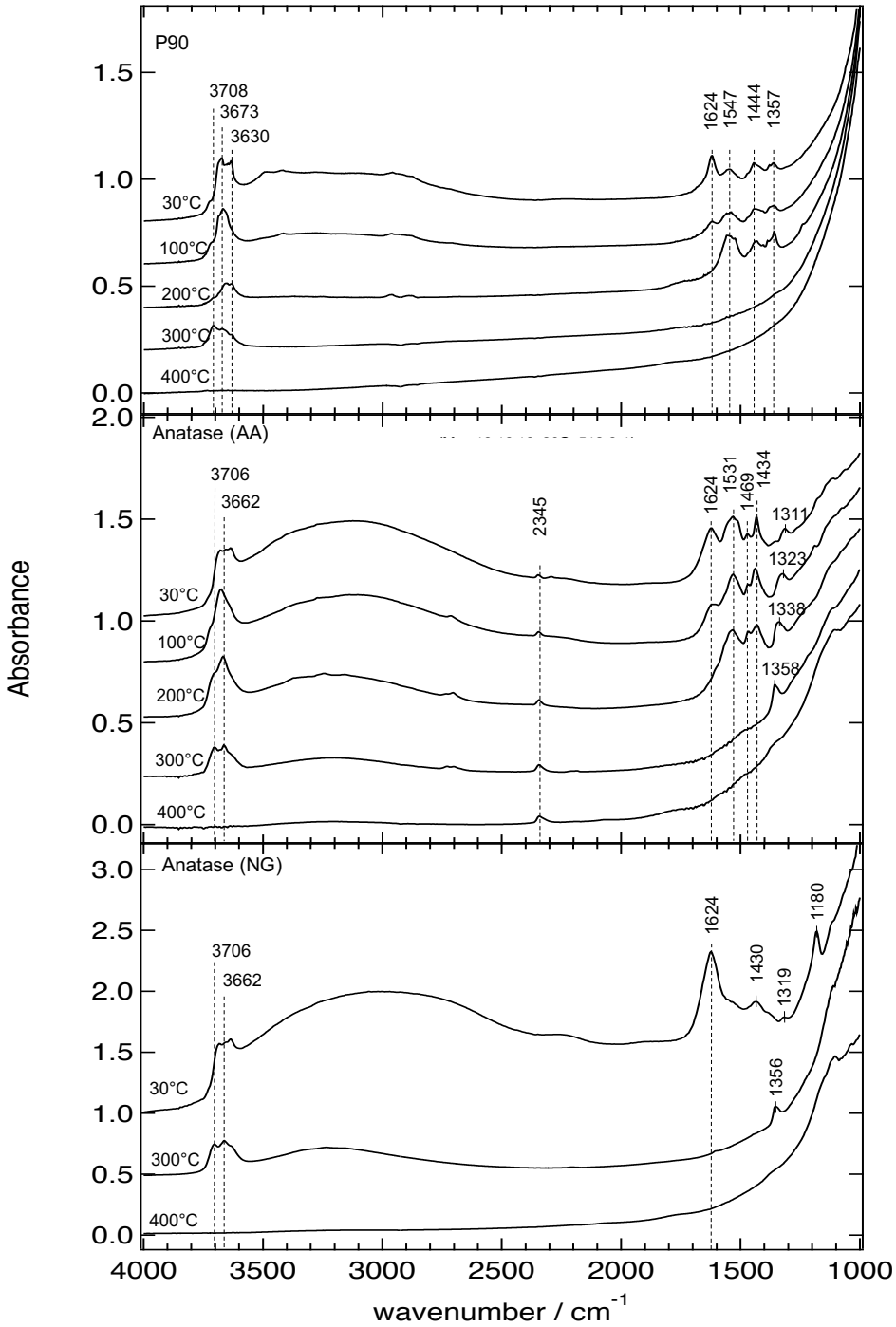

Figure 3.4. DRIFTS spectra of TiO_2 samples recorded during the calcination process from 30 °C to 400 °C. All the spectra are referenced to dried KBr powder on which sample was placed. Spectra offset for clarity.

DRIFTS spectra recorded during the TPC of P90 shows changes in the chemical state of the surface at each temperature. On the P90 surface, water was eliminated at 200 °C, carbonates or bicarbonates at 300 °C, and surface hydroxyls at 400 °C. After complete removal of the carbonate bands, three signature surface hydroxyl bands at 3629, 3673, and 3708 cm^{-1} were the major bands observed, very similar to the predominant bands of pure, sulfur-free anatase (Chapter 2). Rutile showed (Chapter 2) bands at 3652, 3683, and 3727 cm^{-1}. This comparison indicates that the exposed surface of P90 is mostly anatase, which is consistent with data from HRTEM and FTIR spectra of adsorbed CO on anatase.[148]

DRIFTS spectra of anatase samples confirm the presence of surface sulfates, consistent with XPS and ICP-OES data. DRIFTS also provides a sensitive measure of the effectiveness of different treatment methods designed to reduce the amount of sulfur on the surface, which can then be correlated with catalytic results. DRIFTS spectra of AA anatase recorded at 30 °C shows bands at 1311, 1434, 1469, and 1531 cm^{-1}. Heating can distinguish surface carbonates from surface sulfates, both of which have FTIR absorbance bands at 1311 cm^{-1}.[147,149] While the carbonate bands are eliminated upon heating (as was observed for P90), the sulfate band blue shifts to ~1360 cm^{-1} as a tridentate sulfate species is formed[149-150] (Scheme 1). In AA anatase, the band at ~1311 cm^{-1} gradually blue shifts to ~1358 cm^{-1} as the sample is calcined from 100 °C to 300 °C, indicating that sulfur is present on the surface. The IR signature of the surface sulfate was also observed for the USR, SA, and NG anatase samples (Figure 3.5-A). The tridentate sulfate band at ~1360 cm^{-1} was eliminated from the DRIFTS spectra of all commercial anatase samples after overnight calcination at 400 °C.

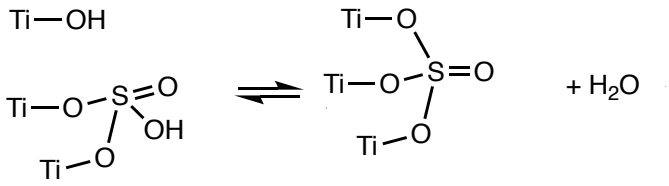

Scheme 3.1. Formation of tridentate sulfate band from dehydration of sulfated titania (Adapted from Saur et. al.[149])

It is particularly important to know the chemical state of the surface at 300 °C since this is the temperature at which the phenol HDO reactions are performed. Figure 3.5-A provides spectra that facilitate the comparison of several of the anatase samples with P90 after extensive calcination at 300 °C. The absence of the water bending band at ~1620 cm^{-1} in all the spectra indicates the TiO_2 surfaces are dehydrated. The ~1360 cm^{-1} band in all the commercial anatase samples (AA, SA, USR, and NG) shows the presence of tridentate sulfate species on the surface. The broad feature associated with H-bonded surface hydroxyls was observed for all low-temperature synthesized anatase samples, including the sulfur-free anatase(BC), which contrasts with the pyrogenic P90 spectrum.

Surface sulfur species perturb the surface hydroxyls (Figure 3.5-B). The 3708 cm^{-1} band of sulfate-free anatase and P90 samples red shifts by about 2 cm^{-1} while the 3673 cm^{-1} band red shifts by 11 cm^{-1} when sulfate is present. In addition to the frequency shift, the presence of surface sulfate changes the relative intensity of the bands in this region. While the 3708 cm^{-1} band is more intense than the 3673 cm^{-1} band in P90 and sulfate-free anatase, the relative intensity reverses in the sulfated anatase samples. As the amount of sulfate increases, the ratio of the higher-to-lower frequency band decreases.

We recently assigned the 3708 cm^{-1} band to the terminal hydroxyls (OH) of the anatase (001) surface and the 3673 cm^{-1} band to the bridging hydroxyls of anatase (101) surface (Chapter 2). A relative decrease in the terminal (001) OH peak intensity suggests that this facet is either covered with a greater amount of sulfate or that the facet is less prevalent in materials with greater sulfate content. An alternative explanation is that sulfur makes the surface more reducible (analogous to the effects of nitrogen[151]),

increasing the oxygen vacancy coverage and increasing the amount of surface hydroxyls formed from dissociative adsorption of water, thereby increasing the intensity of the 3708 cm^{-1} band relative to the 3673 cm^{-1} band.

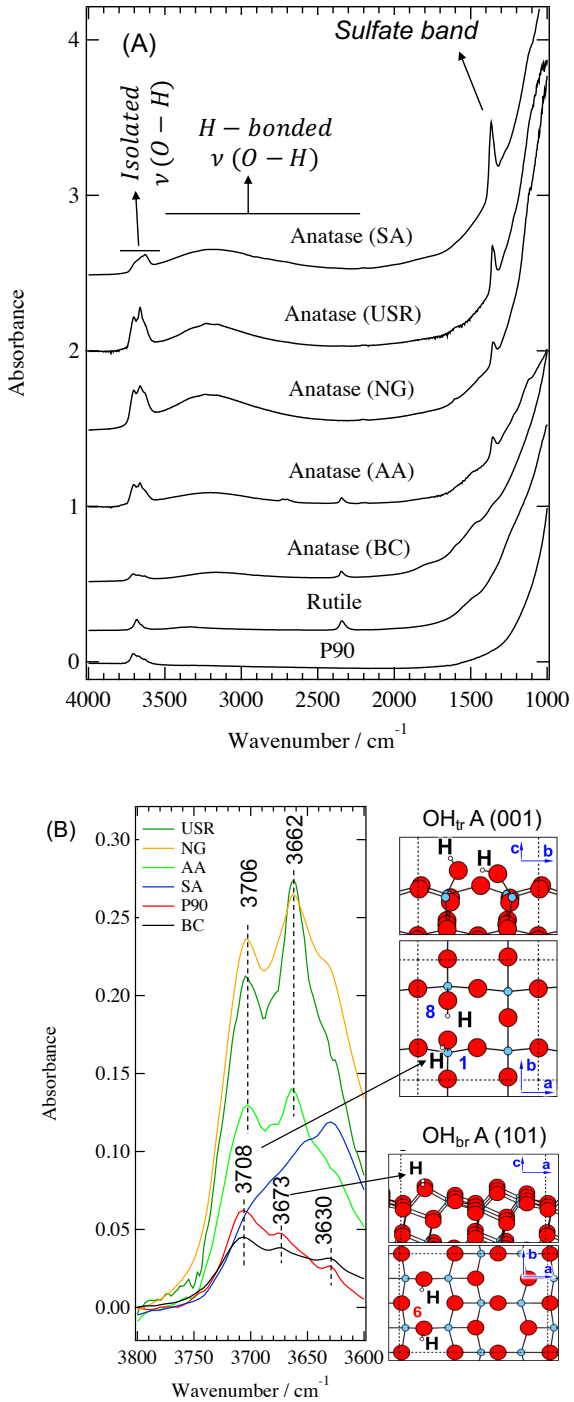

Figure 3.5. DRIFTS spectra of P90 and anatase samples recorded at 300°C in the entire spectrum (A) and in the isolated hydroxyls region (B). Spectra are off-set for clarity. See the supporting information for the description of the number codes.

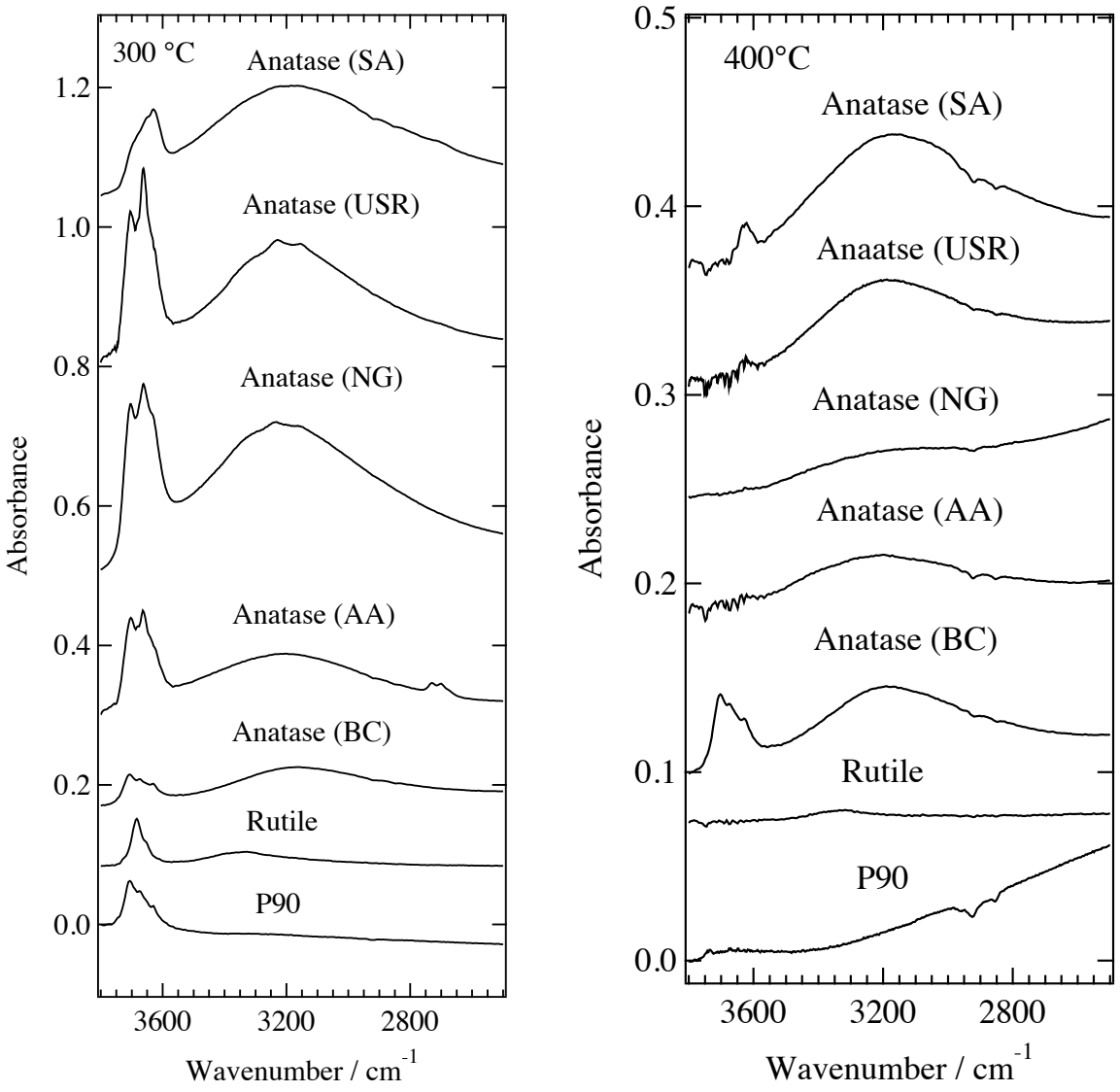

Figure 3.6. DRIFTS spectra of the P90 and anatase samples in the 2000-3800 cm^{-1} region after overnight calcination at (left) 300 °C and (right) 400°C. Spectra are off-set for clarity.

DRIFTS spectra of the TiO_2 samples after overnight calcination at 300 °C and 400 °C in the 2500-3800 cm^{-1} region are shown in Figure 3.6. In a contrast to the complete dehydroxylation of P90, the broad absorbance band in the 2500-3500 cm^{-1} region observed for all the anatase samples shows that the low temperature synthesized samples are still hydroxylated.[152] The extent of hydroxylation may produce differences in the hydrophilicity of the surface and affect the role of water, which is a co-catalyst in the

reaction. Note that the negative-going C-H modes in the 400 °C data are due to loss of hydrocarbons from the KBr, which was only calcined at 300 °C before measuring a single beam spectrum.

3.4. Discussion

In our earlier work, we demonstrated that small particles of metallic Ru are required for achieving high selectivity for DDO, suggesting the active site for direct deoxygenation exists at the interface between the particle and the support.[153] The preponderance of data from EXAFS[153] indicates that the catalytically active phase involves Ru, not RuO_2, which would be unlikely to exist under the catalytic reaction conditions employed. A study by Crossley *et al.* shows strong evidence that the rate of gas-phase DDO of cresol is proportional to the number of interfacial sites and specifically to the total perimeter length of the Ru TiO_2 interface, which is also consistent with the importance of this interface.[154-155]

This work demonstrates that it is more difficult to make a highly selective DDO catalyst using anatase as a support than rutile or pyrogenic titania; even the highest purity anatase does not produce selective DDO catalysts. Pyrogenic TiO_2 (both P25 and P90) can be used to make highly selective DDO catalysts, even though both P25 and P90 are both primarily anatase. These observations raise several questions regarding the material and its surface, which we articulate and address below.

Is there an effect associated with the epitaxial matching between rutile RuO_2(110) and rutile TiO_2(110) that either stabilizes the RuO_2 phase or facilitates high dispersion in the activated catalyst? RuO_2 has a rutile crystal structure with lattice parameters well matched to those of rutile TiO_2, which has spawned speculation that heteroepitaxy between RuO_2 and rutile TiO_2 facilitates catalytic selectivity.[156-160] The results from Crossley *et al* in which deoxygenation of *m*-cresol is insensitive to TiO_2 crystal structure[154], while their results with guaiacol are not, providing no clear-cut answer to the role of titania structure in DDO catalysts.[154]

Our results initially seemed consistent with the heteroepitaxy hypothesis as Ru/TiO_2 rutile was a much more active and much more selective catalyst than Ru/TiO_2 anatase. The high selectivity and activity of both Ru/P25 and Ru/P90, both of which are primarily anatase, raised questions, however, about this hypothesis. Our results would, however, be consistent with the heteroepitaxy hypothesis if P25 and P90 had a thin shell of rutile TiO_2 on top of a core of anatase TiO_2.

Is there evidence to support a core-shell model, originally suggested from microscopy, where there is a rutile layer less than 1 nm covering the surface of the anatase particles in P25 and P90? The morphology of P25 and P90 have been debated extensively. [161-162] The first detailed investigation of the morphology of P25 was performed by Bickley et al.[163] P25 was described as a mixture of an amorphous state with pure phase crystals present. The appearance of the Moiré fringes in the HRTEM data was interpreted as being consistent with the presence of some anatase particles being covered by a thin layer of rutile.[163] Later studies have, however, refuted the core-shell model. Datye[164] *et al*. used additional HTREM data to conclude that anatase and rutile exist as discrete crystalline particles, as did Ohno *et al*.[37] who argued that anatase and rutile exist as single phase particles with a small amount of amorphous material present. Datye *et al.*[164] did not conclusively detect any amorphous particles or core-shell particles, but left open the possibility that there could be an overlayer of rutile on anatase particles. Mino *et al.* argued that the presence of a rutile overlayer on anatase could escape observation by HRTEM and that new routes of P25 morphology assessment should be undertaken.[148] Accordingly, we have undertaken PDF and HRTEM measurements on P90 in this study, and these data confirm the presence of individual small rutile and anatase particles.[161] DRIFTS measurements of the surface hydroxyls, as described in greater detail in Chapter 2, show that the frequencies of surface hydroxyls of TiO_2 can be associated with the specific distribution of facets exposed on anatase and rutile. The dominant isolated hydroxyl frequencies on P90 and P25, assigned to terminal hydroxyls on the anatase (001) face and bridging hydroxyls on the anatase (101) face, are not consistent with the core-shell model. The band at 3687 cm^{-1}, assigned to the bridging hydroxyls on the low surface energy rutile(110) face, tracks

qualitatively with the rutile content of pyrogenic titania and is weak in the P90 DRIFT spectrum (containing 5% rutile) and somewhat stronger in the P25 DRIFT spectrum (containing 12% rutile).[165]

The lack of evidence for rutile on the anatase particle surfaces of P90,[165] and pyrogenic titania in general,[148, 166] argues against a core-shell model for pyrogenic titania. So if heteroepitaxial growth is important in Ru/TiO_2 catalysts, there would be small well-distribtued Ru(0) particle formation only on the (110) facets of the surface associated with the 5% of pyrogenic titania present as rutile particles.[159] TEM images of pretreated catalysts showed no evidence for preferential formation of Ru nanoparticles on the rutile vs. anatase components of P90. Alternatively, smaller Ru particles necessary for high DDO selectivity[137, 153] could be stabilized during catalyst synthesis by heteroepitaxial growth of rutile RuO_2 on rutile(110) TiO_2 facets compared to other facets of rutile and anatase. No significant differences in nanoparticle size were observed in HRTEM between the anatase and rutile components of P90, nanoparticles on pure anatase, or those on pure rutile catalysts. Furthermore, Ru/P90 was synthesized anaerobically using RuC clusters as ruthenium precursors, and results from the catalyst so synthesized did not differ appreciably from Ru/P90 synthesized in air, a result again inconsistent with heteroepitaxy between rutile ruthenium oxide and rutile titanium oxide being a critical determinant in catalyst selectivity (SI).[167] Overall these results, along with published results on a similar catalytic system by Crossley[154], do not support the heteroepitaxy hypothesis.

Is the DDO of phenol on the Ru/TiO_2 surface a "structure sensitive" reaction, in which the selectivity can be associated with the amount of particular facets and the acid/base properties of the hydroxyls on these facets, and might these differ between anatase synthesized by different methods? The presence of sulfur contamination on most commercial phase-pure anatase materials interferes with the activity and selectivity of the catalysts for HDO of phenol. Our XPS measurements suggest that the coverage of sulfate on the anatase surfaces is relatively high, of the order of a monolayer. The presence of sulfate groups strongly attenuates the band at 3717 cm^{-1}, assigned to terminal hydroxyls on the anatase(001) face, and decreases the intensity of the 3673 cm^{-1} mode associated with bridging hydroxyls

on the anatase(101) face. Because the catalytic mechanism proposed requires hydroxyls that act as a Brønsted base for heterolytic dissociative adsorption of H_2 across the Ru/TiO_2 interface, the loss of hydroxyls could account for the decrease in the DDO selectivity, particularly if the anatase (101) bridging hydroxyls are critical as the active sites in the mechanism.[137] Although calcination-reduction-calcination of the sulfate-containing anatase materials significantly reduced the bulk and surface sulfate content, DRIFTS measurements after exposure H_2O show the re-appearance of sulfate-related bands, similarly to observations by Sauer, et al.[168] after exposure to to H_2.

The remaining question is why anatase synthesized using sulfur-free methods achieves conversion comparable to pyrogenic and rutile based catalysts, but does not have the same selectivity to the DDO product, benzene. We suggest several possibilities. First, if the reaction is structure sensitive, such that the hydroxyls on different facets have different acid-base properties,[169] and there is a different distribution of exposed facets in pyrogenic TiO_2 compared to low temperature synthesized anatase, then the selectivity to DDO could be influenced by the synthesis conditions. The facets that are thermodynamically stable, as predicted from the Wulff construction, have been assessed by Arrouvel *et al.*[42], and in our work[165], from calculations of the surface energy of surfaces with varying coverages of molecularly or dissociatively adsorbed water. Experimental and theoretical evidence for other, low surface energy facets, such as the anatase (102) and (103) facets illustrates the potential of hydroxyls being on well defined, but as yet unidentified, exposed surfaces of crystalline anatase.[122, 170] Although not necessarily the thermodynamically stable morphology, kinetic constraints during synthesis using structure directing agents[171] can potentially produce facet distributions that differ from the amounts expected from the Wulff construction. Although the acid/base properties of such faces need to be determined, comparison of the DRIFTS spectra in the isolated hydroxyl region for P90 and our sulfur free anatase(BC) provides little evidence for differences in the distribution of exposed facets, since the relative intensities are similar.

A second possibility may involve differences in the hydrophilicity of the anatase surface. We have previously shown that water serves as a co-catalyst in these reactions and there is an optimal water concentration for reactions with Ru/P90. We speculate that differential interaction with water may contribute to the differences in reactivity we observe. The low temperature synthesized and commercial anatase materials all show a broad hydrogen-bonded hydroxyl absorption region in DRIFTS that is not present for pyrogenic TiO_2. The absence of the 1620 cm^{-1} water bending mode suggests that this band is not associated with chemisorbed or physisorbed water but with hydroxyls that are present in more heterogeneous bonding conformations that hydrogen bond to nearby oxide oxygens. Furthermore, the low temperature anatase surfaces are much more hydrophilic than the pyrogenic anatase surface, and since water acts as a co-catalyst, with the DDO reaction rate going through a maximum as a function of water content in the feed, both in gas phase[154] and our liquid phase reactions, the more hydrophilic nature of these low temperature anatase surfaces may play a role. P90 interacts with water in a biphasic way, appearing initially to interact with water in a way that is very similar to the hydrophobic interaction between water and rutile, but later reacting rapidly with water in a way that is similar to the hydrophilic interaction between water and anatase.[158] Interestingly, Crossley *et al*. found no difference between the TOF for the DDO selectivity of cresol on Ru catalysts prepared on P25, rutile, and the anatase(AA) supports. The contrast between our work and that of Crossley, *et al.,* seems most likely to be due to gas phase vs. aqueous conditions. Further studies to explore, in detail, the role of water are underway.

The reaction between hydrogen and Ru generates water and this type of water might be contributing to the generation of new types of Lewis acid sites. Alternatively, differential catalyst activation pathways might be important in explaining the observed differences. All of the reactions reported are done in a batch reaction. Further studies that facilitate kinetic analysis of the reaction are also underway.

CHAPTER 4

IMPLICATIONS OF ELECTRON SCAVENGING CHARACTER OF SULFATED TITANIA FOR PHOTOCHEMISTRY

Knowledge of the electronic structure of photocatalysts is of immense importance in understanding and enhancing photocatalytic reactions. Here, we used *in-situ* DRIFTS during the reaction of TiO_2 with H_2 to reveal information about the electronic structure of TiO_2 as a function of crystal structure and chemical impurities. TiO_2 is n-doped upon H_2 dissociation and the corresponding electrons can be detected with FTIR if they are in either the conduction band or shallow trap states. However, electrons are not observed in the IR region when occupying deep traps. Our results are consistent with sulfate impurities in anatase creating deep trap states that scavenge electrons. These results provide support for a model of improved photocatalyst activity in which trapping the electrons increases the hole lifetime and increases the efficiency of oxidation reactions.

4.1. Introduction

Understanding the relationship between surface structure and trap states is critical for the rational design of photocatalysts. Chemical species such as hydroxyls, water, fluoride, and sulfate present on TiO_2 surfaces significantly change the structural and chemical properties of TiO_2.[43, 56, 172] Sulfate is one of the most important TiO_2 impurities to study because anatase TiO_2 is commercially produced in the presence of sulfate ions.[36] Density functional theory (DFT) cluster calculations of anatase TiO_2 show that sulfate induces structural changes and introduces empty states near the bottom of the band gap modifying the photoluminescence spectrum.[173] In addition, there are current efforts directed at improving the efficiency of TiO_2 photocatalysts via sulfation.[174-178] Sulfated anatase has higher efficiency for the photooxidation of organic molecules than pyrogenic TiO_2,[174-175, 178-179] which in turn is better than pure anatase.[60]

Several reasons for the increased activity of sulfated anatase, including increased surface acidity,[180] structural stability,[178, 181] and electron-hole separation assisted by the electron scavenger character of the sulfate species[174-175, 178-179, 182-184] have been proposed. Sulfur has been suggested to provide deep traps for electrons and therefore to increase the lifetime of holes.[175, 178-179] Although photoluminescence measurements demonstrate slower electron (e-)/hole (h+) recombination rates,[178] there is no direct evidence for the existence of deep traps on sulfated anatase. It is well established that adsorption of atomic hydrogen onto titania surfaces produces surface hydroxyl protons and electrons, and that changes in IR spectra can reveal whether these electrons fill conduction band states or shallow traps.[70, 108] Mid-gap states that are located at energies less than 1eV below the conduction band minimum (CBM) are called shallow trap (ST) states.[70, 185] Here, we report adsorption of H_2 and D_2 on pyrogenic titania (P90), rutile, several commercial anatase samples [Sigma Aldrich (SA), US Research Nanomaterials (USR), and Alfa Aesar (AA)] for which sulfate was detected, and our synthesized sulfate-free anatase. We observed the formation of surface hydroxyls and occupation of shallow traps by electrons for P90, rutile, and sulfate-free anatase. However, when sulfate is present on the TiO_2 surface, we continued to observe the formation of surface hydroxyls, but failed to observe electronic effects in the IR spectra. We ascribe the latter phenomenon to electrons being trapped in states deeper than the ~1eV range of mid-IR spectroscopy.

Light absorption in the mid-IR region by CB and ST electrons has been used to elucidate differences in the photocatalytic activity of different polymorphs of TiO_2[186-187] and to reveal the influence of surface species such as hydroxyls and water on the nature and dynamics of photoexcited electrons in TiO_2.[188-189] Both CB and ST electrons of metal oxides absorb light in the mid-IR region.[69-70, 190] Interaction of IR light with the CB electrons of semiconductors generates a broad featureless absorbance which increases toward lower wavenumbers with a power law, $\sim\omega^{-p}$ (with $p = 1.5 - 1.7$) $\sim\omega^{-p}$ and is not observable below the frequency where bulk phonon modes absorb strongly ($< \sim 1000$ cm^{-1}).[70] ST

electrons can be excited into the CB continuum with IR light in the 1000-4000 cm^{-1} region.[191-192] We have monitored the reaction of TiO_2 samples with H_2 using *in situ* diffuse reflectance Fourier transform infrared spectroscopy (DRIFTS) experiments to study the influence of TiO_2 crystal phase and surface composition on the electronic structure of TiO_2. Dihydrogen dissociates on pyrogenic titania (P25) above 250 °C to yield electrons and protons.[107] The protons bond to surface oxygens (to form hydroxyls) and the electrons accumulate in the CB and mid-gap states.[69-70, 108] To demonstrate the formation of surface hydroxyls from H_2 independent of the adsorption of background water, we performed our experiments under rigorously dry conditions (see section 4.3.3.3). Reactions with D_2 distinguished between electronic and vibrational contributions to the absorption spectra. Both surface and bulk impurities can introduce defect states in band structures.[67] Accordingly, we have characterized the composition and phase of these materials and cleaned them by *in situ* oxidation at temperatures up to 400 °C to achieve highly dehydroxylated surfaces with no detectable impurities, except for sulfur that was present on all commercially available anatase materials. To distinguish the influence of sulfur from the surface crystallographic structure of anatase, we synthesized sulfur-free anatase using a modified sol-gel method[83] and confirmed that similar facets are present on sulfate-free anatase, commercial anatase, and pyrogenic TiO_2 (*i.e.*, either P25 or P90) on the basis of DFT assignments of the isolated hydroxyl frequencies to specific anatase facets.[34, 165]

4.2. Materials and methods

Pyrogenic TiO_2 (P90) was purchased from Evonik and used as-received. Rutile was purchased from US Research Nanomaterials and used as-received. TiO_2 anatase (Sigma Aldrich, denoted "SA"), TiO_2 anatase (US Research Nanomaterials, denoted "USR"), TiO_2 anatase (Alfa Aesar, denoted "AA") were all purchased from their respective manufacturers. Since commercially available anatase samples contain sulfate impurities, which complicates the interpretation of spectral results, so we synthesized sulfate-free anatase using a modified sol-gel method described elsewhere,[83] as described in Chapter 1.

The TiO_2 materials were studied using XPS, ICP-OES, N_2 adsorption porosimetry, x-ray diffraction, and DRIFTS. All experimental details were as described in section 3.2.

4.3. Results and discussion

Physicochemical characterization of TiO_2 samples and DRIFTS studies of the electronic structure of TiO_2 using reaction with H_2/D_2 is presented in this section.

4.3.1. Physico-chemical characterization of samples

The sulfur 2p region of the XPS spectra of the samples are shown in Figure 4.1. Using the ratio of the S 2p and Ti 2p peak areas, we estimated the surface sulfate coverage on the TiO_2 surface, $\theta_S(\frac{atoms}{area})$, assuming sulfur was adsorbed only on the surface and that both core level peaks were attenuated by the carbonaceous layer, as described in section 3.3.1.

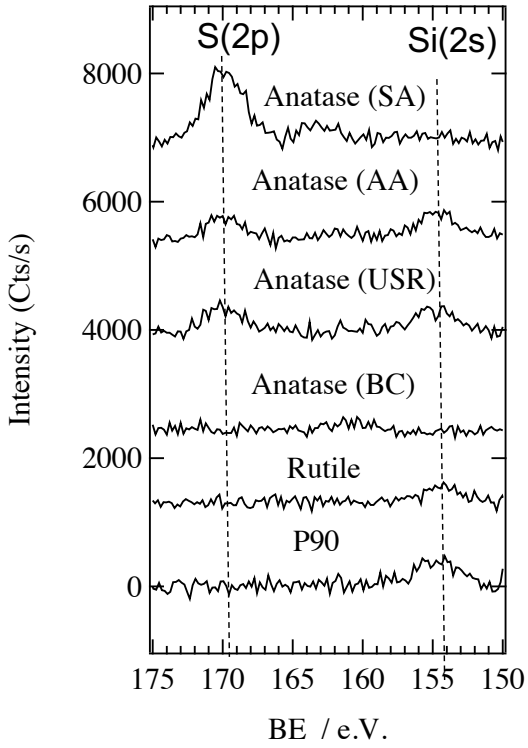

Figure 4.1. XPS of the TiO_2 samples in the sulfate region.

The sulfur coverage is shown in Table 4.1 for the sulfate adlayer model described in section 3.3.1. For comparison with the ICP-OES bulk composition, the estimated bulk sulfur content was calculated from the ratio of the mass of the sulfur adlayer to the mass of the spherical TiO_2 nanoparticle, expressed in ppm on a mass basis. The mass of sulfur on a spherical particle, whose diameter was chosen to give the BET surface area shown in Table 4.1, was calculated from the adlayer coverage from XPS and the particle area.

Table 4.1. Chemical and physical characterization of TiO_2 samples

Material		ICP-OES S content / ppm	XPS S coverage S atoms/ nm^2	BET surface area m^2/g	Estimated bulk S content/ppm	Total Pore Volume (cm^3/g)	BJH avg pore dia. (nm)
Pyrogenic	P90	<500	ND[a]	100	NA	0.35	19
Anatase	SA	3660	1.5	50[c]	4000	NA[b]	NA[b]
	AA	1361	0.47	136	3300	0.42	13
	USR	782	0.52	93	2500	0.35	14
	Sulfate-free	NA[b]	ND	159	NA	0.27	8
Rutile	USR rutile	<500	ND	33	NA	0.10	17

[a]Not Detected, [b]Not Available, [c]as specified by the manufacturer

X-ray diffractograms (Figure 4.2) of the anatase BC, SA, USR, and AA showed pure anatase phase, rutile shows pure rutile phase, while P90 shows 95% anatase and 5% rutile content. Figure 4.3. shows the XRD diffractograms of the as-prepared sulfate free anatase sample (Anatase BC), and the same sample after BET analysis and extensive calcination at 400 °C. As-prepared samples show lines characteristic of the anatase phase. Before BET analysis, the sample was subjected to evacuation at 350°C for 3 hours. XRD diffractograms of the sample after BET analysis shows line narrowing which is an indication of increase in the particle sizes. More XRD line narrowing was observed for the sample subjected to the extensive calcination at 400°C. However, the crystal structure of our sample did not change during such pretreatments.

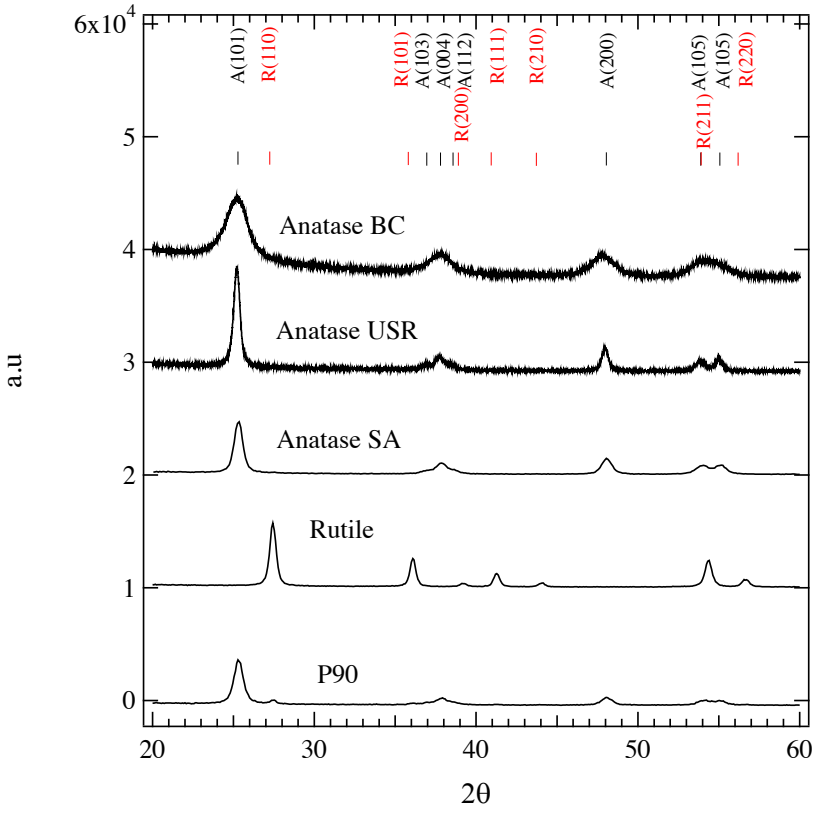

Figure 4.2. X-ray diffractograms of the TiO_2 samples.

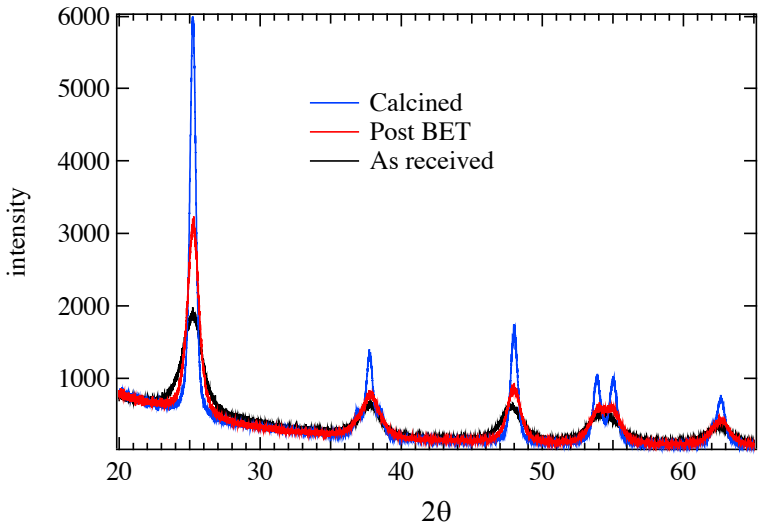

Figure 4.3. XRD analysis of sulfate free anatase (BC) samples after BET analysis and after extensive calcination at 400°C (for several days). Before the BET analysis, the sample was degassed at 350°C for 3 hours.

DRIFTS characterization of the TiO2 samples recorded during the calcination reveals the chemical impurities and temperature at which these impurities are eliminated, Figure 4.4. Surface impurities generally originate from the reaction of the surface with atmospheric gases, specifically water and carbon dioxide, and from chemical impurities introduced during material synthesis. DRIFTS spectra recorded during the temperature programmed calcination (TPC) of P90, rutile, and sulfate free anatase samples are reported elsewhere.[165] Molecular water is removed from TiO_2 samples after calcination at 200 °C, and carbonates/bicarbonates are removed at 300 °C.[165]

The DRIFT spectrum of as-received anatase (USR) recorded at 30 °C shows several impurities (Figure 4.4-A). The complex absorbance feature in the 3600-3800 cm^{-1} region is identified as arising from isolated hydroxyls.[42, 165] The broad absorbance feature in the 2500-3600 cm^{-1} region contains the OH stretches of water and H-bonded surface hydroxyls. The 1622 cm^{-1} band is assigned to the water bending mode.[42, 80] The assignment of the 1182 and 1323 cm^{-1} bands, based only on the spectrum recorded at 30 °C, is ambiguous. These bands could be either for the carbonate[61] or sulfate species.[168] Heating to 300 °C eliminates carbonate bands,[165] while the sulfate band persists and shifts to ~1360 cm^{-1} as the surface is dehydrated.[150, 168] The blue shift of the ~1323 cm^{-1} band to ~1360 cm^{-1} is characteristic of sulfated samples and is assigned to the S=O group of tridentate sulfate species.[168] The surface sulfate IR signature was also observed for the two other commercial anatase samples (see section 4.3.3. Supporting Information). The presence of sulfur on the surface was confirmed by XPS and ICP-OES analyses for these samples (Table 4.1). These tridentate sulfate species, along with molecular water and isolated surface hydroxyls, are removed from the anatase (USR) surface after calcination at 400 °C (see Figure 4.4-A). However, traces of the H-bonded surface hydroxyl band in the 2500-3500 cm^{-1} region remain. Similar results were obtained for the other two commercial anatase samples (see section 4.3.3.). Figure 4.4-B shows the DRIFTS spectra of the TiO_2 samples after calcination at 400 °C to illustrate the state of the surface and the remaining hydroxyl coverage before exposure to H_2 (and isotope exchange reactions

with D_2). All samples except P90 contained H-bonded surface hydroxyls at this point. The samples were heated at 400 °C until the sulfate band was not detectable (see section 4.3.3. Supporting Information).

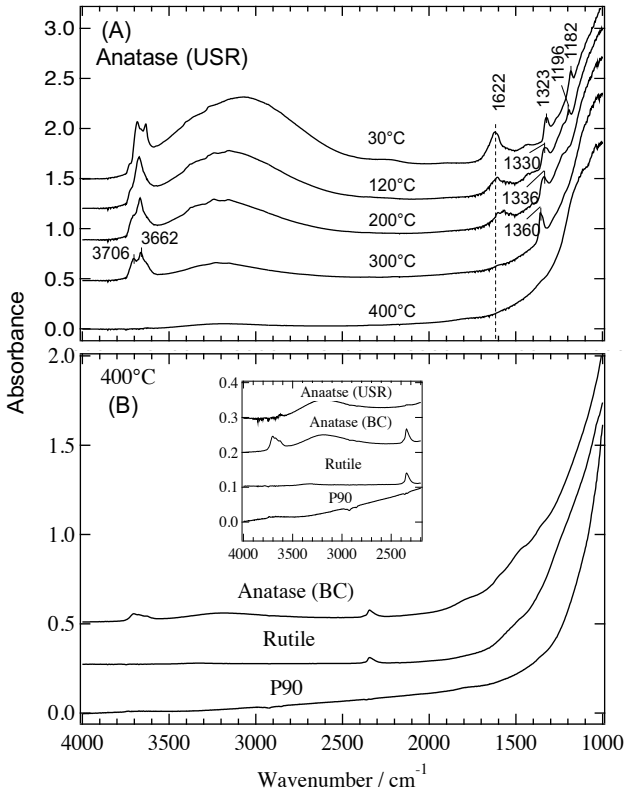

Figure 4.4. DRIFTS spectra of (A) anatase (USR) recorded during temperature programmed calcination at indicated temperatures, (B) representative TiO_2 samples after extensive calcination at 400°C. The inset shows the spectra in the hydroxyl region. All spectra are relative to KBr powder and offset for clarity.

4.3.2. Reaction with H_2/D_2

TiO_2 samples were exposed to H_2/D_2 after calcination at 400 °C. The sample temperature was subsequently reduced from 400 °C to 300 °C under dry O_2 flow and the cell was flushed with Ar at 300 °C for one hour to remove O_2. A reference spectrum was recorded after an hour of flushing with Ar at 300 °C and difference spectra were recorded as a function of time as the gas flow was alternated between H_2 (or D_2) and Ar.

Once P90 was exposed to H_2 (Figure 4.5-A), both vibrational and electronic absorbance features appeared in the spectra. The absence of a water bending band at 1620 cm^{-1} shows that the broad band in the 3000-3600 corresponds to H-bonded hydroxyls, indicating that molecular water produced at this temperature[110] is rapidly desorbed. Two types of isolated surface hydroxyls at 3673 and 3645 cm^{-1} were formed in addition to H-bonded hydroxyls. A broad electronic absorbance (BEA) feature appeared in the spectra at longer times and continued to grow with time under H_2 atmosphere. The spectral shape of the BEA feature increases from 4000 cm^{-1} to 1000 cm^{-1}, where it is cut off by phonon absorption at ~~1000 cm^{-1}. Similarly shaped features are found for P25 when the bare surface is exposed to atomic hydrogen;[70, 185] the Rh-[69] and Au-[193] decorated surfaces are exposed to molecular hydrogen; or the bare surface is thermally reduced.[70] Morris, *et al*. interpreted this BEA as being due to both CB and ST electrons.[70]

The surface hydroxyl peak intensity plateaus when steady state coverage is reached but the BEA intensity continues to grow. We interpret the continued growth of the BEA intensity as being due to the dissociation of H_2 to form hydroxyls,

$$H_2 + 2O_O^x \rightarrow 2HO_O^x + 2e^-, \quad (1)$$

followed by dehydroxylation to produce H_2O, oxygen vacancies, and electrons,

$$2HO_O^x \rightarrow O_O^x + V_O^{\bullet\bullet} + H_2O, \quad (2)$$

where Kröger-Vink notation is used.[194] If the rate of reaction 2 and the rate of desorption of water is fast compared to the rate of reaction 1, then the hydroxyl peak intensity remains small while electrons accumulate in the lowest unoccupied states in the surface and their excitation is detected as the BEA feature.

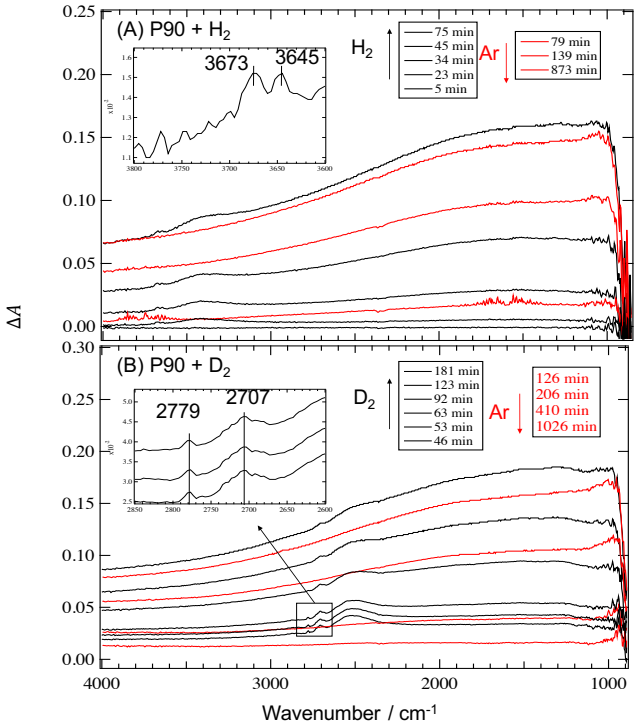

Figure 4.5. Difference DRIFTS spectra recorded during the reaction of P90 with (A) H_2 and (B) D_2. Black spectra were recorded under H_2 (D_2) and red spectra were recorded under Ar.

To distinguish electronic absorbance features from vibrational features, the surface was exposed to D_2 as well (Figure 4.5-B), and showed a BEA similar to that recorded under H_2. A broad band in the 2100-2700 cm^{-1} region and two distinct bands at 2707 and 2779 cm^{-1} were observed. The band at 2707 cm^{-1} is the deuterated equivalent of the 3673 cm^{-1} band, which is assigned to the bridging hydroxyls of the anatase (101) surface.[165] The 2779 cm^{-1} band is assigned to silica impurities,[165] consistent with silica impurities observed by XPS (Figure 4.1).

The intensity of the BEA feature increased with time under both H_2 and D_2 atmospheres. Once the gas flow was switched to Ar, the O-H and O-D bands disappeared rapidly due to dehydroxylation and oxygen vacancy formation while the intensity of the BEA decreased gradually. The intensity of the BEA feature decayed and grew when the gas was switched back and forth between Ar and H_2 (or D_2) atmospheres. The BEA features disappeared rapidly upon exposure of the sample to O_2, further

supporting the assignment to electronic features because O_2 is a known electron scavenger and re-oxidizes the vacancies formed by reaction 2.[45, 70, 186]

Because the prototypical photocatalysts, P25 and P90, contain both rutile and anatase phases, we performed similar experiments to determine whether or not the BEA of pyrogenic titania is simply a superposition of the BEA features of anatase and rutile. Exposure of rutile TiO_2 to H_2 (Figure 4.6-A) led to the formation of two isolated hydroxyls at 3655 and 3683 cm^{-1}, a broad H-bonded hydroxyl band (3000-3600 cm^{-1}), and a water bending mode at 1620 cm^{-1} revealing that traces of water were present on the rutile surface after reaction with H_2. Because the magnitude of the BEA for rutile is similar to that observed for P90, the reaction rates are comparable. The more intense OH stretching frequency compared to the BEA on rutile suggests that the rate of dehydroxylation is not as fast compared to the rate of H_2 dissociation for rutile.

When rutile was exposed to D_2 (Figure 4.6-B), the similarity of the BEA feature to that of reaction with H_2 (Figure 4.6-A) confirms its electronic origin. Again, the intensity of the BEA feature increased over a period of hours under D_2 flow. The BEA decreased slowly when the gas was switched from D_2 to Ar, but was removed immediately after exposure to O_2, suggesting an electronic origin of the BEA feature of rutile. However, the shape of the feature was different from those observed for P90. In contrast to the BEA feature observed for P90, the spectral intensity of the rutile BEA feature increases toward higher wavenumber. Moreover, the lack of absorbance at ~~1000 cm^{-1} provides no evidence for CB electrons in rutile. The absence of CB electrons' IR absorbance feature when rutile TiO_2 is n-doped by photoexcitation,[108, 186-187, 195-197] electrochemical excitation,[198-199] and exposure to atomic hydrogen[108] is reported and has been attributed to the greater depth of the trap states in rutile compared to the trap states of anatase.[186-187]

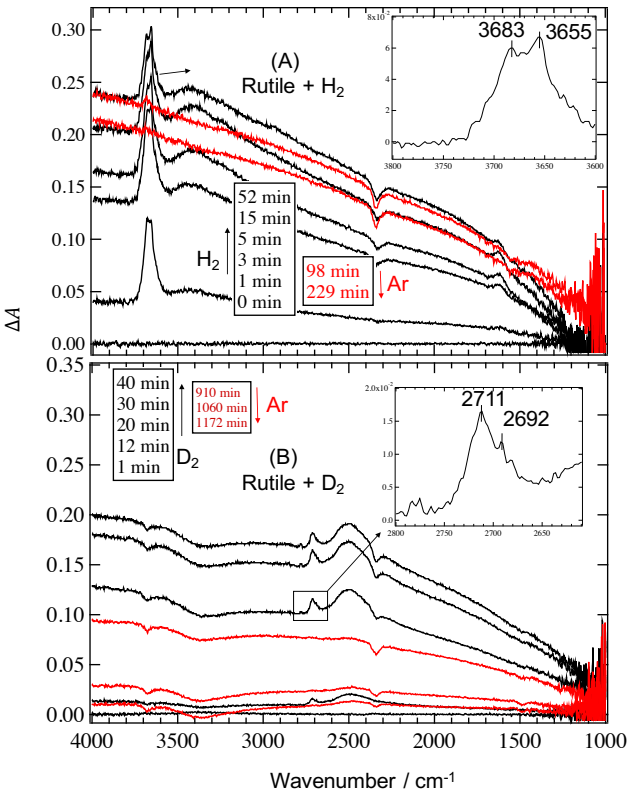

Figure 4.6. Difference DRIFTS spectra recorded during the reaction of the rutile sample with (A) H_2 and (B) D_2. Black spectra were recorded under H_2 (D_2) and red spectra were recorded under Ar.

Because the rutile surface was still partially hydroxylated after calcination at 400°C, H/D exchange happened after exposure to the molecular D_2 (Figure 4.6-B). The small negative-going bands due to isolated hydroxyls (3683 and 3655 cm^{-1}) and hydrogen bonded O-H (3200 – 3600 cm^{-1}), superimposed on the BEA feature, show that they exchange to form the corresponding O-D modes. The larger magnitude of the positive-going bands (2711 and 2692 cm^{-1}; 2400-2600 cm^{-1}) confirms dissociation of D_2, maintaining a steady state OD coverage, as the reaction generates electrons and the BEA intensity grows. The negative going CO_2 asymmetric stretch at 2350 cm^{-1} is due to changes in the optical sampling depth in DRIFTS, rather than loss of trapped CO_2, as it disappears when the BEA returns to baseline.

We now turn to the electronic features of sulfate free anatase, which is the majority component of P90. As shown in Figure 4.7-A, exposure of the 400 °C calcined anatase BC surface to H_2 produced an

intense BEA feature stretching from 1000 to 4000 cm^{-1}. The intensity of this feature increased with time under H_2, decreased slowly with time when the gas was switched back to Ar, and was eliminated immediately upon exposure to O_2 (see section 4.3.3. Supporting Information). Thus, the BEA feature is electronic in origin. However, the general shape of the BEA feature of sulfate-free anatase is different from that of P90. Indeed, subtracting the BEA feature of sulfate-free anatase from that of P90 gives rise to a difference spectrum that is well-described by the $\sim\omega^{-1.5}$ dependence for excitation of CB coupled with acoustic phonons[70] (Figure 4.7-B). This shows that the BEA of the sulfate-free anatase is due to the absorption of IR energy by ST electrons only. While IR absorption by CB electrons has previously been reported for pure anatase,[186-187, 195-199] Litke *et al.* have recently reported that the presence of water and the extent of hydroxylation of the surface will increase the density of trap states and prevent the delocalization of electrons in the CB.[188-189] Therefore, the observed difference between P90 and our sulfate-free anatase is not intrinsic to anatase TiO_2, but rather is due to a higher density of defects. The electrons will fill the associated Ti-OH traps before accumulating in the conduction band.

By comparison of the vibrational modes of sulfate-free anatase with P90, there are more hydrogen bonded OH (2500-3600 cm^{-1}) and some water (note the 1620 cm^{-1} bending band) formed in the reaction with H_2, which is attributed to the more hydrophilic nature of low temperature synthesized anatase.[34] The frequencies of the isolated hydroxyls (3648, 3671 cm^{-1}) are similar to those observed in P90, which indicates that the reactions are taking place on the same facets as on P90.[165] Figure 4.7-C shows spectra, measured out to 7000 cm^{-1}, for exposure of the 400 °C calcined anatase surface to D_2, confirming the strong BEA feature. Relative to the BEA, there are large negative-going isolated and hydrogen bonded hydroxyl features and corresponding positive-going deuterated features, that clearly illustrating the extent of hydroxylation prior to H/D exchange.

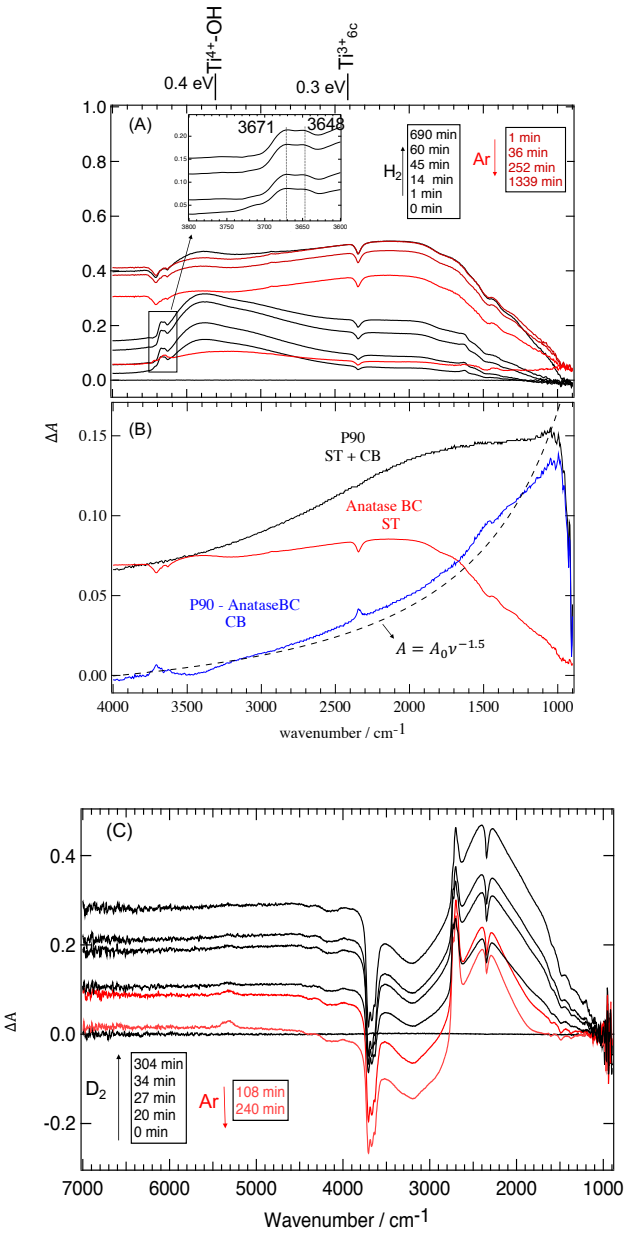

Figure 4.7. (A)Difference DRIFTS spectra of anatase BC after reaction with H_2 (black spectra) and when the gas was switched back to Ar (red spectra), (B) BEA feature of P90, anatase BC, difference spectrum where spectrum of P90 was subtracted from the spectrum of anatase BC, and the theoretical $\sim\omega^{-1.5}$ dependence for excitation of conduction band electrons (dashed line).[70] The schematics on the top of Figure 4A shows the calculated values of the trap states of anatase TiO_2 by Di Valentin et al.[67] Spectrum of the anatase BC was scaled (x0.18). (C) Difference DRIFTS spectra after reaction of anatase BC with D_2 (black spectra) and when the gas was switched back to Ar (red spectra), measured out to 7000 cm^{-1}.

In contrast with the behavior of all of the sulfate-free titania materials, no BEA features were observed for any of the sulfate containing anatase titania. Data in Figure 4.8 for anatase (USR) shows that exposure to H_2 produces hydrogen bonded surface hydroxyls (2500-3600 cm^{-1}) but no water (note absence of the bending band at 1620 cm^{-1}). The growth of these modes shows that dissociation of H_2 continued for hours under flowing H_2. When the sample was exposed to D_2, a negative absorbance feature in the 2500-3600 cm^{-1} region and positive absorbance features in the 1500-2600 cm^{-1} region were observed. These observations confirm that these features originate from vibration of O-H oscillators. Similar behavior was observed for anatase (SA) and anatase (AA) (see section 4.3.3. Supporting Information).

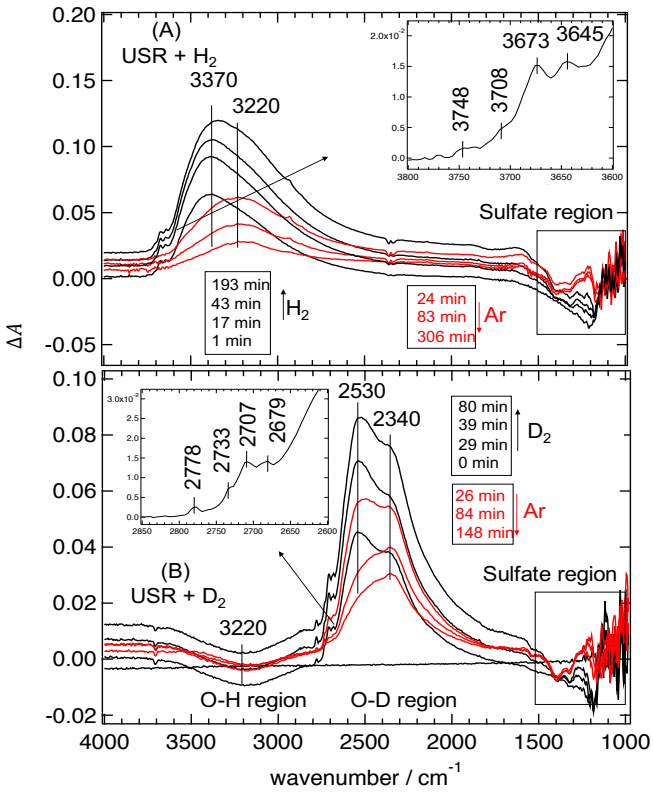

Figure 4.8. Difference DRIFTS spectra of USR anatase after reaction with (A) H_2 and (B) D_2. Black spectra were recorded under H_2 (D_2) and red spectra were recorded under Ar. Although H_2 dissociates to form hydroxyls, the absence of a broad background absorbance feature with electronic character implies that the electrons occupy deep traps.

In summary, DRIFTS spectra of the commercial, sulfated anatase samples recorded during exposure to H_2 and D_2 at 300 °C were different from those of P90, rutile, and sulfate free anatase in several ways: (1) a BEA feature with electronic character was not observed; and (2) there was a negative absorbance feature in the 1000-1500 cm^{-1} region. The formation of surface hydroxyls and molecular water (see section 4.3.3. Supporting Information) confirms the dissociation of H_2, and accumulation of electrons in the sulfated anatase. However, the lack of a BEA can only be explained if the electrons reside in traps deeper than the ~ 1eV photon energy of the mid-IR spectrometer, confirming previous suggestions that sulfate induces deep traps.[174-175, 179, 182, 184]

The BEA features we observed are well-described by recent electronic structure calculations. The plateaus in the absorption for the P90 and sulfate-free anatase samples are consistent with shallow traps at the defect state energies. Di Valentin *et al.*[67] explored defects in n-doped anatase titania and found defect states below the CBM for 6-coordinated Ti^{3+} interstitial sites at 0.3 eV (2149.5 cm^{-1}), 6-coordinated Ti^{3+}-OH sites at 0.4 eV (3226 cm^{-1}), 5-coordinated Ti^{3+} species of O-vacancies at 0.7 eV (5645.5 cm^{-1}), and the 5-coordinated Ti^{3+} interstitial sites at 0.8 eV (6452 cm^{-1}). The energy of the Ti^{3+} interstitial and Ti^{3+}-OH sites are shown at the top of Figure 4.7-A, consistent with assignment of the BEA to shallow traps. For rutile, DFT calculations[200-201] show that the energies of defect states are in the 0.7-1 eV range below the CBM, which is consistent with the ultraviolet photoelectron spectroscopy (UPS)[202] and electron energy loss spectroscopy (EELS)[81] experiments performed on rutile (110) single crystals. The peak in the UPS spectrum is around 0.7 eV, although the onset is near 0.25 eV, perhaps due to lifetime broadening. Consistently, we observe the onset in the electronic absorbance feature in Figure 4.6 for rutile around 1000 cm^{-1} (~ 0.1 eV), but the peak expected at 0.7 eV is beyond the 4000 cm^{-1} (~0.5 eV) range recorded. DFT cluster calculations of sulfated anatase shows that sulfate species create unoccupied states about 0.05 eV above the valence band maximum.[173] Therefore, sulfate trap states must be located roughly 3.2 eV below the CBM. Extensive formation of hydroxyls from H_2 on all sulfated anatase surfaces shows that H_2 dissociated and electrons were produced. Thus, the absence of electronic features in our DRIFTS spectra,

even measured up to 7500 cm^{-1} (0.93 eV) as shown in Figure 4.7-C, supports previous proposals that electrons occupy traps significantly deeper than 1 eV.

Thus, we showed that sulfate impurities change the electronic structure of anatase TiO_2 and act as electron scavengers when TiO_2 is n-doped, which has implications for the use of these materials as photocatalysts. It supports the general picture that the photocatalytic activity of TiO_2 is enhanced in the presence of electron scavengers, such as O_2, NO, metal ions, and more reducible metal oxides, because electron-hole recombination is slowed down by charge separation.[56]

4.3.3. Supporting information

In this section, DRIFTS spectra of other sulfated anatase samples (SA and AA) recorded during the pretreatments and during the reaction with H_2/D_2 are shown. In addition, results of a DRIFTS experiment to evaluate the dryness of our DRIFTS chamber are shown.

4.3.3.1. Anatase SA

Spectra presented in Figure 4.9. were recorded over several days as the sample was kept at 400°C under a dry O_2 flow. Water and carbonate species were gone at 400°C, while surface hydroxyls and sulfate bands were slowly eliminated from the TiO_2 samples at this temperature.[165] Our results showed that surface hydroxyls were slowly removed and only a band at 3625 cm^{-1} persists in the spectra. TiO_2 hydroxyls are generally removed at 400°C under our conditions.[165] The persistence of the 3625 cm^{-1} band could be related to the sulfated impurities.[203] Table 4.1 shows that anatase SA has the highest sulfur content among the commercial anatase samples studied in this work.

In the sulfate region of Figure 4.9., the tridentate sulfate band eliminates slowly at 400°C. In a parallel work, we showed that after pretreatment at 400 °C the sulfate level of the commercial anatase samples declined to a point that was not detected by XPS and ICP-OES analyses.[34] However, Figure 4.9 shows that there is a rather broad absorbance feature in the 1100-1250 cm^{-1} region that slowly grows as

the tridentate sulfate band is eliminated. This suggests that although tridentate sulfate species are largely eliminated, other forms of sulfur may be formed upon heating that are stable at 400°C.

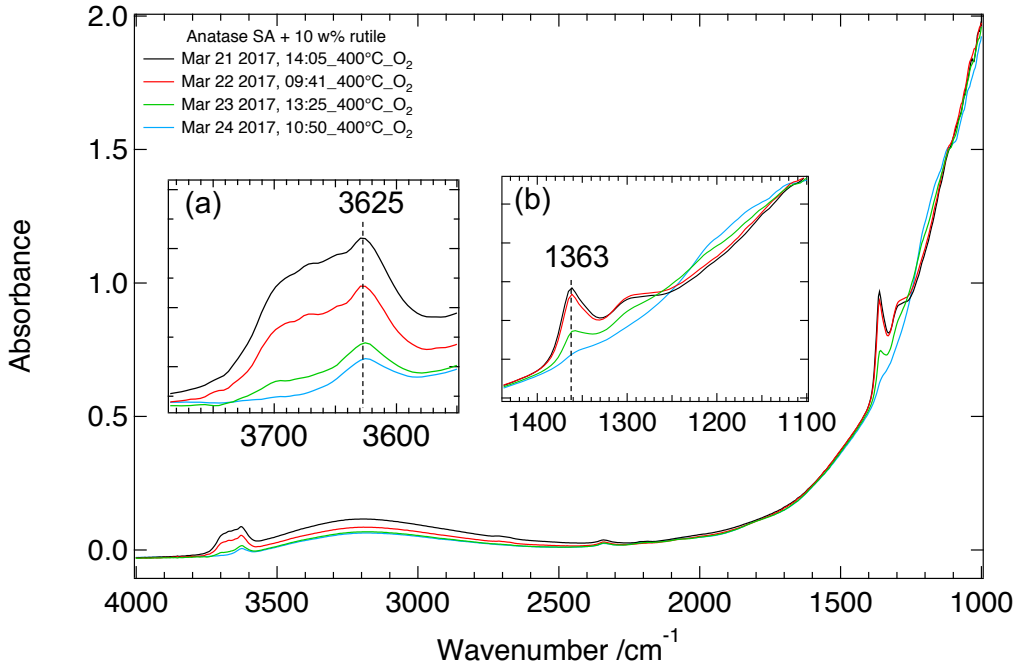

Figure 4.9. DRIFTS spectra recorded during the calcination of a mixture of anatase SA with rutile at 400°C. All the spectra are referenced to the single beam of KBr powder. The sample contained 10 w% rutile to simulate P90.

Figure 4.10 shows DRIFTS spectra recorded during the reaction of anatase SA with H_2 at 300 °C, after extensive calcination at 400 °C. The water bending band, H-bonded surface hydroxyls and isolated sulfate hydroxyls were formed after reaction with H_2. We did not observe the water bending band after reaction of anatase USR with H_2 (Figure 4.8). As discussed in the main text, this could be related to the hydroxylation/hydrophilicity of the surface. The anatase SA surface is more hydroxylated compared to other TiO_2 samples studied in this work.[34] A negative band at 1363 cm^{-1} shows that traces of tridentate sulfate species remained on the surface and reacted with water (the hydrogen dissociation products). In addition, there is a negative absorbance feature in the entire sulfate region (1000-1400 cm^{-1}). Intensity of the negative absorbance features increased with time under H_2 and decreased when the gas was switched

back to Ar. Absence of an electronic absorbance feature shows that electrons occupy deep traps induced by the sulfate species.

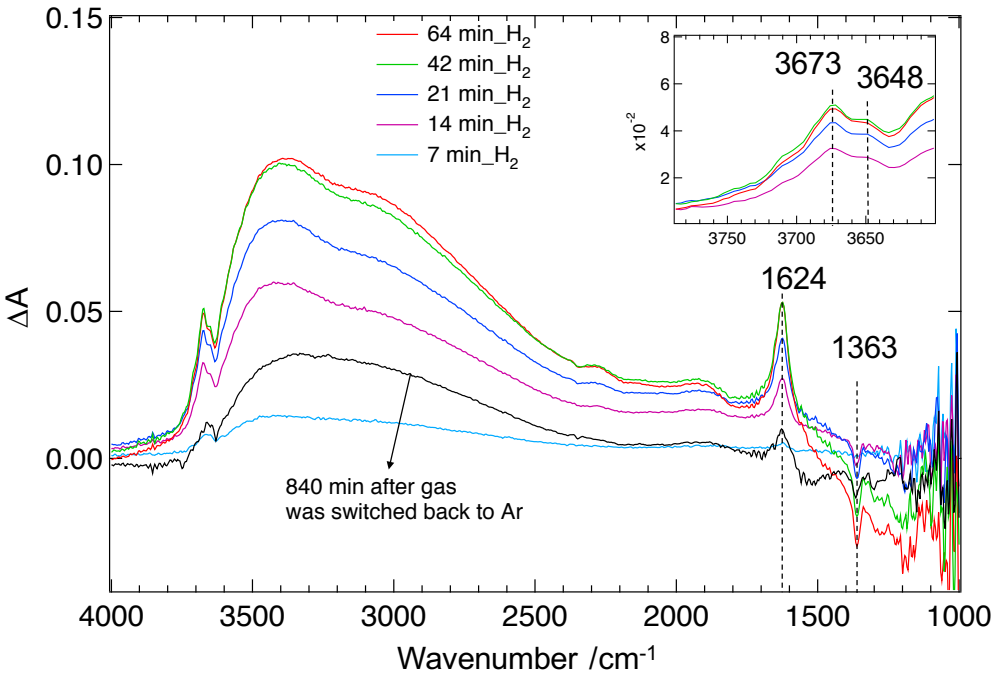

Figure 4.10. Difference DRIFTS spectra recorded during the reaction of a mixture of anatase and rutile with H_2 and when gas was switched back to Ar (black spectrum). Inset shows an expanded view of the isolated hydroxyls groups formed upon reaction with H_2.

Figure 4.11-A provides direct comparison between the sulfated anatase and sulfate free anatase in the spectra recorded up to 7000 cm^{-1}, the limit of out instrument. We did not observe a BEA for the sulfate sample; note that the background remains zero after reaction with H_2. On the other hand, as shown in Figure 4.11-B, reaction of the sulfate free anatase (anatase (BC)) with H_2 showed a BEA feature whose intensity continuously increased with time under H_2, did not change after 8 min exposure to Ar, and immediately dropped after exposure to O_2. Continuous growth of the BEA under H_2 shows that electrons are contineously added to the ST states of sulfate free anatase upon H_2 dissociation. Immediate removal of the BEA after exposure to O_2 is in support of the electronic origin of the BEA because O_2 is an electron

scavenger[56] and reacts with oxygen vacancies. Absence of the BEA in the sulfate samples showed that the depth of "sulfate trap" states must be more than 7000 cm^{-1} from the conduction band minimum.

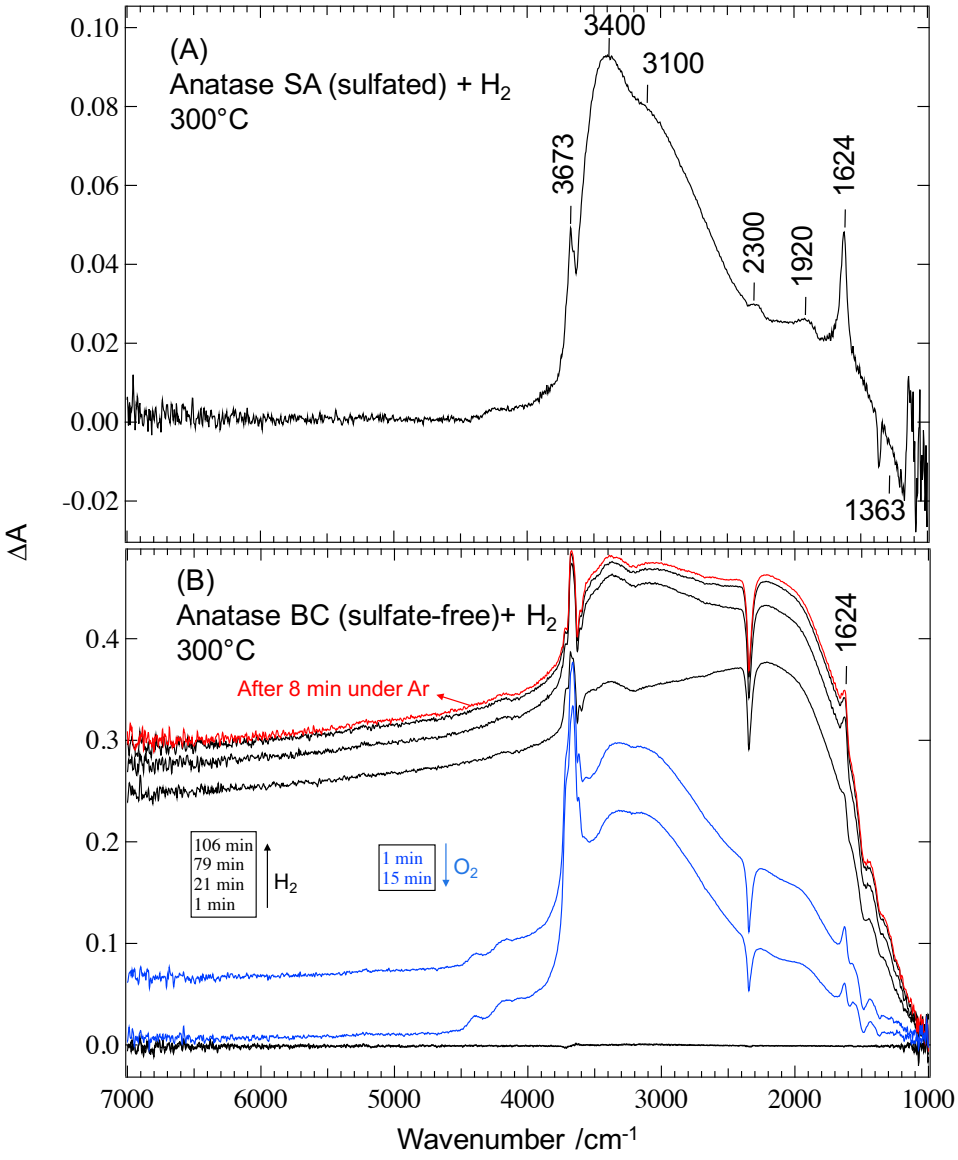

Figure 4.11. (A) Difference DRIFTS spectrum of anatase SA (sulfated) recorded after 28 min exposure to H_2 at 300°C showing there is no electronic absorption up to 7000 cm^{-1}. (**B**) Difference DRIFTS spectra recorded during the reaction of anatase BC (sulfate-free) with H_2 and when gas was switched back to Ar, and then to O_2. Comparison of (A) with (B) shows that while a broad background absorbance with electronic origin is observed for the sulfate free anatase, such a feature is absent in the sulfated samples.

Figure 4.12 shows the DRIFTS spectra recorded during the reaction of anatase SA with D_2. Initially, there were negative bands in the O-H region (both isolated and H-bonded) and positive bands in the O-D region. Intensity of both negative-going O-H bands and positive-going O-D bands increased with time under D_2. However, the intensity of the negative O-H bands stopped increasing after 20 min while the intensity of the positive O-D bands kept increasing. These observations showed that in addition to the H/D exchange, new O-D bands were formed upon D_2 dissociation over the sample at 300°C.

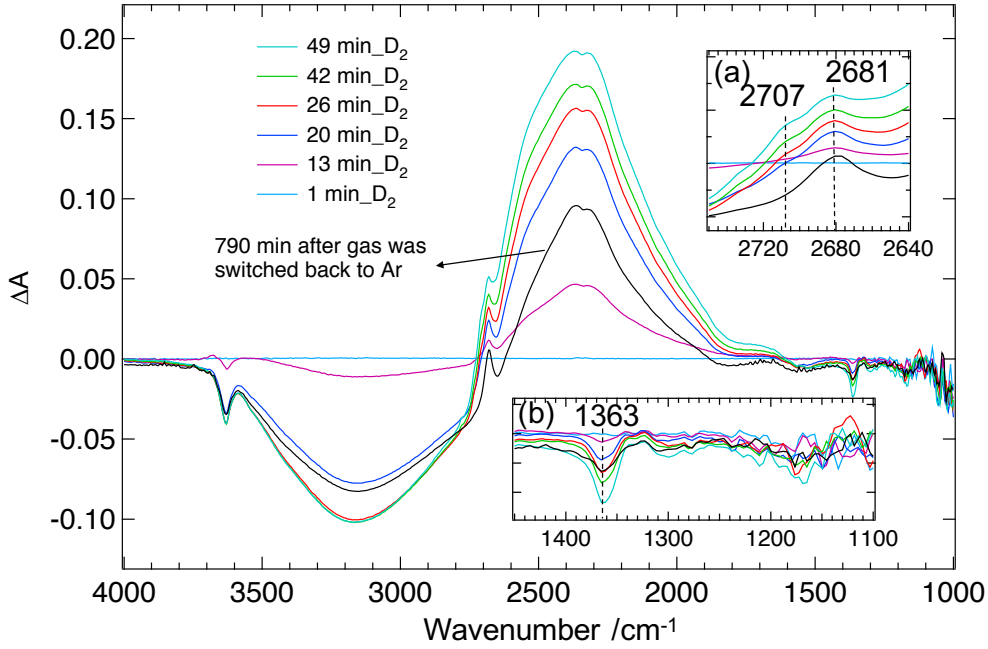

Figure 4.12. Difference DRIFTS spectra recorded during the reaction of anatase SA with D_2 and when the gas was switched back to Ar (black spectrum). Insets show the expanded view of the isolated hydroxyls and sulfate regions. 10w% rutile was added to this sample.

4.3.3.2. Anatase AA

DRIFTS spectra recorded during the step-wise calcination of anatase AA are shown in Figure 4.13. Our results showed that anatase AA surface was cleaned from molecular water and carbonates after calcination at 300°C. The tridentate sulfate band and isolated surface hydroxyl bands were removed after calcination at 400°C. H_2 adsorption experiments were performed on this surface.

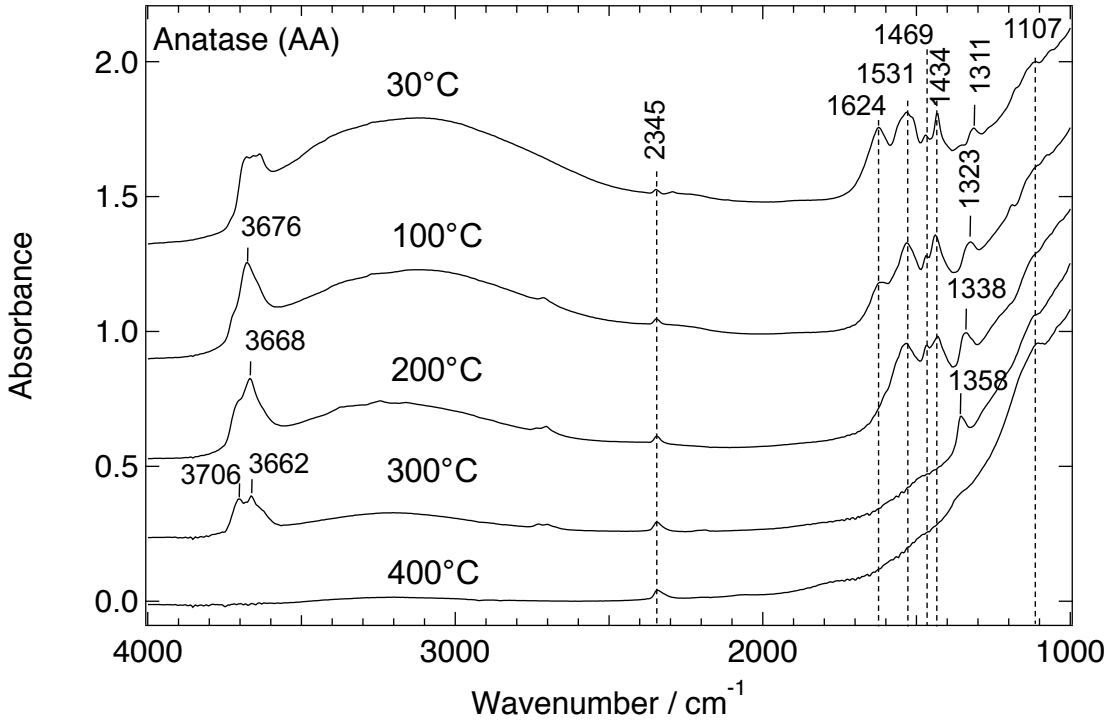

Figure 4.13. DRIFTS spectra recorded during the calcination of anatase Alfa-Aesar (surface area: 150 m^2/g). Sample was kept at each temperature for several hours (At least 8 hours). All the spectra were referenced to KBr powder

Figure 4.13 shows the DRIFTS spectra recorded during the exposure of anatase AA, calcined at 400 °C, to H_2 at 300 °C, and when gas was switched back to Ar. In general, similar features as for the two other commercial anatase samples were observed. However, the intensity of the water bending band formed after reaction with H_2 was intermediate between anatase USR (Figure 4.8) and anatase SA (Figure 4.10). Water is the reaction product of our experiments and we speculate that more hydroxylated surfaces

can retain water on the surface at 300°C for longer times. We did not observe an electronic absorbance feature for this sample and there was a negative absorbance feature in the sulfate region.

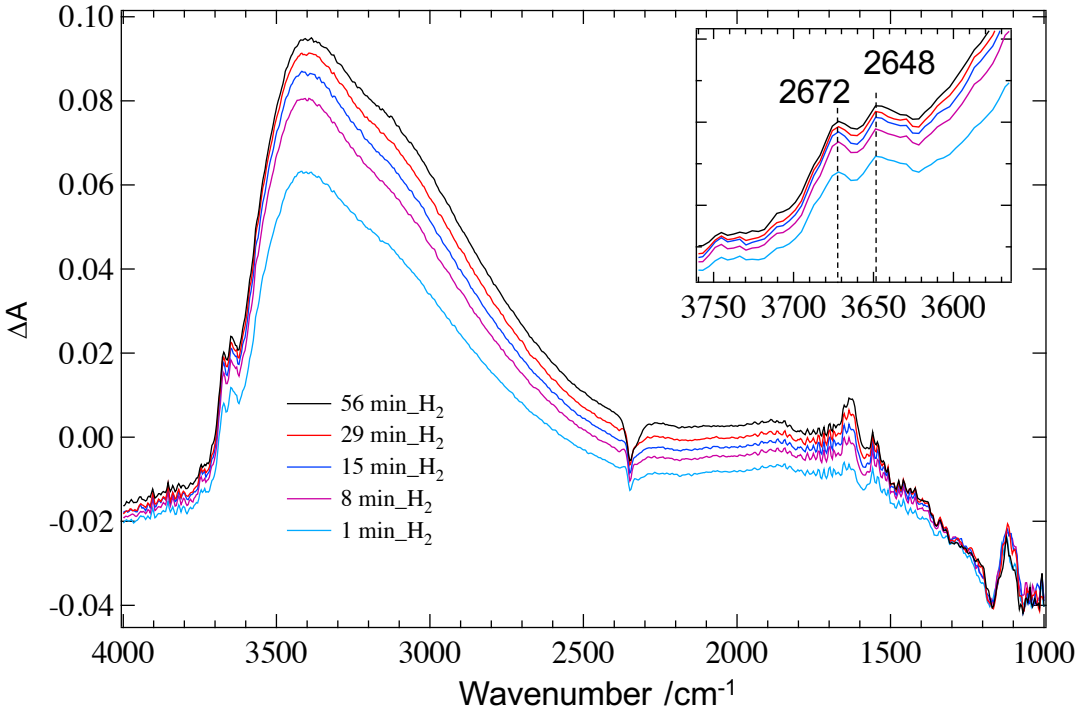

Figure 4.14. Difference DRIFTS spectra recorded during the reaction of anatase AA with H_2. Inset shows the expanded view of the isolated hydroxyls groups formed upon reaction with H_2.

4.3.3.3. Dryness test

Figure 4.15 illustrates the dryness level of our DRIFTS experimental conditions. TiO_2 surfaces are dehydrated at 300 °C. However, residual water molecules, that are always present on the cell walls, re-adsorb on the surface at lower temperatures.[47] Spectra depicted in Figure 4.15. shows that the water bending band did not appear in the spectra recorded under our experimental conditions within two hours after the temperature was reduced from 300°C to 30°C. However, the spectrum recorded after 18 h at room temperature shows that water gradually builds up on the surface and both the stretching and bending water band appear in the spectra. These results showed that our experiments were performed in dry conditions comparable to ultrahigh vacuum conditions. FTIR spectra recorded at room temperature, after

initial pretreatment at higher temperatures, under ultrahigh vacuum conditions usually show the water bending band.[47]

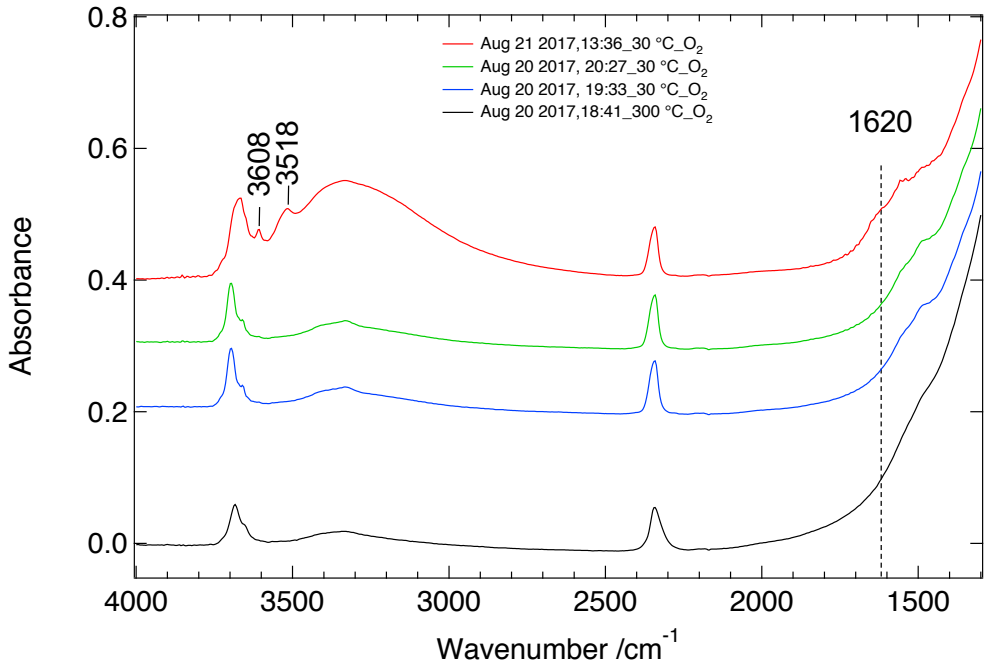

Figure 4.15. DRIFTS spectra of rutile sample recorded at 300°C, and when temperature was reduced to room temperature under dry O_2 flow.

REFERENCES

1. Chu, S.; Majumdar, A., Opportunities and challenges for a sustainable energy future. *Nature* 2012, *488* (7411), 294-303.

2. Nashawi, I. S.; Malallah, A.; Al-Bisharah, M., Forecasting World Crude Oil Production Using Multicyclic Hubbert Model. *Energy & Fuels* 2010, *24* (3), 1788-1800.

3. An Assesment of the Environmental Implications of Oil and Gas Production: A Regional Case Study. *U.S. Environmental Protection Agency* 2008.

4. Hausmann, P.; Sussmann, R.; Smale, D., Contribution of oil and natural gas production to renewed increase in atmospheric methane (2007–2014): top–down estimate from ethane and methane column observations. *Atmospheric Chemistry and Physics* 2016, *16* (5), 3227-3244.

5. IPCC, *Managing the Risks of Extreme Events and Disasters to Advance Climate Change Adaptation. A Special Report of Working Groups I and II of the Intergovernmental Panel on Climate Change* Cambridge University Press: Cambridge, UK, and New York, NY, USA, 2012.

6. Jiang, Z.; Xiao, T.; Kuznetsov, V. L.; Edwards, P. P., Turning carbon dioxide into fuel. *Philosophical Transactions of the Royal Society A: Mathematical, Physical and Engineering Sciences* 2010, *368* (1923), 3343.

7. EPA Lifecycle Analysis of Greenhouse Gas Emissions from Renewable Fuels. Environmental protection Agency, Ed. 2010.

8. Morales, M.; Quintero, J.; Conejeros, R.; Aroca, G., Life cycle assessment of lignocellulosic bioethanol: Environmental impacts and energy balance. *Renewable and Sustainable Energy Reviews* 2015, *42*, 1349-1361.

9. Rosegrant, M. W., Biofuels and Grain Prices: Impacts and Policy responses *International Food Policy Institute* 2008.

10. Searchinger, T.; Heimlich, R.; Houghton, R. A.; Dong, F.; Elobeid, A.; Fabiosa, J.; Tokgoz, S.; Hayes, D.; Yu, T.-H., Use of U.S. Croplands for Biofuels Increases Greenhouse Gases Through Emissions from Land-Use Change. *Science* 2008, *319*, 1238-1240.

11. Dickerson, K.; Rubin, J.; Kavkewitz, J., Biomass and Biofuels in Maine: Estimating Supplies for Expanding the Forest Products Industry. Margaret Chase Smith Policy Center, Forest Bioproducts Research Intiative, Univ. of Maine: 2007.

12. Huber, G. W., Breaking the Chemical and Engineering Barriers to Lignocellulosic Biofuels: Next Generation Hydrocarbon Biorefineries. National Science Foundation. Chemical Environmental, and Transport Systems Divisions, Bioengineering, Ed. NSF: Washington, D.C., 2008.

13. Huber, G. W.; Iborra, S.; Corma, A., Synthesis of Transportation Fuels from Biomass: Chemistry, Catalysts, and Engineering. *Chemical Reviews* 2006, 4044-4098.

14. Lin, Y.-C.; Huber, G. W., The critical role of heterogeneous catalysis in lignocellulosic biomass conversion. *Energy & Environmental Science* 2009, *2*, 68-80.

15. Anderson, R. B., *The Fischer-Tropsch Synthesis*. Academic Press, Inc. (Harcourt Brace Jovanovich): New York, 1984.

16. Swanson, R. M.; Platon, A.; Satrio, J. A.; Brown, R. C., Techno-economic analysis of biomass-to-liquids production based on gasification. *Fuel* 2010, *89* (Suppl. 1), S11-S19.

17. Wright, M. M.; Brown, R. C.; Boateng, A. A., Distributed processing of biomass to bio-oil for subsequent production of Fischer-Tropsch liquids. *Biofuels, Bioprod. Biorefin.* 2008, *2* (3), 229-238.

18. DeSisto, W. J.; Hill, N.; Beis, S. H.; Mukkamala, S.; Joseph, J.; Baker, C.; Ong, T.-H.; Stemmler, E. A.; Wheeler, M. C.; Frederick, B. G.; van Heiningen, A., Fast Pyrolysis of Pine Sawdust in a Fluidized-Bed Reactor. *Energy & Fuels* 2010, *24*, 2642-2651.

19. Joseph, J. Chemical Composition, Aging Reactions, and Stabilization of Bio-Oils. Ph.D., Univ. of Maine, Orono, ME, 2014.

20. DeSisto, W. J.; Wheeler, M. C., A funnel plot to assess energy yield and oil quality for pyrolysis-based processes. *Biomass & Bioenergy* 2016, *93*, 254-258.

21. Bozell, J. J.; Petersen, G. R., Technology development for the production of biobased products from biorefinery carbohydrates-the US Department of Energy's "Top 10" revisited. *Green Chemistry* 2010, *12* (4), 539-554.

22. van Heiningen, A., Converting a Kraft Pulp Mill into an Integrated Forest Products Biorefinery. *Pulp Pap. Can.* 2006, *107* (6), 38-43.

23. Upton, B. M.; Kasko, A. M., Strategies for the Conversion of Lignin to High-Value Polymeric Materials: Review and Perspective. *Chem Rev* 2016, *116* (4), 2275-306.

24. Zhang, X.; Wilson, K.; Lee, A. F., Heterogeneously Catalyzed Hydrothermal Processing of C5-C6 Sugars. *Chem Rev* 2016, *116* (19), 12328-12368.

25. Tunc, M. S.; Chheda, J.; van der Heide, E.; Morris, J.; van Heiningen, A., Two-Stage Fractionation and Fiber Production of Lignocellulosic Biomass for Liquid Fuels and Chemicals. *Industrial & Engineering Chemistry Research* 2013, *52* (36), 13209-13216.

26. Schwartz, T. J.; O'Neill, B. J.; Shanks, B. H.; Dumesic, J. A., Bridging the Chemical and Biological Catalysis Gap: Challenges and Outlooks for Producing Sustainable Chemicals. *ACS Catalysis* 2014, *4* (6), 2060-2069.

27. Wang, H.; Tucker, M.; Ji, Y., Recent Development in Chemical Depolymerization of Lignin: A Review. *Journal of Applied Chemistry* 2013, *2013*, 1-9.

28. Brittain, A. D.; Chrisandina, N. J.; Cooper, R. E.; Buchanan, M.; Cort, J. R.; Olarte, M. V.; Sievers, C., Quenching of reactive intermediates during mechanochemical depolymerization of lignin. *Catalysis Today* 2018, *302*, 180-189.

29. Dier, T. K. F.; Rauber, D.; Durneata, D.; Hempelmann, R.; Volmer, D. A., Sustainable Electrochemical Depolymerization of Lignin in Reusable Ionic Liquids. *Sci Rep* 2017, *7* (1), 5041.

30. Beis, S. H.; Mukkamala, S.; Hill, N.; Joseph, J.; Baker, C.; Jensen, B.; Stemmler, E. A.; Wheeler, M. C.; Frederick, B. G.; van Heiningen, A.; Berg, A. G.; DeSisto, W. J., Fast Pyrolysis of Lignins. *Bioresources* 2010, *5*, 1408-1424.

31. Saidi, M.; Samimi, F.; Karimipourfard, D.; Nimmanwudipong, T.; Gates, B. C.; Rahimpour, M. R., Upgrading of lignin-derived bio-oils by catalytic hydrodeoxygenation. *Energy Environ. Sci.* 2014, *7* (1), 103-129.

32. Newman, C.; Zhou, X.; Goundie, B.; Ghampson, I. T.; Pollock, R. A.; Ross, Z.; Wheeler, M. C.; Meulenberg, R. W.; Austin, R. N.; Frederick, B. G., Effects of support identity and metal dispersion in supported ruthenium hydrodeoxygenation catalysts. *Applied Catalysis A: General* 2014, *477*, 64-74.

33. Nelson, R. C.; Baek, B.; Ruiz, P.; Goundie, B.; Brooks, A.; Wheeler, M. C.; Frederick, B. G.; Grabow, L. C.; Austin, R. N., Experimental and Theoretical Insights into the Hydrogen-Efficient Direct Hydrodeoxygenation Mechanism of Phenol over Ru/TiO_2. *ACS Catal.* 2015, *5*, 6509-6523.

34. Husremovic, S.; Mahdavi-Shakib, A.; Ki, S.; Glynn, J.; Bannerjee, S.; Arce-Ramos, J. M.; Grabow, L. C.; Schwartz, T. J.; Billinge, S.; Nelson, R. C.; Zangiabadi, A.; Barmak, K.; Frederick, B. G.; Austin, R. N., Does the crystal structure of titania impact the effectiveness of Ru/TiO_2 direct deoxygenation catalysts? *(in prep)* 2018.

35. Li, G.; Li, L.; Boerio-Goates, J.; Woodfield, B. F., High Purity Anatase TiO_2 Nanocrystals: Near Room-Temperature Synthesis, Grain Growth Kinetics, and Surface Hydration Chemistry. *J. Am. Chem. Soc* 2005, *127*, 8659-8666.

36. Hadjiivanov, K. I.; Klissurski, D. G., Surface Chemistry of Titania (Anatase) and Titania-supported Catalysts. *Chem. Soc. Rev.* 1996, *107*, 534-545.

37. Ohno, T.; Sarukawa, K.; Tokieda, K.; Matsumura, M., Morphology of a TiO_2 Photocatalyst (Degussa, P-25) Consisting of Anatase and Rutile Crystalline Phases. *Journal of Catalysis* 2001, *203* (1), 82-86.

38. Datye, A. K.; Riegel, G.; Bolton, J. R.; Huang, M.; Prairie, M. R., Microstructural Characterization of a Fumed Titanium Dioxide Photocatalyst. *Journal of Solid State Chemistry* 1995, *115*, 236-239.

39. Roger I. Bickley; Teresita Gonzalez-Carreno; John S. Lees; Leonardo Palmisano; Tilley, R. J. D., A Structural Investigation of Titanium Dioxide Photocatalyts. *J. Solid. State. Chem.* 1991, *92*, 178.

40. Mino, L.; Spoto, G.; Bordiga, S.; Zecchina, A., Particles Morphology and Surface Properties As Investigated by HRTEM, FTIR, and Periodic DFT Calculations: From Pyrogenic TiO_2 (P25) to Nanoanatase. *The Journal of Physical Chemistry C* 2012, *116* (32), 17008-17018.

41. Hernandez-Mejia, C.; Gnanakumar, E. S.; Olivos-Suarez, A.; Gascon, J.; Greer, H. F.; Zhou, W.; Rothenberg, G.; Raveendran Shiju, N., Ru/TiO_2-catalysed hydrogenation of xylose: the role of the crystal structure of the support. *Catal. Sci. Technol.* 2016, *6* (2), 577-582.

42. Arrouvel, C.; Digne, M.; Breysse, M.; Toulhoat, H.; Raybaud, P., Effects of morphology on surface hydroxyl concentration: a DFT comparison of anatase–TiO_2 and γ-alumina catalytic supports. *Journal of Catalysis* 2004, *222* (1), 152-166.

43. Diebold, U., The Surface Science of Titanium Dioxide. *Surface Science Reports* 2003, *48*, 53-229.

44. Steven H. Szczepankiewicz; A. J. Colussi; Hoffmann, M. R., Infrared Spectra of Photoinduced Species on Hydroxylated Titania Surfaces. *J. Phys. Chem. B.* 2000, *104*, 9842-9850.

45. Szczepankiewicz, S. H.; Moss, J. A.; Hoffmann, M. R., Electron Traps and the Stark Effect on Hydroxylated Titania Photocatalysts. *J. Phys. Chem. B.* 2002, *106*, 7654-7658.

46. Nanayakkara, C. E.; Pettibone, J.; Grassian, V. H., Sulfur dioxide adsorption and photooxidation on isotopically-labeled titanium dioxide nanoparticle surfaces: roles of surface hydroxyl groups and adsorbed water in the formation and stability of adsorbed sulfite and sulfate. *Phys Chem Chem Phys* 2012, *14* (19), 6957-66.

47. Deiana, C.; Fois, E.; Coluccia, S.; Martra, G., Surface Structure of TiO_2 P25 Nanoparticles: Infrared Study of Hydroxy Groups on Coordinative Defect Sites. *J. Phys. Chem. C* 2010, *114*, 21531-21538.

48. Dzwigaj, S.; Arrouvel, C.; Breysse, M.; Geantet, C.; Inoue, S.; Toulhoat, H.; Raybaud, P., DFT makes the morphologies of anatase-TiO_2 nanoparticles visible to IR spectroscopy. *Journal of Catalysis* 2005, *236* (2), 245-250.

49. Thompson, T. L.; Yates, J. T., Jr. , Surface Science Studies of the Photoactivation of TiO_2 -New Photochemical Processes. *Chem. Rev.* 2006, *106*, 4428-4453.

50. Tykhon Zubkov; Dirk Stahl; Tracy L. Thompson; Dimitar Panayotov; Oliver Diwald; John T. Yates, J., Ultraviolet Light-Induced Hydrophilicity Effect on TiO_2(110)(1×1). Dominant Role of the Photooxidation of Adsorbed Hydrocarbons Causing Wetting by Water Droplets. *J. Phy. Chem. B* 2005, *109*, 15454-15462.

51. Posternak, M.; Baldereschi, A.; Delley, B., Dissociation of Water on Anatase TiO_2 Nanoparticles: the Role of Undercoordinated Ti Atoms at Edges. *J. Phys. Chem. C* 2009, *113*, 15862-15867.

52. Vimont, A.; Thibault-Starzyk, F.; Daturi, M., Analysing and understanding the active site by IR spectroscopy. *Chem Soc Rev* 2010, *39* (12), 4928-50.

53. Zaera, F., New advances in the use of infrared absorption spectroscopy for the characterization of heterogeneous catalytic reactions. *Chem Soc Rev* 2014, *43* (22), 7624-63.

54. Wang, Y.; Woll, C., IR spectroscopic investigations of chemical and photochemical reactions on metal oxides: bridging the materials gap. *Chem Soc Rev* 2017, *46* (7), 1875-1932.

55. Petrik, N. G.; Kimmel, G. A., Reaction Kinetics of Water Molecules with Oxygen Vacancies on Rutile TiO_2(110). *The Journal of Physical Chemistry C* 2015, *119* (40), 23059-23067.

56. Henderson, M. A., A Surface Science Perspective on TiO_2 Photocatalysis. *Surface Science Reports* 2011, *66* (6-7), 185-297.

57. Yin, X. L.; Calatayud, M.; Qiu, H.; Wang, Y.; Birkner, A.; Minot, C.; Woll, C., Diffusion versus desorption: complex behavior of H atoms on an oxide surface. *Chemphyschem* 2008, *9* (2), 253-6.

58. Sang, L.; Zhao, Y.; Burda, C., TiO_2 nanoparticles as functional building blocks. *Chem Rev* 2014, *114* (19), 9283-318.

59. De Angelis, F.; Di Valentin, C.; Fantacci, S.; Vittadini, A.; Selloni, A., Theoretical studies on anatase and less common TiO_2 phases: bulk, surfaces, and nanomaterials. *Chem Rev* 2014, *114* (19), 9708-53.

60. Hurum, D. C.; Agrios, A. G.; Gray, K. A., Explaining the Enhanced Photocatalytic Activity of Degussa P25 Mixed-Phase TiO_2 Using EPR. *The Journal of Physical Chemistry B* 2003, *107*, 4545-4549.

61. Mino, L.; Spoto, G.; Ferrari, A. M., CO_2 Capture by TiO_2 Anatase Surfaces: A Combined DFT and FTIR Study. *The Journal of Physical Chemistry C* 2014, *118* (43), 25016-25026.

62. Simonsen, M. E.; Li, Z.; Søgaard, E. G., Influence of the OH groups on the photocatalytic activity and photoinduced hydrophilicity of microwave assisted sol–gel TiO_2 film. *Applied Surface Science* 2009, *255* (18), 8054-8062.

63. Wu, C.-Y.; Tu, K.-J.; Deng, J.-P.; Lo, Y.-S.; Wu, C.-H., Markedly Enhanced Surface Hydroxyl Groups of TiO_2 Nanoparticles with Superior Water-Dispersibility for Photocatalysis. *Materials* 2017, *10* (5), 566.

64. Berger, T.; Sterrer, M.; Diwald, O.; Knözinger, E.; Panayotov, D.; Thompson, T. L.; Yates, J. T., Light-Induced Charge Separation in Anatase TiO_2 Particles. *The Journal of Physical Chemistry B* 2005, *109* (13), 6061-6068.

65. Panayotov, D. A.; Yates, J. T., Depletion of conduction band electrons in TiO_2 by water chemisorption – IR spectroscopic studies of the independence of Ti–OH frequencies on electron concentration. *Chemical Physics Letters* 2005, *410* (1-3), 11-17.

66. Lobo-Lapidus, R. J.; Gates, B. C., Probing surface sites of TiO_2: reactions with [$HRe(CO)_5$] and [$CH_3Re(CO)_5$]. *Chemistry* 2010, *16* (37), 11386-98.

67. Di Valentin, C.; Pacchioni, G.; Selloni, A., Reduced and n-Type Doped TiO_2: Nature of Ti^{3+} Species. *The Journal of Physical Chemistry C* 2009, *113*, 20543-20552.

68. Mahdavi-Shakib, A.; Rahmani-Chokanlu, A.; Schwartz, T. J.; Austin, R. N.; Frederick, B. G., Implications of Electron Scavanging Character of Sulfated Titania for Photochemistry. *(in prep)* 2018.

69. Panayotov, D.; Ivanova, E.; Mihaylov, M.; Chakarova, K.; Spassov, T.; Hadjiivanov, K., Hydrogen spillover on Rh/TiO_2: the FTIR study of donated electrons, co-adsorbed CO and H/D exchange. *Phys Chem Chem Phys* 2015, *17* (32), 20563-73.

70. Panayotov, D. A.; Burrows, S. P.; Morris, J. R., Infrared Spectroscopic Studies of Conduction Band and Trapped Electrons in UV-Photoexcited, H-Atom n-Doped, and Thermally Reduced TiO_2. *The Journal of Physical Chemistry C* 2012, *116* (7), 4535-4544.

71. Michel Primet; Pierre Pichat; Mathieu, M.-V., Infrared Study of the Surface of Titanium Dioxide. I. Hydroxyl Groups *The Journal of Physical Chemistry* 1971, *75*, 1216-1220.

72. Tsyganenko, A. A.; Filimonov, V. N., Inrared Spectra of Surface Hydroxyls Groups and Crystaline Structure of Oxides *Journal of Molecular Structure* 1973, *19*, 579-589.

73. Liu, C.; Ma, Q.; He, H.; He, G.; Ma, J.; Liu, Y.; Wu, Y., Structure–activity relationship of surface hydroxyl groups during NO2 adsorption and transformation on TiO_2 nanoparticles. *Environmental Science: Nano* 2017, *4* (12), 2388-2394.

74. Rustad, J. R.; Boily, J. F., Density functional calculation of the infrared spectrum of surface hydroxyl groups on goethite (-FeOOH). *American Mineralogist* 2010, *95* (2-3), 414-417.

75. Chizallet, C.; Digne, M.; Arrouvel, C.; Raybaud, P.; Delbecq, F.; Costentin, G.; Che, M.; Sautet, P.; Toulhoat, H., Insights into the Geometry, Stability and Vibrational Properties of OH Groups on gamma-Al_2O_3, TiO_2-Anatase and MgO from DFT Calculations. *Topics in Catalysis* 2009, *52* (8), 1005-1016.

76. Sun, C.; Liu, L.-M.; Selloni, A.; Lu, G. Q.; Smith, S. C., Titania-water interactions: a review of theoretical studies. *Journal of Materials Chemistry* 2010, *20* (46), 10319.

77. Tilocca, A.; Selloni, A., Structure and Reactivity of Water Layers on Defect-Free and Defective Anatase TiO_2(101) Surfaces. *J. Phy. Chem. B* 2004, *108*, 4743-4751.

78. Tilocca, A.; Selloni, A., Reaction pathway and free energy barrier for defect-induced water dissociation on the (101) surface of TiO_2-anatase. *The Journal of Chemical Physics* 2003, *119* (14), 7445-7450.

79. Nadeem, I. M.; Harrison, G. T.; Wilson, A.; Pang, C. L.; Zegenhagen, J.; Thornton, G., Bridging Hydroxyls on Anatase TiO_2(101) by Water Dissociation in Oxygen Vacancies. *J Phys Chem B* 2018, *122* (2), 834-839.

80. Henderson, M. A., An HREELS and TPD study of water on TiO_2 (ll0): the extent of molecular versus dissociative adsorption. *Surface Science* 1996, *355*, 151-166.

81. Henderson, M. A.; Epling, W. S.; Peden, C. H. F.; Perkins, C. L., Insights into Photoexcited Electron Scavenging Processes on TiO_2 Obtained from Studies of the Reaction of O_2 with OH Groups Adsorbed at Electronic Defects on TiO_2 (110). *The Journal of Physical Chemistry B* 2003, *107*, 534-545.

82. Brookes, I. M.; Muryn, C. A.; Thornton, G., Imaging Water Dissociation on TiO_2 (110). *Phys Rev Lett* 2001, *87* (26), 266103.

83. Li, G.; Li, L.; Boerio-Goates, J.; Woodfield, B. F., High Purity Anatase TiO_2 Nanocrystals: Near Room-Temperature Synthesis, Grain Growth Kinetics, and Surface Hydration Chemistry. *J. Am. Chem. Soc.* 2005, *127*, 8659-8666.

84. Couble, J.; Gravejat, P.; Gaillard, F.; Bianchi, D., Quantitative analysis of infrared spectra of adsorbed species using transmission and diffuse reflectance modes: Case study: Heats of adsorption of CO on TiO_2 and CuO/Al_2O_3. *Applied Catalysis A: General* 2009, *371* (1), 99-107.

85. Meunier, F. C., Pitfalls and benefits of in situ and operando diffuse reflectance FT-IR spectroscopy (DRIFTS) applied to catalytic reactions. *Reaction Chemistry & Engineering* 2016, *1* (2), 134-141.

86. Kresse, G.; Furthmüller, J., Efficiency of ab-initio Total Energy Calculations for Metals and Semiconductors using a Plane-Wave Basis Set. *Comput. Mater. Sci.* 1996, *6*, 15-50.

87. Kresse, G.; Hafner, J., Ab Initio Molecular Dynamics for Open-Shell Transition Metals. *Phys. Rev. B* 1993, *48*, 13115-13118.

88. Kresse, G.; Hafner, J., Ab initio molecular-dynamics simulation of the liquid-metal-amorphous-semiconductor transition in germanium. *Physical Review B* 1994, *49* (20), 14251-14269.

89. Bohn, S. R.; Jacobsen, K. W., An object-oriented scripting interface to a legacy electronic structure code. *J. Comput. Sci. Eng.* 2002, *4* (3), 56-66.

90. Blöchl, P. E., Projector augmented-wave method. *Physical Review B* 1994, *50* (24), 17953-17979.

91. Hammer, B.; Hansen, L. B.; Nørskov, J. K., Improved adsorption energetics within density-functional theory using revised Perdew-Burke-Ernzerhof functionals. *Physical Review B* 1999, *59* (11), 7413-7421.

92. Perdew, J. P.; Burke, K.; Ernzerhof, M., Generalized Gradient Approximation Made Simple. *Physical Review Letters* 1996, *77* (18), 3865-3868.

93. Stevens, E. D.; Rys, J.; Coppens, P., Quantitative comparison of theoretical calculations with the experimentally determined electron density distribution of formamide. *Journal of the American Chemical Society* 1978, *100* (8), 2324-2328.

94. Dudarev, S. L.; Botton, G. A.; Savrasov, S. Y.; Humphreys, C. J.; Sutton, A. P., Electron-energy-loss spectra and the structural stability of nickel oxide: An LSDA+U study. *Physical Review B* 1998, *57* (3), 1505-1509.

95. Hu, Z.; Metiu, H., Choice of U for DFT+U Calculations for Titanium Oxides. *The Journal of Physical Chemistry C* 2011, *115* (13), 5841-5845.

96. Morgan, B. J.; Watson, G. W., A Density Functional Theory + U Study of Oxygen Vacancy Formation at the (110), (100), (101), and (001) Surfaces of Rutile TiO_2. *The Journal of Physical Chemistry C* 2009, *113* (17), 7322-7328.

97. Chueh, Y. L.; Hsieh, C. H.; Chang, M. T.; Chou, L. J.; Lao, C. S.; Song, J. H.; Gan, J. Y.; Wang, Z. L., RuO_2 Nanowires and RuO_2/TiO_2 Core/Shell Nanowires: From Synthesis to Mechanical, Optical, Electrical, and Photoconductive Properties. *Advanced Materials* 2006, *19* (1), 143-149.

98. Bengtsson, L., Dipole correction for surface supercell calculations. *Physical Review B* 1999, *59* (19), 12301-12304.

99. Monkhorst, H. J.; Pack, J. D., Special points for Brillouin-zone integrations. *Physical Review B* 1976, *13* (12), 5188-5192.

100. Hadjiivanov, K., Identification and Characterization of Surface Hydroxyl Groups by Infrared Spectroscopy. *Advances in Catalysis* 2014, 57, 99-318.

101. Mino, L.; Spoto, G.; Bordiga, S.; Zecchina, A., Rutile Surface Properties Beyond the Single Crystal Approach: New Insights from the Experimental Investigation of Different Polycrystalline Samples and Periodic DFT Calculations. *The Journal of Physical Chemistry C* 2013, *117* (21), 11186-11196.

102. Busca, G.; Saussey, H.; Saur, O.; Lavalley, J. C.; Lorenzelli, V., FT-IR Characterization of the Surface Acidity of Different Titanium Dioxide Anatase Preparations. *Appl. Catal.A* 1985, *14*, 245-260.

103. Šurca Vuk, A.; Ješe, R.; Gaberšček, M.; Orel, B.; Dražič, G., Structural and spectroelectrochemical (UV–vis and IR) studies of nanocrystalline sol–gel derived TiO_2 films. *Solar Energy Materials and Solar Cells* 2006, *90* (4), 452-468.

104. K. E. Lewis; Parfit, G. D., Infra-red Study of hte Surface of Rutile. *Transactions of the Faraday Society* 1966, *62*, 204-214.

105. McCool, B.; Tripp, C. P., Inaccessible Hydroxyl Groups on Silica Are Accessible in Supercritical CO_2. *J. Phy. Chem. B* 2005, *109*, 8914-8919.

106. Lin, H.; Long, J.; Gu, Q.; Zhang, W.; Ruan, R.; Li, Z.; Wang, X., In situ IR study of surface hydroxyl species of dehydrated TiO_2: towards understanding pivotal surface processes of TiO_2 photocatalytic oxidation of toluene. *Phys Chem Chem Phys* 2012, *14* (26), 9468-74.

107. Han, B.; Hang Hu, Y., Investigation on H-containing shallow trap of hydrogenated TiO_2 with in situ Fourier transform infrared diffuse reflection spectroscopy. *Nanotechnology* 2017, *28* (30), 304001.

108. Sezen, H.; Buchholz, M.; Nefedov, A.; Natzeck, C.; Heissler, S.; Di Valentin, C.; Wo¨ll, C., Probing Electrons in TiO_2 Polaronic Trap States by IR-Absorption: Evidence for the Existence of Hydrogenic States. *Sci. Rep.* 2014, *4*, 3808.

109. Payne, D. T.; Zhang, Y.; Pang, C. L.; Fielding, H. H.; Thornton, G., Creating Excess Electrons at the Anatase TiO_2(101) Surface. *Topics in Catalysis* 2016.

110. Rekoske, J. E.; Barteau, M. A., Isothermal Reduction Kinetics of Titanium Dioxide-Based Materials. *J. Phys. Chem. B* 1997, *101*, 1113-1124.

111. Guo, J.; Watanabe, S.; Janik, M. J.; Ma, X.; Song, C., Density functional theory study on adsorption of thiophene on TiO_2 anatase (001) surfaces. *Catalysis Today* 2010, *149* (1), 218-223.

112. Thomas, A. G.; Flavell, W. R.; Mallick, A. K.; Kumarasinghe, A. R.; Tsoutsou, D.; Khan, N.; Chatwin, C.; Rayner, S.; Smith, G. C.; Stockbauer, R. L.; Warren, S.; Johal, T. K.; Patel, S.; Holland, D.; Taleb, A.; Wiame, F., Comparison of the electronic structure of anatase and rutile TiO_2 single-crystal surfaces using resonant photoemission and x-ray absorption spectroscopy. *Physical Review B* 2007, *75* (3), 035105.

113. Liang, Y.; Gan, S.; Chambers, S. A.; Altman, E. I., Surface structure of anatase TiO_2: Reconstruction, atomic steps, and domains. *Physical Review B* 2001, *63* (23), 235402.

114. Yuan, W.; Wu, H.; Li, H.; Dai, Z.; Zhang, Z.; Sun, C.; Wang, Y., In Situ STEM Determination of the Atomic Structure and Reconstruction Mechanism of the TiO_2 (001) (1 × 4) Surface. *Chemistry of Materials* 2017, *29* (7), 3189-3194.

115. Selçuk, S.; Selloni, A., Surface Structure and Reactivity of Anatase TiO_2 Crystals with Dominant {001} Facets. *The Journal of Physical Chemistry C* 2013, *117* (12), 6358-6362.

116. Cheng, H.; Selloni, A., Surface and subsurface oxygen vacancies in anatase TiO_2 and differences with rutile. *Physical Review B* 2009, *79* (9), 092101.

117. Li, H.; Guo, Y.; Robertson, J., Calculation of TiO2 Surface and Subsurface Oxygen Vacancy by the Screened Exchange Functional. *The Journal of Physical Chemistry C* 2015, *119* (32), 18160-18166.

118. Aschauer, U.; Selloni, A., Hydrogen interaction with the anatase TiO_2(101) surface. *Phys Chem Chem Phys* 2012, *14* (48), 16595-602.

119. Vittadini, A.; Casarin, M.; Selloni, A., Chemistry of and on TiO_2-anatase surfaces by DFT calculations: a partial review. *Theoretical Chemistry Accounts* 2007, *117* (5-6), 663-671.

120. Henderson, M. A.; Lyubinetsky, I., Molecular-level insights into photocatalysis from scanning probe microscopy studies on TiO_2 (110). *Chem. Rev.* 2013, *113* (6), 4428-55.

121. Ramamoorthy, M.; Vanderbilt, D.; King-Smith, R. D., First-principles calculations of the energetics of stoichiometricTiO_2 surfaces. *Physical Review B* 1994, *49* (23), 16721-16727.

122. Yuan, W.; Meng, J.; Zhu, B.; Gao, Y.; Zhang, Z.; Sun, C.; Wang, Y., Unveiling the Atomic Structures of the Minority Surfaces of TiO_2 Nanocrystals. *Chemistry of Materials* 2018, *30* (1), 288-295.

123. Bourikas, K.; Kordulis, C.; Lycourghiotis, A., Titanium dioxide (anatase and rutile): surface chemistry, liquid-solid interface chemistry, and scientific synthesis of supported catalysts. *Chem Rev* 2014, *114* (19), 9754-823.

124. Bouzoubaa, A.; Markovits, A.; Calatayud, M.; Minot, C., Comparison of the reduction of metal oxide surfaces: TiO_2-anatase, TiO_2-rutile and SnO_2-rutile. *Surface Science* 2005, *583* (1), 107-117.

125. Sinha, P.; Boesch, S. E.; Gu, C.; Wheeler, R. A.; Wilson, A. K., Harmonic Vibrational Frequencies: Scaling Factors for HF, B3LYP, and MP2 Methods in Combination with Correlation Consistent Basis Sets. *The Journal of Physical Chemistry A* 2004, *108* (42), 9213-9217.

126. Andersson, M. P.; Uvdal, P., New Scale Factors for Harmonic Vibrational Frequencies Using the B3LYP Density Functional Theory Method with the Triple-ζ Basis Set 6-311+G(d,p). *J. Phys. Chem. A* 2005, *109*, 2937-2941.

127. Irikura, K. K.; III, R. D. J.; Kacker, R. N.; R.Kessel, Uncertainties in Scaling Factors for ab initio Vibrational Zero-Point Energies. *J. Chem. Phys.* 2009, *130*, 114102-114111.

128. Kashinski, D. O.; Chase, G. M.; Nelson, R. G.; Di Nallo, O. E.; Scales, A. N.; VanderLey, D. L.; Byrd, E. F. C., Harmonic Vibrational Frequencies: Approximate Global Scaling Factors for TPSS, M06, and M11 Functional Families Using Several Common Basis Sets. *The Journal of Physical Chemistry A* 2017, *121* (11), 2265-2273.

129. Sholl, D.; Steckel, J. A., *Density Functional Theory: A Practical Introduction*. John Wiley & Sons, Inc.: Hoboken, New Jersey, 2009; p 252.

130. Menetrey, M.; Markovits, A.; Minot, C., Reactivity of a reduced metal oxide surface: hydrogen, water and carbon monoxide adsorption on oxygen defective rutile TiO_2 (110). *Surface Science* 2003, *524* (1-3), 49-62.

131. Osuga, R.; Yokoi, T.; Doitomi, K.; Hirao, H.; Kondo, J. N., Infrared Investigation of Dynamic Behavior of Brønsted Acid Sites on Zeolites at High Temperatures. *The Journal of Physical Chemistry C* 2017, *121* (45), 25411-25420.

132. Miki Niwa; Katsuki Suzuki; Kazuyo Isamoto; Katada, N., Identification and Measurements of Strong Brønsted Acid Site in Ultrastable Y (USY) Zeolite. *J. Phy. Chem. B* 2006, *110*, 264-269.

133. Miki Niwa; Katsuki Suzuki; Naonobu Katada; Tomonori Kanougi; Atoguchi, T., Ammonia IRMS-TPD Study on the Distribution of Acid Sites in Mordenite. *J. Phys. Chem. B* 2005, *109*, 18749-18757.

134. Mondal, T.; Tripathi, A.; Zhang, J.; Sathe, V.; Shripathi, T.; Shinohara, H.; Tiwari, A., Temperature-Dependent Raman Study of Gd@C82. *The Journal of Physical Chemistry C* 2015, *119* (22), 12698-12702.

135. Yiqing, C.; Peng, B.; Wang, B., Raman Spectra and Temperature-Dependent Raman Scattering of Silicon Nanowires. *J. Phy. Chem. C* 2007, *111*, 5855-5858.

136. Mendoca, C.; Rabbani, S. R., Anharmonic Lattice Vibrations and the Temperature Shift of Raman Spectral *Z. Naturforsch* 1996, *51a*, 716-720.

137. Nelson, R.; Baek, B.; Ruiz, P.; Goundie, B.; Brooks, A.; Wheeler, M. C.; Frederick, B. G.; Grabow, L. C.; Austin, R. N., Experimental and theoretical insights into the hydrogen-efficient direct hydrodeoxgenation mechanism of phenol over Ru/TiO_2. *ACS Catal.* 2015, *11*, 6509-6523.

138. Kavan, L.; Basca, R.; Tunckol, M.; Serp, P.; Zakeeruddin, S. M.; Le Formal, F.; Zukalova, M.; Graetzel, M., Multi-walled carbon nanotubed functionalized by carboxylic groups: Activation of TiO_2 (anatase) and phosphate olivines ($LiMnPO_4$; $LiFePO_4$) for electrochemical Li-storage. *Journal of Power Sources* 2010, *195*, 5360-5369.

139. Brunauer, S.; Emmett, P. H.; Teller, E., Adsorption of Gases in Multimolecular Layers. *Journal of the American Chemical Society* 1938, *60*, 309-319.

140. Klissurski, K. H. a. D. G., Surface Chemistry of Titania (Anatase) and Titania-supported Catalysts. *Chem. Soc. Rev.* 1996, *107*, 534-545.

141. Colon, G.; Hidalgo, M. C.; Munuera, G.; Ferino, I.; Cutrufello, M. G.; Navio, J. A., Structural and surface approach to the enhanced photocatalytic activity of sulfated TiO_2 photocatalyst. *Appl Catal B* 2006, *63*, 45-49.

142. Seah, M. P.; Spencer, S. J., Ultrathin SiO_2 on Si. I. Quantifying and removing carbonaceous contamination. *Journal of Vacuum Science & Technology A* 2003, *21* (2), 345-352.

143. Reilman, R. F.; Msezane, A.; Manson, S. T., Relative intensities in photoelectron spectroscopy of atoms and molecules. *Journal of Electron Spectroscopy and Related Phenomena* 1976, *8*, 389-394.

144. Scofield, J. H., Hartree-Slater subshell photoionization cross-sections at 1254 and 1487 eV. *Journal of Electron Spectroscopy and Related Phenomena* 1976, *8*, 129-137.

145. Seah, M. P., A system for the intensity calibration of electron spectrometers. *Journal of Electron Spectroscopy and Related Phenomena* 1995, *71* (3), 191-204.

146. Olson, C. L.; Nelson, J.; Islam, M. S., Defect Chemistry, Surface Structures, and Lithium Insertion in Anatase TiO_2. *The Journal of Physical Chemistry B* 2006, *110* (20), 9995-10001.

147. Mino, L.; Spoto, G.; Ferrari, A. M., CO_2 capture by TiO_2 Anatase Surfaces: A combined DFT and FTIR study. *J. Phys. Chem C* 2014, *118*, 25016-25026.

148. Mino, L.; Spoto, G.; Bordiga, S.; Zecchina, A., Particles, Morphology and Surface Properties As Investigated by HRTEM, FTIR, and Periodic DFT Calculations: From Pyrogenic TiO_2 (P25) to Nanoanatase. *J. Phys. Chem. C.* 2012, *116*, 17008-17018.

149. Saur, P.; Bensitel, M.; Saad, A. B. M.; Lavalley, J. C.; Tripp, C. P.; Morrow, B. A., The Structure and Stability of Sulfated Alumnia and Titania. *Journal of Catalysis* 1986, *99*, 104-110.

150. Lange, F.; Hadjiivanov, K.; Schmelz, H.; Knozinger, H., Low Temperature Infrared Study of Carbon Monoxide Adsorption on Sulfated Titania. *Catal Lett* 1992, *16* (1), 97-107.

151. Sayed, F. N.; Jayakumar, O. D.; Sasikala, R.; Kadam, R. M.; Bharadwaj, S. R.; Kienle, L.; Schürmann, U.; Kaps, S.; Adelung, R.; Mittal, J. P.; Tyagi, A. K., Photochemical Hydrogen Generation Using Nitrogen-Doped TiO_2–Pd Nanoparticles: Facile Synthesis and Effect of Ti3+ Incorporation. *The Journal of Physical Chemistry C* 2012, *116* (23), 12462-12467.

152. Hadjiivanov, K. I.; Klissurki, D. G., surface chemistry of titania (anatase) and titania-supported catalysts. *Chem Soc. Rev.* 1996, 61-69.

153. Newman, C.; Zhou, X.; Goundie, B.; Ghampson, I. T.; Pollock, R. A.; Ross, Z.; Wheeler, M. C.; Meulenberg, R.; Austin, R. N.; Frederick, B. G., Effects of support identity and metal dispersion in supported ruthenium hydrodeoxygenation catalysts. *Appl Catal A Gen* 2014, *477*, 64-74.

154. Omotoso, T. O.; Baek, B.; Grabow, L. C.; Crossley, S. P., Experimental and First-Principles Evidence for Interfacial Activity of Ru/TiO_2 for the Direct Conversion of m-Cresol to Toluene. *ChemCatChem* 2017, *9* (14), 2642-2651.

155. Omotoso, T.; Boonyasuwat, S.; Crossley, S. P., Understanding the role of TiO_2 crystal structure on the enhanced activity and stability of Ru/TiO_2 catalysts for the conversion of lignin-derived oxygenates. *Green Chem.* 2014, *16*, 645-655.

156. Xiang, G.; Shi, X.; Wu, Y.; Zhuang, J.; Wang, X., Size effects in Atomic-Level Epitaxial Redistribution Process of RuO_2 over TiO_2. *Scientific Reports* 2012, *2*, 801.

157. Liu, Z.; Sriram, V.; Lee, J.-Y., Heterogeneous oxidation of elemental mercury vapor over RuO_2/rutile TiO_2 catalyst for mercury emission control. *Applied Catalysis B Environmental* 2017, *207*, 143-152.

158. Aranda-Perez, N.; Ruiz, M. P.; Echave, J.; Faria, J., Enhanced Activity and Stability of $Ru\text{-}TiO_2$ for Liquid Phase Ketonization. *Appl Catal A* 2017, 531, 106

159. Kim, A.; Sanchez, C.; Patriarche, G.; Ersen, O.; Moldovan, S.; Wisnet, A.; Sassoye, C.; Debecker, D. P., Selective CO_2 methanation on Ru/TiO_2 catalysts: unravelling the decisive role of the TiO_2 support crystal structure. *Catal. Sci. Technol.* 2016, *6*, 8117-8128.

160. Yang, C.; Zhao, Z.-Y., Investigation of energy band alignments and interfacial properties of rutile NMO_2/TiO_2 (NM = Ru, Rh, Os, and Ir) by first-principles calculations. *Physical Chemistry Chemical Physics* 2017, *19* (43), 29583-29593.

161. Hurum, D. C.; Agrios, A. G.; Gray, K. A.; Rajh, T.; Thurnauer, M. C., Explaining the Enhanced Photocatalytic Activity of Degussa P25 Mixed-Phase TiO_2 Using EPR. *The Journal of Physical Chemistry B* 2003, *107* (19), 4545-4549.

162. Datye, A.; Riegel, G.; Bolton, J. R.; Huang, M.; Prarie, M. R., Microstructural characterization of a fumed titanium dioxide photocatalyst. *Journal of solid state chemistry* 1995, *115*, 236-239.

163. Bickley, R. I.; Gonzalez-Carreno, T.; Lees, J. S.; Palmisano, L.; Tilley, R. J. D., A structural investigation of titanium dioxide photocatalysts. *Journal of Solid State Chemistry* 1991, *92* (1), 178-190.

164. Datye, A. K.; Riegel, G.; Bolton, J. R.; Huang, M.; Prairie, M. R., Microstructural Characterization of a Fumed Titanium Dioxide Photocatalyst. *Journal of Solid State Chemistry* 1995, *115* (1), 236-239.

165. Mahdavi-Shakib, A.; Arce, J. M.; Austin, R. N.; Schwartz, T. J.; Grabow, L. C.; Frederick, B. G., Use of Surface Hydroxyl Frequencies to Identify the Exposed Facets of Pyrogenic TiO_2 Nanoparticles. *J Phys Chem C* 2018, *(in prep)*.

166. Shiraishi, Y.; Hirakawa, H.; Togawa, Y.; Sugano, Y.; Ichikawa, S.; Hirai, T., Rutile Crystallites isolated from Deguassa (Evonik) P25 TiO_2: Highly Efficient Photocatalyst for Chemoslective Hydrogenation of Nitroaromatics. *ACS Catal.* 2013, *33*, 2318-2326.

167. Gao, D.; Schweitzer, C.; Hwang, H. T.; Varma, A., Conversion of Guaiacol on Noble Metal Catalysts: Reaction Performance and Deactivaton Studies. *Ind. Eng. Chem. Res.* 2014, *57*, 18658-18667.

168. Saur, O.; Bensitel, M.; Saad, A. B. M.; Lavalley, J. C.; Tripp, C. P.; Morrow, B. A., The structure and stability of sulfated alumina and titania. *Journal of Catalysis* 1986, *99* (1), 104-110.

169. Li, F.; Huang, W.-H.; Gon, X.-Q., Unique adsorption behaviors of NO and O_2 at hydrogenated anatase TiO_2 (101). *Chinese Chemical Letters* 2018, 29, 765-768.

170. Zongyan, Z.; Zhaosheng, L.; Zhigang, Z., Surface properties and electronic structure of low-index stoichiometric anatase TiO_2 surfaces. *Journal of Physics: Condensed Matter* 2010, *22* (17), 175008.

171. Gordon, T. R.; Cargnello, M.; Paik, T.; Mangolini, F.; Weber, R. T.; Fornasiero, P.; Murray, C. B., Nonaqueous Synthesis of TiO_2 Nanocrystals Using TiF_4 to Engineer Morphology, Oxygen Vacancy Concentration, and Photocatalytic Activity. *J Am Chem Soc* 2012, *134*, 6751-6761.

172. Peng, Y. K.; Hu, Y.; Chou, H. L.; Fu, Y.; Teixeira, I. F.; Zhang, L.; He, H.; Tsang, S. C. E., Mapping surface-modified titania nanoparticles with implications for activity and facet control. *Nat Commun* 2017, *8* (1), 675.

173. Miroshnichenko, O.; Posysaev, S.; Alatalo, M., A DFT study of the effect of SO_4 groups on the properties of TiO_2 nanoparticles. *Phys. Chem. Chem. Phys.* 2016, *18* (48), 33068-33076.

174. Lin, X. H.; Li, S. F. Y., Impact of the spatial distribution of sulfate species on the activities of SO_4^{2-}/TiO_2 photocatalysts for the degradation of organic pollutants in reverse osmosis concentrate. *Applied Catalysis B: Environmental* 2015, *170-171*, 263-272.

175. Lin, X. H.; Yin, X. J.; Liu, J. Y.; Yau Li, S. F., Elucidation of structures of surface sulfate species on sulfated titania and mechanism of improved activity. *Applied Catalysis B: Environmental* 2017, *203*, 731-739.

176. Xiong, Y.; He, D.; Jaber, R.; Cameron, P. J.; Edler, K. J., Sulfur-Doped Cubic Mesostructured Titania Films for Use as a Solar Photocatalyst. *The Journal of Physical Chemistry C* 2017, *121* (18), 9929-9937.

177. Devi, L. G.; Kavitha, R., Enhanced photocatalytic activity of sulfur doped TiO_2 for the decomposition of phenol: A new insight into the bulk and surface modification. *Materials Chemistry and Physics* 2014, *143* (3), 1300-1308.

178. Xie, C.; Yang, Q.; Xu, Z.; Du, Y., Effect of calcination temperature on the physicochemical properties of highly active sulfated titania photocatalysts. *Journal of Molecular Catalysis A: Chemical* 2014, *381*, 107-113.

179. Naik, B.; Parida, K. M.; Gopinath, C. S., Facile Synthesis of N- and S-Incorporated Nanocrystalline TiO_2 and Direct Solar-Light-Driven Photocatalytic Activity. *The Journal of Physical Chemistry C* 2010, *114*, 19473-19482.

180. Wang, X.; Yu, J. C.; Liu, P.; Wang, X.; Su, W.; Fu, X., Probing of photocatalytic surface sites on SO_4^{2-}/TiO_2 solid acids by in situ FT-IR spectroscopy and pyridine adsorption. *Journal of Photochemistry and Photobiology A: Chemistry* 2006, *179* (3), 339-347.

181. Colón, G.; Hidalgo, M. C.; Munuera, G.; Ferino, I.; Cutrufello, M. G.; Navío, J. A., Structural and surface approach to the enhanced photocatalytic activity of sulfated TiO_2 photocatalyst. *Applied Catalysis B: Environmental* 2006, *63* (1-2), 45-59.

182. Barraud, E.; Bosc, F.; Edwards, D.; Keller, N.; Keller, V., Gas phase photocatalytic removal of toluene effluents on sulfated titania. *Journal of Catalysis* 2005, *235* (2), 318-326.

183. Xie, C.; Yang, Q.; Xu, Z.; Liu, X.; Du, Y., New Route to Synthesize Highly Active Nanocrystalline Sulfated Titania-Silica: Synergetic Effects between Sulfate Species and Silica in Enhancing the Photocatalysis Efficiency. *The Journal of Physical Chemistry B* 2006, *110*, 8587-8592.

184. Gómez, R.; López, T.; Ortiz-Islas, E.; Navarrete, J.; Sánchez, E.; Tzompanztzi, F.; Bokhimi, X., Effect of sulfation on the photoactivity of TiO_2 sol–gel derived catalysts. *Journal of Molecular Catalysis A: Chemical* 2003, *193* (1-2), 217-226.

185. Panayotov, D. A.; Yates, J. T., n-Type doping of TiO_2 with atomic hydrogen-observation of the production of conduction band electrons by infrared spectroscopy. *Chemical Physics Letters* 2007, *436* (1-3), 204-208.

186. Vequizo, J. J. M.; Matsunaga, H.; Ishiku, T.; Kamimura, S.; Ohno, T.; Yamakata, A., Trapping-Induced Enhancement of Photocatalytic Activity on Brookite TiO_2 Powders: Comparison with Anatase and Rutile TiO_2 Powders. *ACS Catalysis* 2017, *7* (4), 2644-2651.

187. Yamakata, A.; Vequizo, J. J. M.; Matsunaga, H., Distinctive Behavior of Photogenerated Electrons and Holes in Anatase and Rutile TiO_2 Powders. *The Journal of Physical Chemistry C* 2015, *119* (43), 24538-24545.

188. Litke, A.; Hensen, E. J. M.; Hofmann, J. P., Role of Dissociatively Adsorbed Water on the Formation of Shallow Trapped Electrons in TiO_2 Photocatalysts. *The Journal of Physical Chemistry C* 2017, *121* (18), 10153-10162.

189. Litke, A.; Su, Y.; Tranca, I.; Weber, T.; Hensen, E. J. M.; Hofmann, J. P., Role of Adsorbed Water on Charge Carrier Dynamics in Photoexcited TiO_2. *The Journal of Physical Chemistry C* 2017, *121* (13), 7514-7524.

190. Panayotov, D. A.; Burrows, S. P.; Morris, J. R., Photooxidation Mechanism of Methanol on Rutile TiO_2 Nanoparticles. *The Journal of Physical Chemistry C* 2012, *116* (11), 6623-6635.

191. Kukimoto, H.; Hioki, R.; Koda, T.; Shionoya, S., Infrared Absorption Due to Shallow Electron Traps and the Effective Mass in ZnS. *Physics Letters* 1965, *19*, 551-552.

192. Kukimoto, H.; Shionoya, S.; Koda, T.; Hioki, R., Infrared Absorption Due to Donor States in ZnS Crystals. *J. Phys. Chem. Solids* 1968, *29*, 935-944.

193. Panayotov, D. A.; John T. Yates, J., Spectroscopic Detection of Hydrogen Atom Spillover from Au Nanoparticles Supported on TiO_2: Use of Conduction Band Electrons. *The Journal of Physical Chemistry C* 2007, *111*, 2959-2964.

194. Kröger, F.; Vink, H., Relationships Between the Concentrations of Imperfections in Crystalline Solids. In *Solid State Physics*, Seitz, F.; Turnbull, D., Eds. 1956; Vol. 3, pp 307-435.

195. Savory, D. M.; McQuillan, A. J., Influence of Formate Adsorption and Protons on Shallow Trap Infrared Absorption (STIRA) of Anatase TiO_2 During Photocatalysis. *The Journal of Physical Chemistry C* 2013, *117* (45), 23645-23656.

196. Savory, D. M.; McQuillan, A. J., IR Spectroscopic Behavior of Polaronic Trapped Electrons in TiO_2 under Aqueous Photocatalytic Conditions. *The Journal of Physical Chemistry C* 2014, *118* (25), 13680-13692.

197. Savory, D. M.; Warren, D. S.; McQuillan, A. J., Shallow Electron Trap, Interfacial Water, and Outer-Sphere Adsorbed Oxalate IR Absorption Correlate during UV Irradiation of Photocatalytic TiO_2 Films in Aqueous Solution. *The Journal of Physical Chemistry C* 2011, *115*, 902-907.

198. Berger, T.; Anta, J. A.; Morales-Flórez, V., Electrons in the Band Gap: Spectroscopic Characterization of Anatase TiO_2 Nanocrystal Electrodes under Fermi Level Control. *The Journal of Physical Chemistry C* 2012, *116* (21), 11444-11455.

199. Berger, T.; Anta, J. A., IR-spectrophotoelectrochemical characterization of mesoporous semiconductor films. *Anal. Chem.* 2012, *84* (7), 3053-7.

200. Lee, H.-Y.; Clark, S. J.; Robertson, J., Calculation of point defects in rutile TiO_2 by the screened-exchange hybrid functional. *Physical Review B* 2012, *86* (7).

201. Stausholm-Moller, J.; Kristoffersen, H. H.; Hinnemann, B.; Madsen, G. K.; Hammer, B., DFT+U study of defects in bulk rutile TiO_2. *J. Chem. Phys.* 2010, *133* (14), 144708.

202. Mao, X.; Lang, X.; Wang, Z.; Hao, Q.; Wen, B.; Ren, Z.; Dai, D.; Zhou, C.; Liu, L.-M.; Yang, X., Band-Gap States of TiO_2 (110): Major Contribution from Surface Defects. *The Journal of Physical Chemistry Letters* 2013, *4* (22), 3839-3844.

203. Morterra, C., An Infrared Spectroscopic Study of Anatase Properties Part 6.-Surface Hydration and Strong Lewis Acidity of Pure and Sulphate-doped Preparations. *J. Chem. Soc., Faraday Trans. 1* 1988, *84*, 1617-1637.

BIOGRAPHY OF THE AUTHOR

Akbar Mahdavi-Shakib was born in Tehran, Iran in October 6, 1984. In 2003, he got accepted into the Chemistry Program of Teacher Training University of Tehran (also known as Kharazmi University) and graduated in 2007. Akbar got accepted into Analytical Chemistry program of Sharif University of Technology in 2008 and joined Prof. Saeed Shahrokhian's lab to develop electrochemical sensors by modifying electrode surfaces using self-assembled monolayers. After graduation with a M.Sc. from the Sharif University of Technology, Akbar got accepted into the Chemistry graduate program of the University of Maine in 2012 and joined Prof. Brian Frederick's lab to perform mechanistic studies of reducible metal oxides as hydrodeoxygenation catalysts. Akbar did research on spectroscopic characterization of heterogeneous catalysts and photocatalysts, kinetic modeling of sugar conversion reactions to platform chemicals such as hydroxymethylfurfural and lactic acid, and hydrothermal synthesis of hexagonal WO_3 nanowires. He is a candidate for the Doctor of Philosophy in Chemistry from the University of Maine in August 2018.